ANKARA YILDIRIM BEYAZIT UNIVERSITY

GRADUATE SCHOOL OF NATURAL AND APPLIED SCIENCE



GEL CASTING OF MULLITE FOR RADOME APPLICATIONS

M. Sc. Thesis by

Nazım ECEBAŞ

Department of Materials Engineering

July, 2018

ANKARA

GEL CASTING OF MULLITE FOR RADOME APPLICATIONS

A Thesis Submitted to

the Graduate School of Natural and Applied Sciences of

Ankara Yıldırım Beyazıt University

in Partial Fulfillment of the Requirements for the Degree of Master of Science in Materials Engineering

by

Nazım ECEBAŞ

July, 2018

ANKARA

M.Sc. THESIS EXAMINATION RESULT FORM

We have read the thesis entitled **"GEL CASTING OF MULLITE FOR RADOME APPLICATIONS"** completed by **Nazım ECEBAŞ** under supervision of **Prof. Dr. Cihangir DURAN** and we certify that in our opinion it is fully adequate, in scope and in quality, as a thesis for the degree of Master of Science.

Prof. Dr. Cihangir DURAN

Supervisor

Prof. Dr. Hasan OKUYUCU

Jury Member

Prof. Dr. Hasan GÖÇMEZ

Jury Member

Prof. Dr. Ergün ERASLAN

Director

Graduate School of Natural and Applied Sciences

ETHICAL DECLARATION

I hereby declare that, in this thesis which has been prepared in accordance with the Thesis Writing Manual of Graduate School of Natural and Applied Sciences,

- All data, information and documents are obtained in the framework of academic and ethical rules,
- All information, documents and assessments are presented in accordance with scientific ethics and morals,
- All the materials that have been utilized are fully cited and referenced,
- No change has been made on the utilized materials,
- All the works presented are original,

and in any contrary case of above statements, I accept to renounce all my legal rights.

2018, 30 July **Nazım ECEBAŞ**

ACKNOWLEDGMENTS

Firstly, I would like to express my gratitude to my supervisor Prof. Dr. Cihangir Duran for his encouragement from the beginning of the work and his support during study period. I am also thankful for his advice, comment, patience and kind help.

I would like to thank Hande Yeşilova, Meryem Dursun, Necati Uçak, Abdullah Atılgan to help me during my studies. I would like to thank Kadir Kaan KARAVELİ from Turkuaz seramik for dilatometer measurements. I would like to thank to Prof. Dr. Yahya Kemal TÜR from Gebze Technical University for Young's modulus and flexural strength measurements. Finally, I am thankful to Meteksan Savunma A.Ş. for dielectric measurements.

Last, but not least, I would like to thank my family for their encouragements and supports during my studies.

2018, 30 July **Nazım ECEBAŞ**

GEL CASTING OF MULLITE FOR RADOME APPLICATIONS

ABSTRACT

Gel casting is a colloidal processing route to produce large and 3D complex products. It was aimed to investigate gel casting of mullite ceramics because this method has not been studied to produce dense mullite ceramics in literature. Mullite was chosen due to its excellent creep and thermal shock resistance at high temperatures, and low dielectric properties suitable for electronic and radome applications. Gel casting parameters such as monomer types, their ratios, effect of initiator and catalyzer were studied. Densification behavior, dielectric properties, mechanical properties and thermal properties were characterized in detail for radome applications. Initial mullite powder had 5-10% glass phase and 1 % corundum. Ball milling for 48 h decreased mean particle size from 3-5 μm to 0.28 μm. 3.4 wt% nano TiO_2 (e.g., 21 nm) was added to form a liquid phase to aid densification. Gelation of the slurries was completed in 3 to 5 minutes at 25°C for the samples with catalyzer and in 35 to 65 minutes at 70°C for the samples without catalyzer. All samples reached to the relative densities of 97 to 98.2 % after sintering at 1540°C for 2 h. Backscattered SEM images revealed anisotropically grown mullite grains, glassy phase located as islands between the grains, hexagonally-shaped Al_2O_3 grains, white-color grains rich in ZrO_2 and TiO_2, and pores with sharp corners. All samples had hardness values between 1077 HV to 1089 HV, and fracture toughness values between 2.4 to 2.5 MPa. $\sqrt{m}$. The Weibull modulus was calculated as 12.33. Thermal conductivity increased and ranged from 1.5 W/m.K at 50°C to 3.75 W/m.K at 550°C due to the presence of a glassy phase. Thermal expansion coefficient was 5.26 ppm/°C between 30°C and 800°C. The dielectric constant was nearly 7.5 up to 10 GHz and loss tangent was 0.0031 at 5 MHz. Mullite is a suitable candidate for radome applications because it has a higher thermal shock resistance parameter (142°C) than Al_2O_3 and has advantages in terms of sintering in air as opposed to Si_3N_4 and BN ceramics. A large block (240x250x35 mm^3) was successfully casted, and then easily machined to the desired shapes.

Keywords: Mullite, Gel casting, Liquid phase sintering, Mechanical properties, Thermal Properties, Dielectric Properties, Radome

RADOM UYGULAMALARI İÇİN JEL DÖKÜM İLE MÜLLİT ÜRETİMİ

ÖZ

Jel döküm karmaşık ve 3 boyutlu ürünler yapmak için kullanılan koloidal bir yöntemdir. Yoğun müllit seramik üretimi literatürde daha önce çalışılmadığı için jel döküm ile bu seramiklerin üretimi amaçlanmıştır. Yüksek sıcaklıkta sürünme ve ısısal şok direncinin mükemmel ve düşük dielektrik sabitinden dolayı radom ve elektronik uygulamalar için müllit seçilmiştir. Monomer türü, oranları, reaksiyon başlatıcı ve katalizör etkileri jel döküm parametreleri olarak çalışılmıştır. Yoğunlaşma davranışı, dielektrik özelikler, mekanik özellikler ve termal özellikler detaylı karakterize edilmiş ve radome uygulamaları için uygunluğu araştırılmıştır. Başlangıç müllit tozu yüzde 5-10 arasında cam fazı ve yüzde 1 korundum içermektedir. 48 saat bilyeli öğütücü ile ortalama parçacık boyutu 3-5 μm'dan 0.28 μm'a indirilmiştir. Sıvı faz oluşturarak yoğunlaşmaya katkıda bulunması için ağırlıkça yüzde 3.4 nano TiO_2 (21 nm) eklenmiştir. Katalizör eklenen çamurların katılaşması 25°C'de 3 ile 5 dk. ve katalizör eklenmeyen çamurların katılaşması 70°C'de 35 ile 65 dk. arasında tamamlanmıştır. Numunelerin 1540°C'de 2 saat sinterlenmesinden sonra bağıl yoğunluk yüzde 97 ile yüzde 98.2 arasında ölçülmüştür. Elektron mikroskop çalışması anizotropik büyüyen müllit taneleri, bu taneler arasında ada şeklinde cam fazı, altıgen şeklinde alüminyum oksit tanelerini, zirkonyum dioksit ve titanyum dioksit miktarının fazla olduğu açık renkli taneler ve keskin köşeli boşlukları göstermiştir. Bütün numunelerin sertlik değerleri 1077 ve 1089 HV arasında, kırılma toklukları ise 2.4 ile 2.5 MPa.$\sqrt{m}$ arasında bulunmuştur. Weibull modülü 12.33 olarak hesaplanmıştır. Cam fazdan dolayı termal iletkenlik 50°C'de 1.5 W/m.K değerinden 550°C'de 3.75 W/m.K değerine yükselmiştir. Termal genleşme katsayısı 30°C ile 800°C arasında 5.26 ppm/°C bulunmuştur. Dielektrik sabiti yaklaşık 10 GHz e kadar 7.5 ve dielektrik kayıp 5 MHz'de 0.0031 olarak ölçülmüştür. Müllit, termal şok direnç parametresi (142°C) alüminyum oksitten büyük olması, bor nitrit ve silisyum nitrüre göre havada sinterlenmesi avantajlarından dolayı radom uygulamaları için aday bir malzemedir. Büyük bir blok (240x250x35 mm^3) başarıyla dökülmüş ve kolaylıkla istenilen şekle işlenmiştir.

Anahtar kelimeler: Müllit, Jel döküm, Sıvı faz sinterleme, Mekanik Özellikler, Termal Özellikler, Dielektrik Özellikler, Radom.

CONTENTS

M.Sc. THESIS EXAMINATION RESULT FORM ..... **ii**
ETHICAL DECLARATION ..... **iii**
ACKNOWLEDGMENTS ..... **iv**
ABSTRACT ..... **v**
ÖZ ..... **vi**
CONTENTS ..... **vii**
NOMENCLATURE ..... **viii**
ABBREVIATIONS ..... **viii**
LIST OF SYMBOLS ..... **xi**
LIST OF TABLES ..... **xiii**
LIST OF FIGURES ..... **xiv**
CHAPTER 1 INTRODUCTION 1
1.1 Gel casting method 1
1.2 Radome Materials 10
1.2.1 Dielectric properties 12
1.2.2 Mechanical and Thermal properties 17
1.3 Mullite Materials 20
1.4 The review of literature 23
1.5 Objective 23
CHAPTER 2 EXPERIMENTAL MEDHODS 25
CHAPTER 3 RESULTS AND DISCUSSION 33
3.1 Phase Analysis and Densification 33
3.2 Mechanical Properties 49
3.3 Thermal properties 60
3.4 Dielectric properties 68
3.5 Application 69
CHAPTER 4 CONCLUSION 72
FUTURE STUDIES 77
REFERENCES 78
CIRCULUM VITAE 87

NOMENCLATURE

ABBREVIATIONS

μm	Micrometer
Al_2O_3	Alumina
CaO	Calcium Oxide
K_2O	Potassium Oxide
MPa	Mega Pascal
Na_2O	Sodium Oxide
rpm	Round per minute
SiO_2	Silica
vol%	Volume percent
wt%	Weight percent
AM	Acrylamide
MBAM	Methylenebisacrylamide
APS	Ammoniumpersulfate
TEMED	Tetramethylenediamine
HMAM	Hydroxymethylacrylamide
NVP	N-vinylpyrrolidone
MPEGMA	Methoxypoly (ethyleneglycol) monomethacrylate
3-D	3-Dimension
PEG600	Polyethylene glycol 600
RF	Radio frequency
MHz	Megahertz
GHz	Gigahertz
Hz	Hertz
KHz	Kilohertz
GPa	Giga Pascal

ppm	Part per million
$PbZrTiO_3$	Lead zirconate titanate
ZrO_2	Zirconium oxide
B_2O_3	Boron trioxide
TBA	Tert-butyl alcohol
TiO_2	Titanium oxide
Fe_2O_3	Ferric oxide
MgO	Magnesium oxide
K_2O	Potassium oxide
HCl	Hydrogen chloride
CTE	Thermal expansion coefficient
d_{50}	Median particle size
IEP	Isoelectric point
Al_2TiO_5	Aluminum titanate
$ZrTiO_4$	Zirconium titanate
BeO	Beryllium oxide
BN	Boron nitride
$2MgO.2Al_2O_3.5SiO_2$	Cordierite
Si_3N_4	Silicon nitride
$3Al_2O_3$-$2SiO_2$	Mullite

Acronyms:

EDS	Energy Dispersive Spectrometry
HV	Vickers Hardness
LPS	Liquid Phase Sintering
OM	Optical Microscope
SEM	Scanning Electron Microscopy
XRD	X-ray Diffraction
TG-DTA	Thermogravimetric-Differential Thermal Analysis

LIST OF SYMBOLS

R	Thermal shock resistance
°	Degree
μ	Poisson's ratio
2θ	Diffraction angle
C	Capacitance
E	Young's modulus
J	Joule
K	Dielectric constant
m	Meter
N	Newton
η	Viscosity
P	Force
Pa	Pascal
T	Temperature
V	Volume
W	Watt
α	Thermal expansion coefficient
Δ	Difference
ρ	Density
P_e	Electronic polarization
P_i	Ionic polarization,
P_d	Dipolar polarization,
P_s	Space charge polarization
P_t	Total polarization
ε_0	Permittivity of space (8.8542×10^{-12} $F.m^{-1}$)
K	Dielectric constant
X	Electric susceptibility
E	Electric field

P_0	Power out
P_x	Power in
P_A	Insertion loss
σ_f	Flexural strength
HV	Vickers hardness
K_c	Fracture toughness
δ	Non-dimensional constant
m	Mass
σ	Characteristic strength
α	Thermal diffusivity
C_p	Specific heat
P_e	Volume friction of porosity
s	second
h	hour

LIST OF TABLES

Table 1.1. Comparison between Gel casting and other ceramic processes 6

Table 1.2. Mold materials for gel casting..... 8

Table 1.3. Examples of candidate materials for radome applications..... 20

Table 1.4. Properties of mullite ceramics..... 22

Table 2.1. Properties of mullite 25

Table 2.2. The properties of TiO_2..... 26

Table 2.3. The weight of AM, MBAM and water in monomer solutions and the solubility of MBAM in water..... 26

Table 3.1. The bulk density, relative density, and apparent porosity of the samples prepared with/out TEMED at different AM/MBAM ratios (t refers to TEMED) 41

Table 3.2. The results of average fracture toughness and crack extension after quenching (+ denotes increment and – denotes decrement with respect to the 25°C values)..... 66

Table 3.3. Thermal shock resistance (TSR) of the sample with TEMED at AM/MBAM ratio of 20 68

Table 3.4. The mechanical, thermal and dielectric results of the mullite ceramics sintered at 1540°C for 2 h 71

LIST OF FIGURES

Figure 1.1. The mechanism of gel casting 2

Figure 1.2. Cross-linking principle of monomers by TEMED and APS 3

Figure 1.3. The effect of amount of APS/TEMED on curing time 3

Figure 1.4. The effect of temperature on curing time with constant APS/ TEMED concentration 4

Figure 1.5. Combined effect of APS and temperature on gelation time 5

Figure 1.6. The ceramic forming methods 6

Figure 1.7. Examples of ceramics fabricated by gel casting 7

Figure 1.8. The macroscopic topography of green bodies under different condition; (a) drying at room temperature, (b) drying in 65 wt% PEG600 solution 9

Figure 1.9. Sialon radome ceramics; (a) nose cracked green radome dried in air and (b) green radome dried in PEG400 9

Figure 1.10. Picture of a radome 10

Figure 1.11. The wall configurations of radome 12

Figure 1.12. Dielectric behavior of materials depend on frequency 13

Figure 1.13. The effect of the amount of porosity on dielectric constant of Si_3N_4 15

Figure 1.14. The loss tangent and dielectric constant of Al_2O_3 as a function of temperature 16

Figure 1.15. The effect of porosity on Young's modulus of micro-structured Al_2O_3 by natural sintering and spark plasma sintering 18

Figure 1.16. Al_2O_3-SiO_2 phase diagram.....21

Figure 1.17. The crystal structure of mullite.....22

Figure 2.1. The flowchart of gel casting process 28

Figure 2.2. Temperature-time profile for binder burnout process.....29

Figure 3.1. XRD pattern of the as-received mullite powder.....33

Figure 3.2. XRD pattern of the as-received TiO_2 powder.....34

Figure 3.3. Median particle size variations as a function of ball milling time.....35

Figure 3.4. The particle size of mullite as a function of milling time.....35

Figure 3.5. The curing of slurries with TEMED at different AM/MBAM ratios ...37

Figure 3.6. The complete curing time of slurries with/out TEMED at different AM/MBAM ratios 37

Figure 3.7. Differential thermal analysis of powder at AM/MBAM ratio of 20.....39

Figure 3.8. The Relative densities of samples without TEMED at different AM/MBAM ratios 40

Figure 3.9. XRD pattern of the sintered mullite ceramics 42

Figure 3.10. Backscattered SEM image of the sample prepared with TEMED and AM/MBAM ratio of 15.....44

Figure 3.11. Back-scattered SEM images of the samples prepared without TEMED at AM/MBAM ratios of (a) 9, (b) 12, (c) 15, and (d) 20 45

Figure 3.12. Back-scattered SEM images of the samples prepared with TEMED at AM/MBAM ratios of (a) 6, (b) 9, (c) 12, and (d) 15 47

Figure 3.13. The hardness of the samples without TEMED (a) and with TEMED (b) at different AM/MBAM ratios 49

Figure 3.14. The hardness indentation pictures of the samples with TEMED (a) and without TEMED (b) at AM/MBAM ratio of 15 51

Figure 3.15. The fracture toughness of the samples without TEMED (a) and with TEMED (b) at different AM/MBAM ratios 52

Figure 3.16. The fracture toughness result samples with TEMED at AM/MBAM ratio of 15 53

Figure 3.17. Back scattered SEM pictures of fracture surface mullite sample with TEMED at AM/MBAM ratios of 20 54

Figure 3.18. The crack propagation in the samples prepared with TEMED at AM/MBAM ratios of 15 55

Figure 3.19. The flexural strength of samples with TEMED (a) and without TEMED (b) at different AM/MBAM ratios 57

Figure 3.20. Dried samples prepared at AM/MBAM ratio of 20 without (a) and with (b) TEMED 58

Figure 3.21. Statistical analysis of flexural strength using Weibull approach 59

Figure 3.22. Young's modulus at different densification levels 60

Figure 3.23. Thermal properties of the sample with TEMED at AM/MBAM ratio of 20 (a) thermal diffusivity, (b) C_P and (c) thermal conductivity as a function of temperature 62

Figure 3.24. Thermal expansion coefficient as a function of temperature 64

Figure 3.25. Relative expansion as a function of temperature 64

Figure 3.26. Change in fracture toughness and crack extension as a function of temperature 65

Figure 3.27. Extension of crack at 200°C, 400°C and 600°C 67

Figure 3.28. Green ceramics at various sizes 69

Figure 3.29. Green machining of a mullite block 70

CHAPTER 1

INTRODUCTION

1.1 Gel casting method

Ceramics are chemically non-metallic and inorganic compounds with exception of carbon. Ceramic materials are produced by various ceramic fabrication methods such as dry pressing, slip casting, tape casting, etc. One of the important ceramic fabrication methods is gel casting method because it allows the production of large and complex shape ceramics [1].

The mechanism of gel casting is schematically shown in Figure 1.1. Gel cast slurries are prepared by mixing (e.g., speed mixer, stirring, ball milling or similar ones) using powder, monomer solution using acrylamide (AM) and methylenebisacrylamide (MBAM), initiator ammoniumpersulfate (APS) and catalyzer tetramethylenediamine (TEMED). TEMED is also called as initiator. First, monomer solution, dispersant and powder mixture are mixed together to obtain a stable slurry. Monomers are non-ionic and they don't absorb on the ceramic surfaces. Hence, they do not compete with the dispersant [2]. Then, APS and TEMED are admixed consecutively for several minutes. TEMED is added if fast curing is required. Molds are used to shape the green samples. On completion of the curing of slurry within the mold, sample is quickly removed from the mold. Generally, AM and MBAM are used to prepare monomer solutions. Other common monomers are hydroxymethylacrylamide (HMAM), N-vinylpyrrolidone (NVP), methoxypoly (ethyleneglycol) monomethacrylate (MPEGMA). The selection of monomers depends on some parameters such as strength, stiffness, toughness of gel and toxicity of the starting chemicals [2].

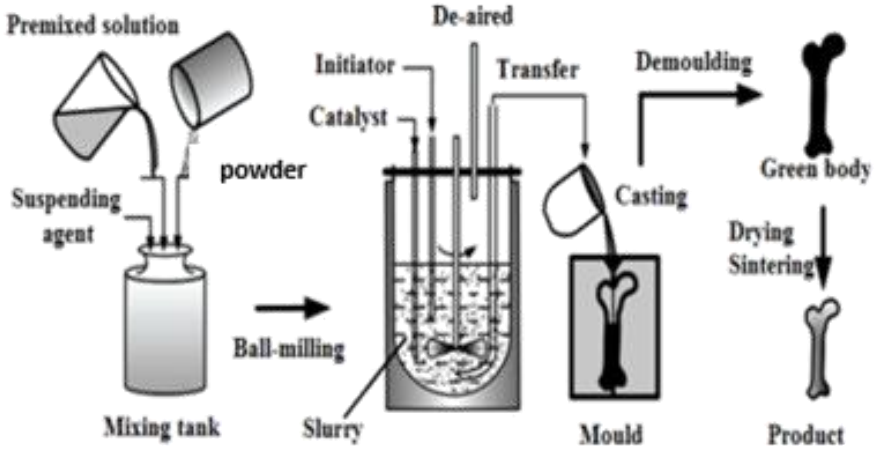

Figure 1.1. The mechanism of gel casting [3]

Figure 1.2 shows cross-linking mechanism of acrylamide monomers in the presence of APS and TEMED. Polyacrylamide is formed by cross-linking of the acrylamide monomers. APS with TEMED forms oxygen free radicals from the catalyst O_2, O_2^-, OH and H_2O_2 [4]. Then, the process is initiated by oxygen free radicals. Finally, the double bonds between CH_2 and CH in the AM and MBAM are broken. At this point, interconnection of linear monomers and crosslinking bisacylamide monomers develop [5,6].

Relative concentrations of TEMED and APS affect many physical parameters during gel casting. For example, increasing concentration of the initiators leads to a shorter average polymer chain length of AM and MBAM, resulting in higher gel turbidity and lower gel elasticity, and vice versa [6]. The gel elasticity is an important parameter during demolding of samples. For example, an undesirable gel elasticity may lead to tearing of samples during demolding or cracking of samples during burnout and sintering processes due to the formation of stress gradients on sample's surface induced during demolding. Figure 1.3 shows the effect of TEMED and APS amount on curing time. As a result of higher concentration of APS and TEMED, the amount of the free radical increases. As a result, cross-linking polymerization of the monomers is accelerated, resulting in shorter gelation time [7].

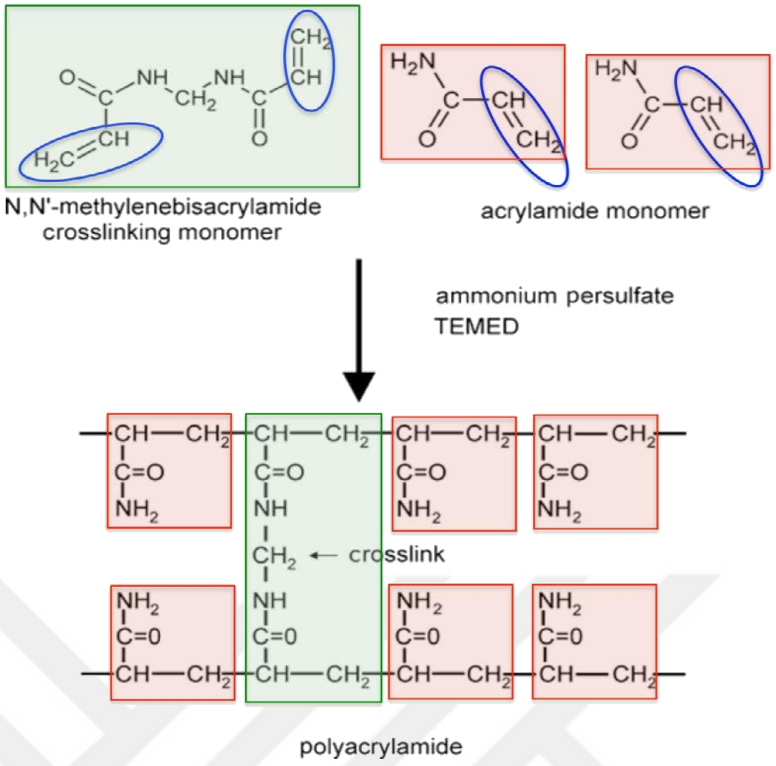

Figure 1.2. Cross-linking principle of monomers by TEMED and APS [8]

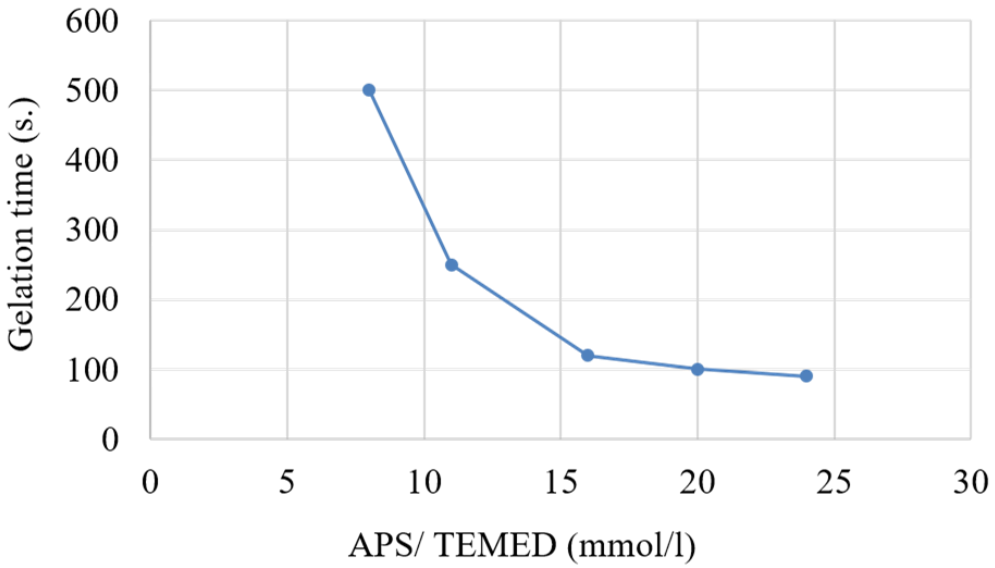

Figure 1.3. The effect of amount of APS/TEMED on curing time [9]

Figure 1.4 shows the effect of temperature on curing time at constant APS/TEMED concentration. The gelation time decreases with increasing temperature due to accelerated generation of the free radicals, which then accelerates cross-linking polymerization process [7]. Figures 1.3 and 1.4 indicate that cross-linking polymerization of monomers (or, gelation time) is controlled both APS/TEMED amount and temperature. Figure 1.5 shows the combined effect of APS and temperature. It is seen that gelation time can easily be altered with changing APS amount and temperature.

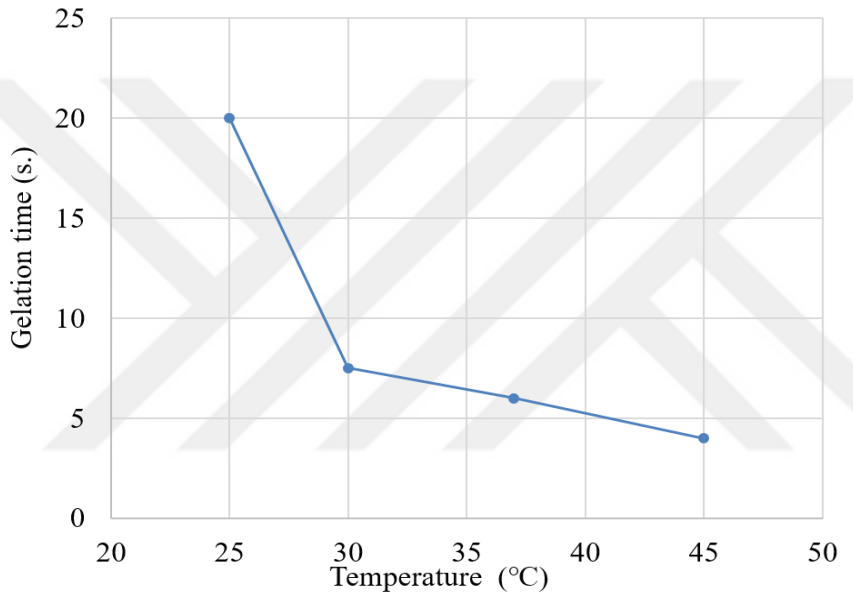

Figure 1.4. The effect of temperature on curing time with constant APS/ TEMED concentration [7]

There are a lot of ceramic fabrication methods, namely pressing, colloidal and plastic (or paste) methods, and they are classified in Figure 1.6. Unfortunately, the production of ceramic part at limited geometries is the main disadvantage of ceramic fabrication methods such as mostly used die pressing. Gel casting belongs to colloidal processing group to produce 3-D complex shapes at near net dimensions.

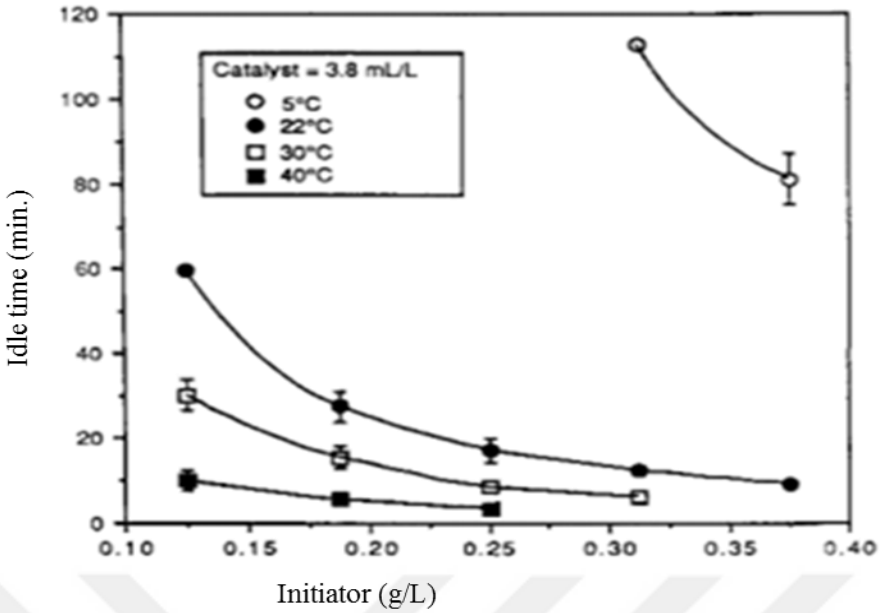

Figure 1.5. Combined effect of APS and temperature on gelation time [10]

Table 1.1 compares the conventional manufacturing techniques to fabricate complex ceramic geometries. Large numbers of complicated and small parts can be successfully produced by injection molding. The main disadvantage of injection molding is very high tooling cost at different geometries [11]. Also, binder removal duration is very long. Slip casting and gel casting are similar methods in that a stable slurry is required to prevent settling of particles. Generally, slip casting employs mostly gypsum mold to suck water by means of capillary pores. Unfortunately, there are some limitations in slip casting with respect to maximum achievable thickness. Moreover, there are many sources of defects such as density gradients, entrapped air bubbles, particle segregation, leaching of soluble species, etc. The main advantage of gel casting is the high degree of homogeneity in the slurry due to cross-linking of the monomers, yielding high quality final ceramics with minimum molding defects. Near net shape ceramics such as gears and rotors are shown in Figure 1.7. In addition, high green density and stiffness can be achieved by gel casting process [12].

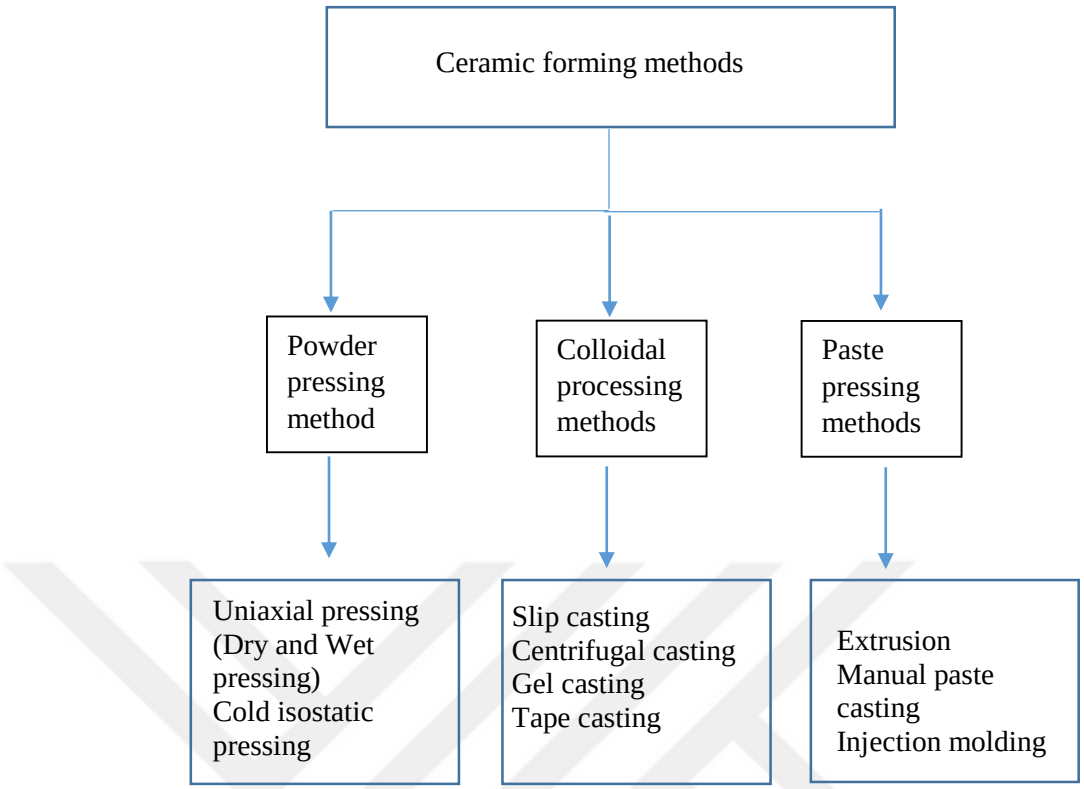

Figure 1.6. The ceramic forming methods [13]

Table 1.1. Comparison between Gel casting and other ceramic processes [2,14]

Parameters	**Slip Casting**	**Injection Molding**	**Gel Casting**
Initial Materials	Aqueous slurry	Thermoplastic mixture	Monomeric aqueous or non-aqueous
Molding Time	1-10 hours	10-60 seconds	5-60 minutes
Mold materials	Plaster	Metal	Metal, Glass, Polymer, Wax
Strength (Dried)	Low	N/A	Very high
Molding Defects	Minimal	Significant	Minimal
Thick/ Thin sections	Thick section needs longer casting time	Problem with binder removal for thick section	Both are OK.
Advantages	-Inexpensive molds -Manufacturing of hallow and solid parts	Mass production of complex parts	-Inexpensive molds -Manufacturing of hallow and solid as well as complex parts -High green density and stiffness
Disadvantages	Large tolerances	Binder removal prior to sintering	Binder removal prior to sintering

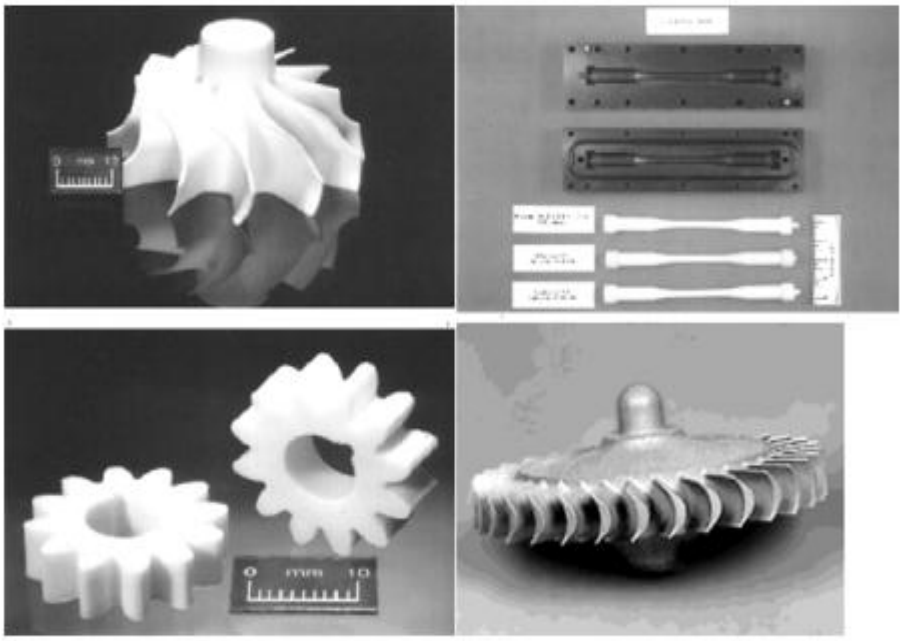

Figure 1.7. Examples of ceramics fabricated by gel casting [2]

Table 1.2 summarizes the mold materials used in gel casting. Many mold materials such as aluminum, metal, glass, wax and polymer, graphite and plaster, etc. can be used. Glass molds are very useful for production of thin films and tubes but at limited shapes. Neoprene rubber molds are very cheap but again they are limited by shapes. PVC molds are suitable for production of bars and rings. Aluminum is a very suitable and widely used mold material because it is cheaper and easily machined to desired shapes. Also, anodized aluminum molds have excellent surface properties with easier demolding [2]. Ultra high purity graphite molds can be machined but its porous structure causes some disadvantages. In brief, the selection of the mold materials depends mostly on the shape of materials.

Table 1.2. Mold materials for gel casting [15]

Materials	Advantages	Disadvantages	Applicability
Aluminum	Machinable, inexpensive	Poor release in some cases.	Widely used
Anodized aluminum	Machinable, inexpensive, better mold release than plain aluminum	-	Best performing mold material
Brass	Machinable	Corrodes, mold release a serious problem	Not recommended
Glass	Inexpensive, readily available, good release.	Limited shapes	Lab tests for plates, rods, and tubes
Graphite	Machinable, available at ultra-high purity	Porous	Special situations where purity is critical
Indium alloys	Castable, low melting point available (< 80°C for use as core material), reusable	-	Meltable cores
Neoprene rubber	Inexpensive, good mold release	Limited shapes	Often used as gasket material in large diameter PVC or metal ring molds and in glass plate molds
Plaster	Inexpensive, easily obtained	Porous, must be sealed or filled	Initial trials

After selection of a mold material, the most important problem is drying of the green bodies without introducing stress gradient and cracking. A fast rate of liquid evaporation can induce stresses, which easily leads to the formation of cracks. To prevent drying cracking, optimum rate of liquid evaporation must be experimentally determined [16]. Figure 1.8 shows drying of Si_3N_4 ceramics at different drying rates such as at room temperature in air and 65 wt% liquid desiccant PEG600 (polyethylene glycol 600) solutions. The all volume of the gelled body was in contact with PEG600, and hence PEG600 moistened all volume uniformly to control drying rate. It was reported that some cracks and defects were observed when gelled body was dried at room temperature in air due to higher drying rate [17]. When the gelled body was immersed in PEG600, the water was pulled out of gelled body into the PEG600 due to significantly higher osmotic stress in the PEG600 than in the gel cast body. In addition, the chemical potential of water to displace from the gelled body into the PEG600 was quite high and not limited by the saturation effects [18]. As a result of lower drying rate, the possibility of formation of residual stresses decreased and hence, crack didn't form in the gelled body [17]. A similar method was also

applied to dry conical radome ceramics. Figure 1.9 shows a nose cracked radome due to drying stress difference between nose and the rest of body in air (Figure 1.9) and gelled radome dried in PEG400 [18].

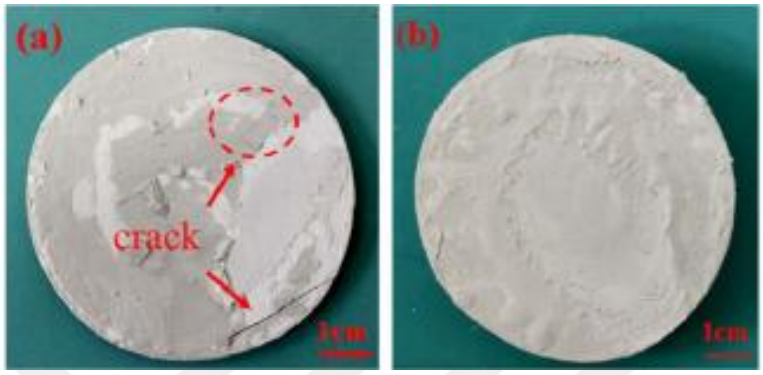

Figure 1.8. The macroscopic topography of green bodies under different condition; (a) drying at room temperature, (b) drying in 65 wt% PEG600 solution [17]

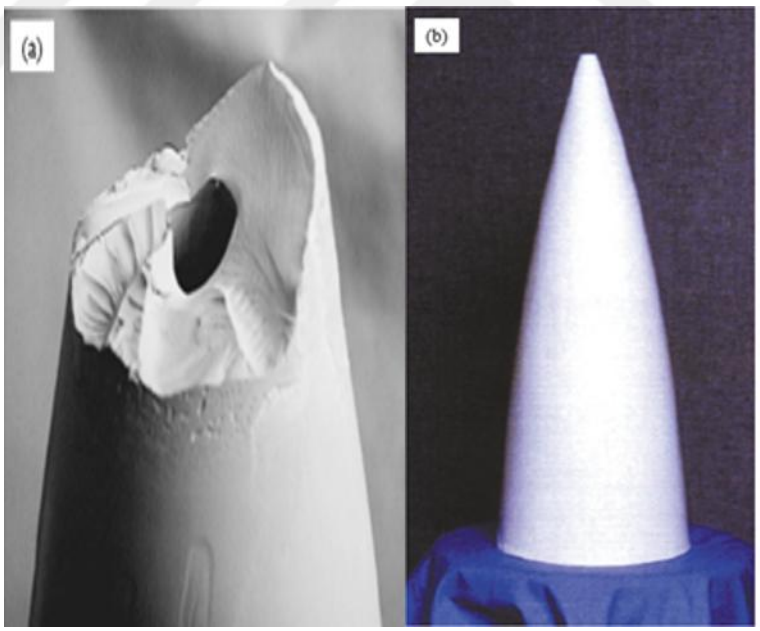

Figure 1.9. Sialon radome ceramics; (a) nose cracked green radome dried in air and (b) green radome dried in PEG400 [18]

1.2 Radome Materials

Radome is an enclosure material which protects an antenna or radar system from wind, rain, ice, UV, etc. Radome arises from combination of radar and dome. It is a material of electrically transparent to electromagnetic energy through which, the loss of power must be minimum in transmission. Therefore, material dielectric constant and loss tangent significantly affect the transmission loss. There are a lot of application areas for radome such as weather radar, aviation, maritime communications, surveillance, satellite communications, coastal surveillance, military and civil flight simulation, military and civil radar, microwave, and broadcast equipment [19]. The picture of a radome is shown in Figure 1.10.



Figure 1.10. Picture of a radome [20]

Radomes are solid wall structure or having walls separated by a core as in sandwich structure. The wall configurations are shown in Figure 1.11. The wall configuration of radome is determined depending on their application areas. Thin wall radome is a single layered homogeneous material and hence it is lightweight. The main advantage is its high transmission due to its low electromagnetic radiation absorption. Unfortunately, its low thermal insulation is the main disadvantage. The

half wavelength and thin wall radome are similar, but loss tangent is determined from the thickness of the wall transmission in half wavelength type. The main disadvantage of this type is weight and poor environmental protection [21]. Sometimes, thin wall and half wavelength do not provide good performance, especially such as bandwidth, weight or strength. Hence, multilayer structures are used instead. Common multilayer configurations are A-type sandwich, B-type sandwich and C-type sandwich [22]. The different dielectric materials can be used to obtain high strength, high transmission over a broad frequency band or multiple bands. They are composed of a core and outer layers. In the A-type sandwich structure, core is made up of high strength material and outer layers are made up of low dielectric constant materials. As a result of its configuration, it has higher strength than monolithic walls. The B-type sandwich is reverse of the A-type sandwich such that it provides very wide bandwidth at high incidents angles. Unfortunately, it has poor mechanical structure due to low density outer layers. High and low dielectrics of 5 layers are laminated in the C-type sandwich structure. The main advantage is the exhibition of a broad band performance couple with a low sensitivity. Unfortunately, its impact strength is poor in the sandwich structure. Finally, the last type is a graded porous structure where porosity lowers the dielectric constant and hence it has a high-power transmission efficiency. Also, its thermo-mechanical properties are better than the A-type sandwich. The main disadvantage is its complicated production. Also, moisture can be detrimental due to its porous structure [21, 22].

Solid wall construction is made from inorganic nonmetallic materials such as alumina and pyroceram to withstand high temperatures (above 1000°C). In contrast to inorganic materials, the useful temperature is 250°C for most organic materials [23].Water and carbon are very harmful to radome performance in that carbon absorbs electromagnetic radiation and reduces performance, and water has high dielectric constant with respect to radome material itself. Material dielectric constant and loss tangent also affect transmission loss during electromagnetic radiation. Low dielectric constant and loss are one of the desired properties. High strength, high thermal shock resistance and high thermal stability also are desired key properties [23].

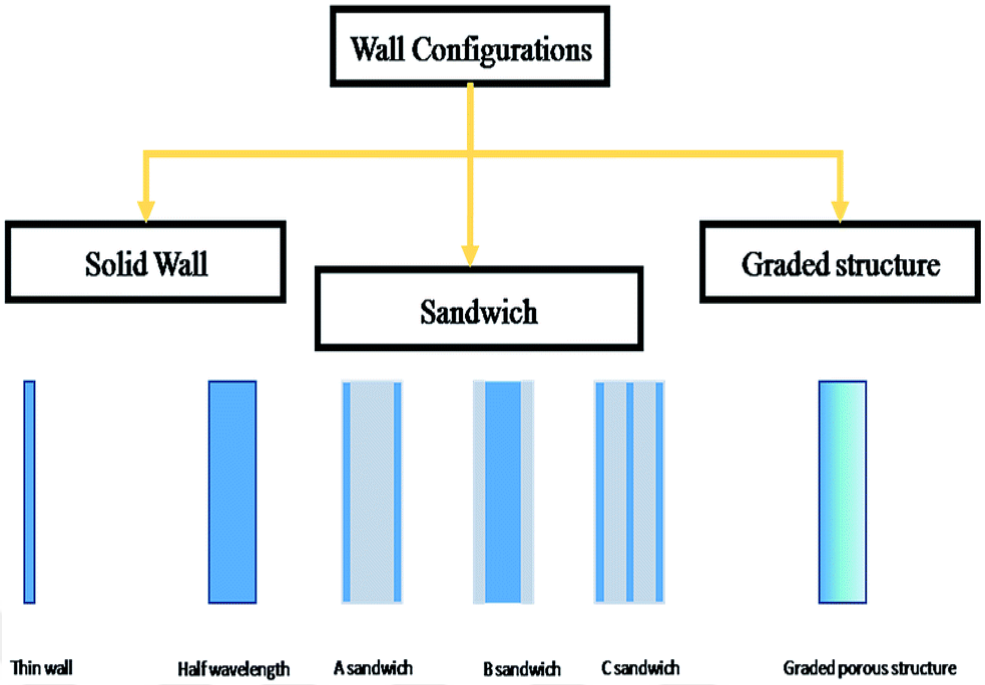

Figure 1.11. The wall configurations of radome [21]

1.2.1 Dielectric properties

Radio frequency (RF) range is between the frequencies of 300 GHz and 9 KHz [24] and microwave (MW) range is between the frequencies 300 MHz and 300 GHz [28]. Figure 1.12 shows frequency dependence of the dielectric polarization. Applied electric field causes separation of positively and negatively charged species within the structure, resulting in polarization. Electronic polarization occurs when positively charged nucleus displaces in the direction of applied electric field and electron cloud in the opposite direction. Similarly, displacement of negative and positive ions leads to ionic polarization. Ionic polarization occurs at lower frequencies than the electronic polarization because ions are heavier than electrons. Relaxation mechanism is valid for the ionic and electronic contributions in the GHz range. Permanent electric dipoles are aligned in the field direction. The prevention of mobile charge carriers by interfaces such as grain boundaries leads to space charge polarization at lower frequencies [26,27]. Total polarization is strongly dependent on the frequency range under consideration. Therefore, total polarization (P_t) can be defined as [25];

$$P_t = P_e + P_i + P_d + P_s \quad \textbf{(1.1)}$$

where P_e is electronic polarization, P_i is ionic polarization, P_d is dipolar polarization, and P_s is space charge polarization.

The relationship between dielectric constant and polarization can be defined as [29];

$$P = \varepsilon_0 X\, E = \varepsilon_0 (K-1)E \quad \textbf{(1.2)}$$

where ε_0 is permittivity of free space (8.8542×10^{-12} $F.m^{-1}$), K is relative dielectric constant ($F.m^{-1}$), X is susceptibility (m.kg.sec) or (cm.gr.sec) and E is applied electric field (V/m).

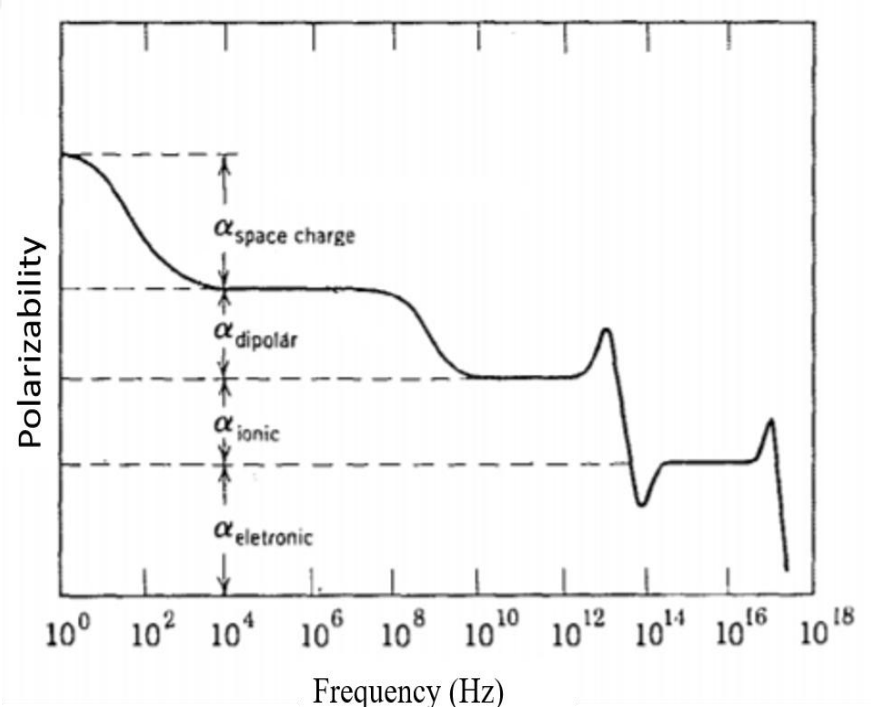

Figure 1.12. Dielectric behavior of materials depend on frequency [30]

Low dielectric constant and tangent loss are desired for radome applications. Hence, the dielectric properties are very important during selection of the candidate materials. Dielectric materials will reflect some incident energy, but radome must reflect minimum energy. The reflection decreases with decreasing dielectric constant of the materials. As a result, it has lower impact to radiation pattern and insertion loss (i.e., loss of total energy due to reflection and absorption) [31]. Power dissipated in dielectric materials also leads to insertion loss [32], which necessitates lower dielectric constants to decrease insertion losses. Insertion loss increases with increasing frequency due to decreasing in wavelength, because all light waves at vacuum have the same speed and the number of waves crossing by a given point in one second depends on wavelength [33]. The insertion loss (P) can be defined as [32];

$$P = 10 \log \left[\frac{P_0}{P_x}\right] \quad \textbf{(1.3)}$$

where P_0 is power out (Watt) and P_x is power in (Watt).

Dielectric constant also plays an important role in delay time of signal transmission because transmission speed of signal increases with decreasing dielectric constant. It is calculated as [34,35];

$$t_d = l.\sqrt{K}/c \quad \textbf{(1.4)}$$

where t_d is delay time (second), *l* is the metal line length (m), K is dielectric constant and c is the speed of light (m/second). For radome applications, low dielectric constant is ensured either by using low dielectric constant materials (e.g., Si_3N_4 (K=8.1) instead of Al_2O_3 (K=9.5)) [36] or introducing porosity to the dielectric materials. Figure 1.13 shows change in dielectric constant and loss tangent as a function of porosity in Si_3N_4. Dielectric constant decreases with increasing porosity [37] because the dielectric constant of air is near 1. In addition, pores increase the resistivity as a result of prevention of the charge carriers [38], resulting in lower

dielectric loss. Materials with pore can be thought of a composite between material itself and air. Therefore, dielectric constant in the presence of porosity can be easily defined by using a mixing law [39];

$$\ln K = \sum_{x}^{n} (V_x \ln K_x) \tag{1.5}$$

where K_x is dielectric constant of each phase and V_x is volume fraction of each phase.

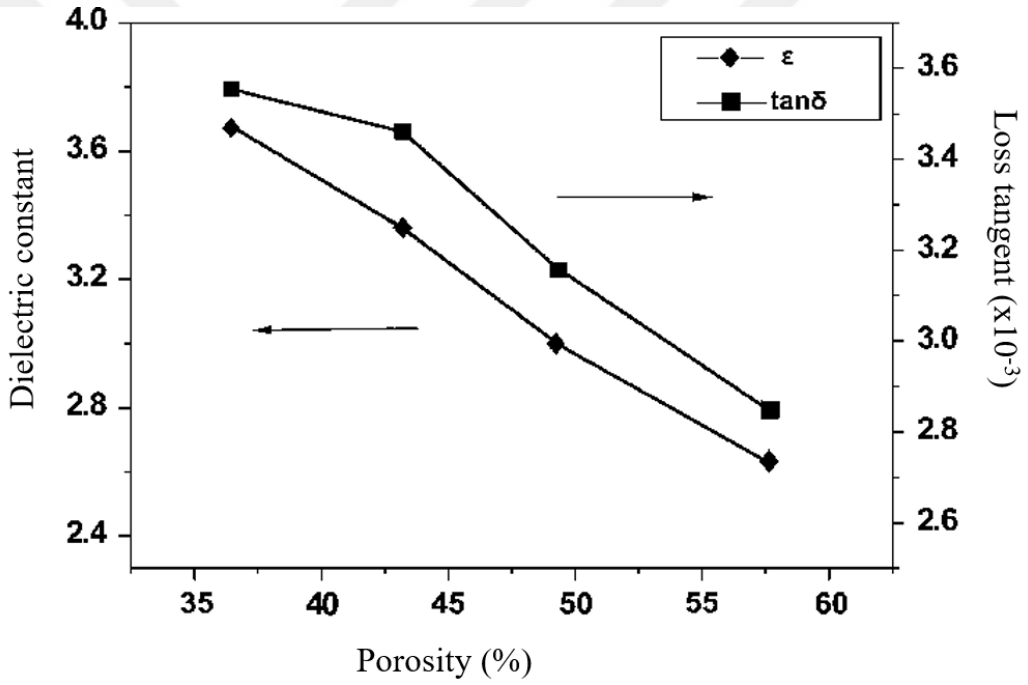

Figure 1.13. The effect of the amount of porosity on dielectric constant of Si_3N_4 [37]

Lower dielectric properties are required but temperature dependence of dielectric constant and loss also affects the radome performance. Figure 1.14 shows temperature dependence of dielectric properties of Al_2O_3. Dielectric constant and loss at 9.5 GHz increase from 9.6 and 0.0001 at room temperature to 11.2 and 0.0011 at 900°C, respectively. Change in dielectric properties with temperature makes the

design of the radomes difficult and complicated because radome is faced with various temperature profiles during its cruise.

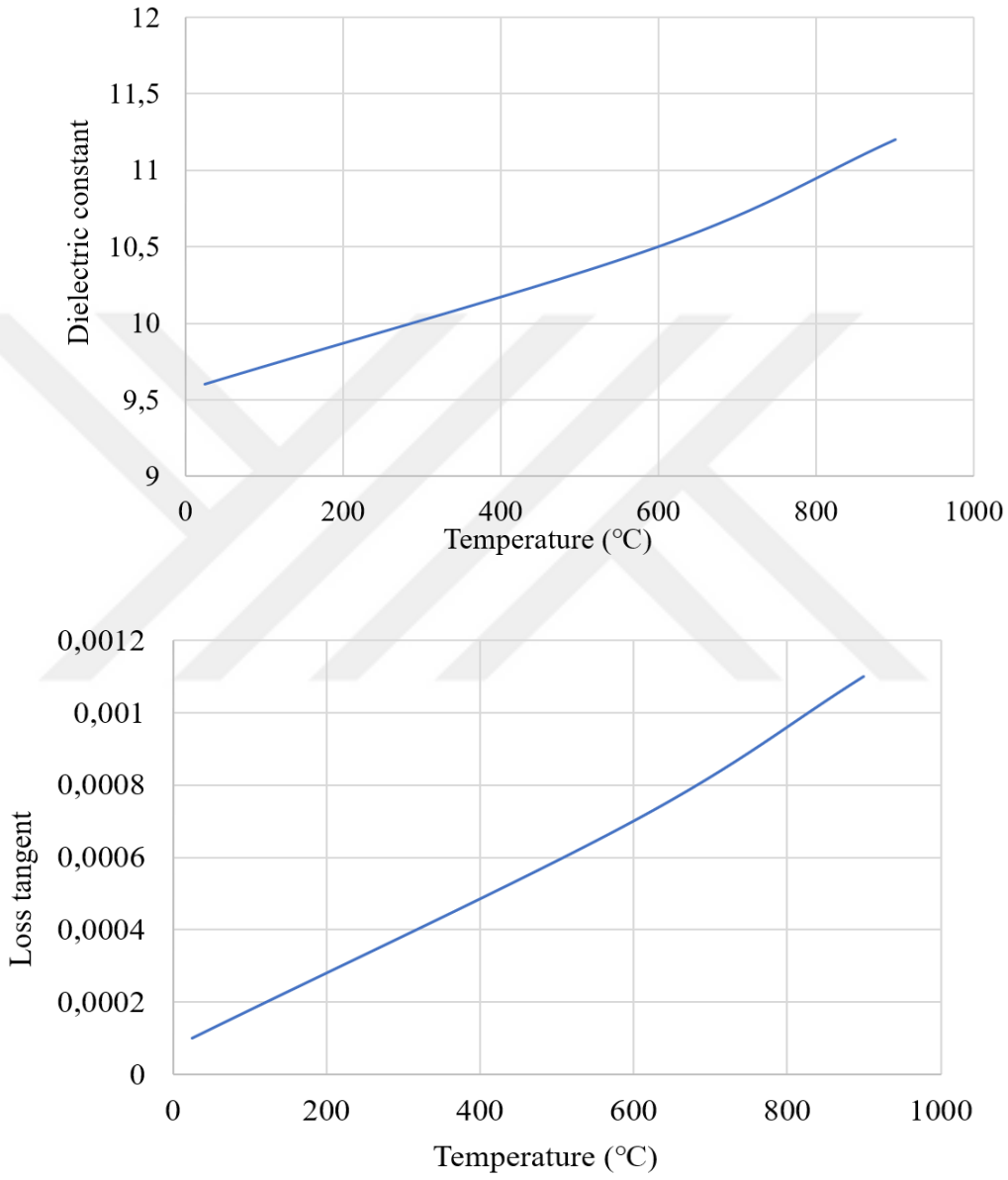

Figure 1.14.The loss tangent and dielectric constant of Al_2O_3 as a function of temperature [23]

1.2.2 Mechanical and Thermal properties

Materials to be used at high temperatures for structural applications should have high melting points. These materials are mostly nonmetallic inorganic materials and have low fracture toughness due to types of atomic bonding. Thermal stresses induced during service at elevated temperatures can easily result in cracks or failure, which is undesirable and limits the efficient usage of the components. Therefore, it is crucial to totally eliminate or at least limit the probability of failure caused by the thermal stresses [40]. They are induced due to temperature fluctuations and particularly tensile stresses easily weaken or even fracture the materials. Surface tensile stresses form if surface temperature is lower than the average temperature. The central compressive stresses are induced as a result of the higher center temperature [30]. Fracture occurs when the stress is sufficient to extend a crack thru the body. The ability of a material's resistance against weakening or fracturing under these conditions are called as thermal endurance, thermal stress resistance or thermal shock resistance (TSR) [30]. In addition to the magnitude of temperature change, mechanical and thermal properties also affect TSR [41]. TSR parameter is used to define crack propagation or crack arrest under a thermal stress. The critical temperature difference (ΔT) is defined as a TSR parameter of R (°C) for extremely rapid cooling and represented as [42];

$$R = \Delta T = \frac{\sigma_f \cdot (1 - \upsilon)}{\alpha \cdot E} \tag{1.6}$$

where σ_f is the flexural strength (Pa), υ is the Poisson's ratio, α is the thermal expansion coefficient (CTE) (ppm/°C) and E is the Young's modulus (Pa). However, in this expression, geometry of the material is not defined. R' (K.W/m) is defined as a second parameter of TSR which includes thermal conductivity (k, W/m.K) of material and represented as;

$$R' = \Delta T = \frac{\sigma_f \cdot k \cdot (1 - \upsilon)}{\alpha \cdot E} \tag{1.7}$$

Lower E and α together with higher k and σ_f values are preferred for higher TSR parameters. When k is included, R and R' values can significantly vary [42].

Porosity also influences TSR. Figure 1.15 shows the effect of porosity on Young's modulus of Al_2O_3 produced by spark plasma sintering and normal sintering. Young's modulus decreases with increasing porosity [43]. Hence, an optimization is required according to the porosity (or densification) level.

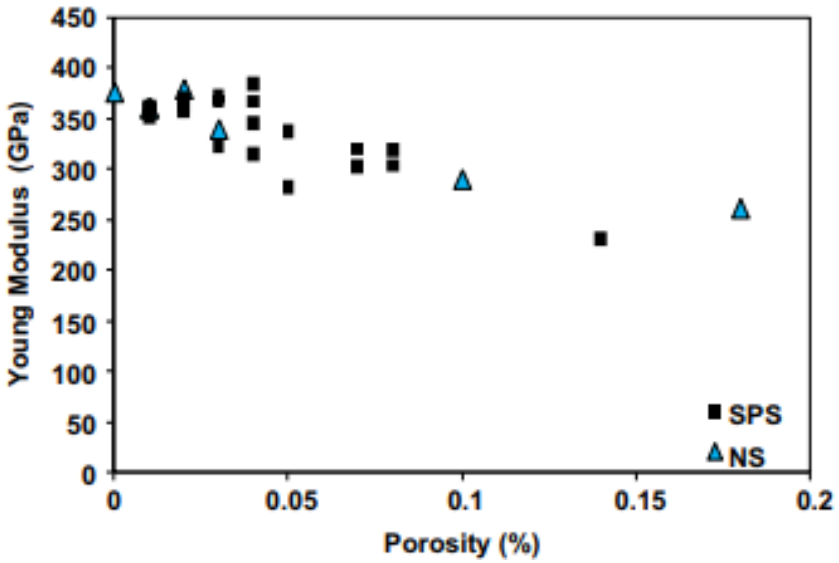

Figure 1.15. The effect of porosity on Young's modulus of micro-structured Al_2O_3 by natural sintering and spark plasma sintering [43]

There are a lot of candidate materials for radome applications such as Al_2O_3, pyroceram, $3Al_2O_3.2SiO_2$ (mullite), BN, BeO, $2MgO.2Al_2O_3.5SiO_2$ and Si_3N_4, etc. The material is selected by considering its mechanical, dielectric and thermal properties all together. Some candidate materials are compared in Table 1.3. First, water absorption is an important problem due to its high dielectric constant (78.5 at room temperature) [44]. Hence, selected materials must have 0% or very low water absorption, which states that densification level is very critical. Second, Young's modulus is important and it should be neither too low nor too high. A lower Young's modulus increases the thermal shock resistance (see Equations 1.6 and 1.7). For example, Young's modulus of mullite (220 GPa up to 700°C) and pyroceram (120 GPa at 25°C) are lower than that of Al_2O_3 (380 GPa at 25°C), but thermal shock

resistance of Al_2O_3 is worse than those of mullite and pyroceram. However, too low Young's modulus considerably degrades the mechanical properties. Third, higher dielectric constant can limit the radome performance, so lower dielectric constant is required in terms of signal transmission delay time. For example, signal transmission delay time of mullite is 17 % less than that of Al_2O_3 due to higher dielectric constant of the latter (6.6 for mullite vs. 9.6 for Al_2O_3 at 25°C and 10-40 GHz) (see Equation 1.4). SiO_2 has very low dielectric constant (3.5 GHz at 25°C and 10-40 GHz) and also exhibit very good thermal shock resistance, but it has very low Young's modulus (50 GPa), which can arise severe disadvantages from mechanical point of view. Also, greater change in dielectric properties with temperature can lead to design problems over wide-frequency band operations because radome is faced with various temperature profiles during its cruise. The dielectric constant change (per 100°C) in Al_2O_3, pyroceram, mullite, BN and BeO are 1.20 %, 0.5%, 0.4 %, 0.6 %, and 1.5 %, respectively. The change in dielectric constant with temperature of mullite is among the lowest. Sintering of materials are also important during selection. For example, Si_3N_4 requires very high sintering temperature (1825-2080°C) and atmosphere control against oxidation [45]. BeO is a toxic material [46] and BN requires hot-pressing for densification [47]. As we consider electrical properties of mullite, it has low dielectric constant. In addition, it has a low thermal expansion coefficient [48], which makes mullite a suitable candidate material for radome applications.

To summarize, there are some candidate materials having excellent properties to be used for radome applications. They must be selected based on their temperature-dependent dielectric, mechanical and thermal properties. Moreover, the physical properties are interrelated such that porosity lowers Young's modulus improving the TSR but, at the same time, can degrade flexural strength. Therefore, properties must be optimized based on the radome requirements such as velocity, flight time, vibration, temperature fluctuation, etc.

Table 1.3. Examples of candidate materials for radome applications [23]

Materials	Flexural strength (MPa)	Young's Modulus (GPa)	Thermal Expansion Coefficient (ppm/°C)	Thermal conductivity (W/m.K)	Thermal Shock Resistance (TSR)	Dielectric constant	Dielectric Loss
Al_2O_3	270 (25°C) 250 (500°C) 220 (1000°C)	380 (25°C) 350 (500°C) 285 (1000°C)	6.5-8.1 (25-1000°C)	38 (25°C) 29 (100°C) 13 (500°C)	Fair	9.6 (25°C, 10-40 GHz) 10.3 (500°C, 10GHz) 11.4 (1000°C, 10GHz)	0.0001 (10 GHz, 25°C), 0.0005 (10 GHz, 500°C) 0.0014 (10 GHz, 500°C)
Pyroceram 9606	235 (25°C) 200 (500°C) 75 (1000°C)	120 (25°C 120 (500°C) 100 (1000°C)	3 (25°C) 7.8 (120°C) 3.8 (500°C)	3.8 (2 °C) 3.2 (500°C) 2.9 (1000°C)	Good and better than Al_2O_3	5.7 (25°C, 10-40 GHz) 5.8 (500°C, 10GHz) 6.1 (1000°C, 10 GHz)	0.00025 (25 °C, 10-40 GHz) 0.001 (500°C, 10 GHz) 0.0016 (750 °C, 10 GHz)
BN	130 (25°C) 85 (500°C) 25(1000°C)	95 (25°C) 70 (500°C) 50 (750°C)	3.2	25.1 (100°C) 18.8 (500°C) 12.6 (1000°C)	Very good	4.5 (25°C, 10-40 GHz) 4.6 (500°C, 10 GHz) 4.78 (1000°C, 10GHz)	0.0006 (500°C, 10 GHz) 0.0009 (750°C, 10 GHz)
BeO	260 (25°C) 225 (400°C) 150 (800°C)	320 (up to 400°C) 300 (500°C) 250 (800°C)	8 (20-100°C) 7.7 (20-500°C) 9.1 (20-1000°C)	293 (20°C) 92 (500°C) 50 (750°C)	Very good	6.6 (25 °C, 10-40 GHz) 7.2 (500°C, 10GHz) 8 (1000 °C, 10GHz)	0.0003 (25°C, 10 GHz) 0.0006 (25°C, 36 GHz) 0.0014 (100°C, 10 GHz)
Si_3N_4	425 (25-1000°C)	310 (25-1000°C	3.2	21 (20°C) 13.4 (1000°C)	Excellent	7.9 (25°C, 10-40 GHz) 8.2 (750°C, 10 GHz)	<0.005 (25°C, 10-40 GHz) <0.005 (700°C, 10 GHz)
Mullite	Tensile 130 (25°C) 100 (700°C)	220 (up to 700°C)	4 (20-500 °C 4.5 (20-1000°C)	6.3 (25-600°C)	improved thermal shock with respect to Al_2O_3	6.6 (25°C, 10-40 GHz) 6.7 (700°C, 10 GHz)	<0.001 (25°C, 10-40 GHz) <0.0045 (25-750°C, 10 GHz)
SiO_2	44 (25°C) 54 (500°C) 66 (1000°C)	50 (25-850°C)	1.5 (25-800°C)	0.6 (25-900°C)	Very good	3.5 (25°C, 10-40 GHz) 3.55 (500°C, 10GHz) 3.8 (1000°C, 10GHz)	<0.0006 (25°C, 10-40 GHz) 0.001 (500°C, 10-GHz) 0.0016 (750°C, 10GHz)

1.3 Mullite Materials

Figure 1.16 shows a phase diagram between Al_2O_3 and SiO_2. The solid solution

between Al_2O_3 and SiO_2 is called as mullite and it has several Al:Si ratios corresponding to $3Al_2O_3.2SiO_2$ and $2Al_2O_3.SiO_2$, but the former is the only stable compound under atmospheric pressure. The eutectic temperatures of silica–mullite and mullite-Al_2O_3 are 1595°C and 1840°C, respectively [49]. Incongruently and congruently melting of mullite is observed at 1810°C and 1900°C±20°C, respectively [50]. A liquid phase of mullite composition is obtained after congruent melting, but the products are corundum (α-Al_2O_3) and liquid. The congruent and incongruent melting depend on the presence of corundum in the system because the precipitation of α-Al_2O_3 is assisted by α-Al_2O_3 nuclei. [50]. Tromer et al. [51] reported that α-Al_2O_3 does not form at slow cooling rate. As a result of homogenization of the starting materials, a stable solid solution composition is obtained. The refractoriness increases with increasing Al_2O_3 amounts [51].

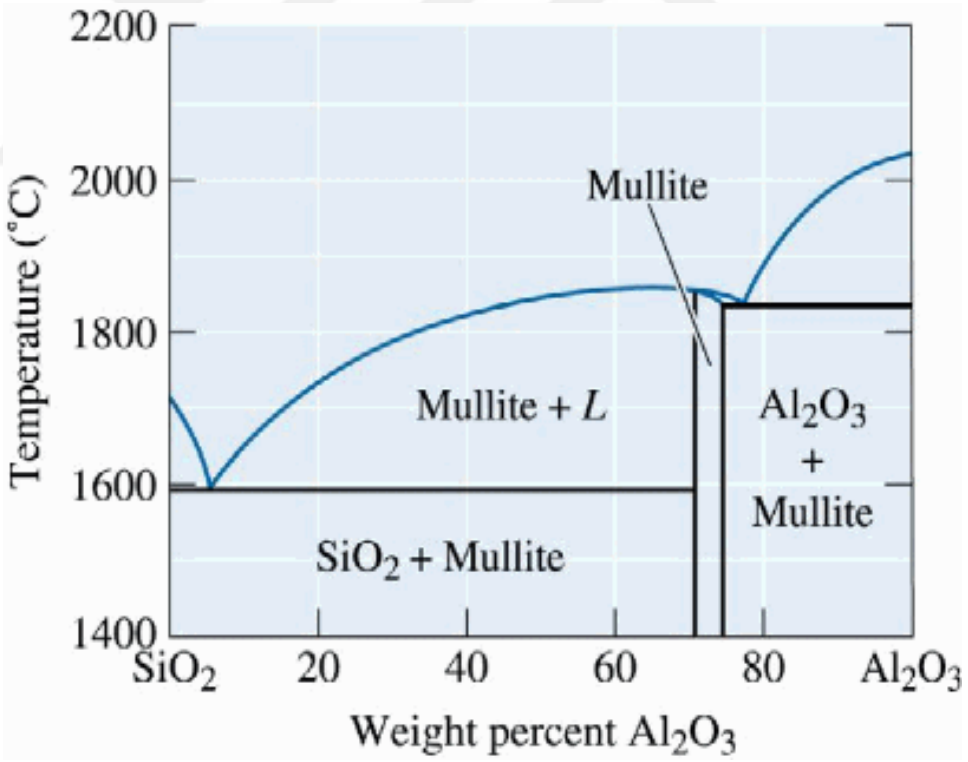

Figure 1.16. Al_2O_3-SiO_2 phase diagram [52]

The crystal structure of mullite is shown in Figure 1.17. Mullite has an orthorhombic crystal structure. AlO_6 chains at the octahedral sites are parallel to the

crystallographic c axis. They are cross-linked by $(Al,Si)O_4$ at the tetrahedral sites which form double chains parallel to the c axis [53].

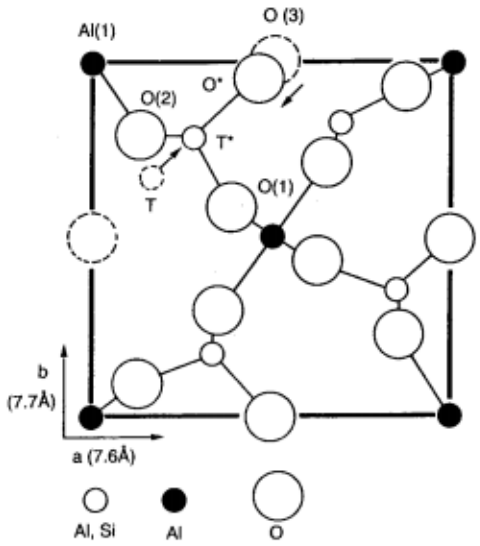

Figure 1.17. The crystal structure of mullite [54]

Mullite ceramics are important for advanced structural and electronic applications due to their suitable properties such as shown in Table 1.4. Although its low fracture toughness can limit its application areas, it has excellent creep resistance and thermal shock resistance at high temperatures. Hence, it's commonly used for high temperature applications. As a result of high creep resistance of mullite at above 1500°C, there happens no plastic deformation up to 900 MPa [55].

Table 1.4. Properties of mullite ceramics [36, 56-60]

Properties	Values
Hardness (HV)	1070-1120
Strength (MPa) 25°C	~200
Young's modulus (GPa)	143-230
Thermal conductivity (W/m.K) (full crystalline ceramic)	6 at 20°C 3 at 1400°C
Thermal expansion coefficient (10^{-6}/K) (20-1400°C)	4.5
Dielectric Constant Up to 14 GHz	6.5-8.1
Poisson's ratio	0.23-0.26
Fracture toughness, MPa.$\sqrt{m}$	2.25-2.55

1.4 The review of literature

Gel casting method is highly versatile method to manufacture large and 3D complex parts. It has been successfully applied to Al_2O_3 [10], Si_3N_4 [61], $PbZrTiO_3$ [62], ZrO_2 [63], etc. However, gel casting of mullite has not been studied extensively in literature. There are several studies concerning fabrication of porous mullite ceramics by gel casting. Porous mullite can be used for industrial and environmental applications such as support for catalytic agents, sound adsorbing materials, etc. [31]. Ya-Fei et al.[64] studied gel casting of porous mullite using mixtures of kaolinite and aluminum hydroxide at different ratios and sintered at different sintering temperature between 1300°C and 1600°C. They examined the effect of raw materials and sintering parameters on pore size, pore size distribution and gas permeability. As a result of a glassy phase, the highest sintering shrinkage was observed in the specimen made from kaolinite with an open porosity of 8.6 to 35.8%. In general, the average pore size decreased in the porous ceramics with increasing sintering temperature. The average pore size was 0.76, 0.9, 1.17, 1.31 μm at temperature between 1300°C and 1600°C, respectively.

The effect of different types of binders (silica-based, SiO_2-B_2O_3 mixture and silicon particles) on microstructure and properties of fibrous mullite ceramics fabricated by TBA- (Tert-butyl alcohol) based gel casting was investigated by Xiaojing et al. [65]. All products had high porosity (> 84%) and hence exhibited very low density and thermal conductivity. They reported that the types of binders strongly affected tailoring the inner structure of the porous ceramics. For example, after sintering at 1500°C with SiO_2binder, very low compressive strength was obtained due to high melting point of SiO_2. The other product with SiO_2 and B_2O_3 binder had higher compressive strength due to low viscosity of binders.

1.5 Objective

One of the most important ceramics for advanced structural and electronic applications is mullite due to its suitable properties such as excellent creep resistance and thermal shock resistance at high temperatures, and low dielectric properties for substrate and radome applications. In this thesis, it was aimed to investigate

fabrication of mullite ceramics by gel casting method because this method has not been studied to produce dense mullite ceramics in literature. Therefore, gel casting parameters such as monomer types and their ratios, effect of initiator and catalyst were studied in detail. Moreover, densification behavior, dielectric properties (dielectric and tangent loss), mechanical properties (fracture toughness, hardness, Young's modulus and flexural strength) and thermal properties (thermal expansion coefficient, thermal conductivity and thermal shock resistance) were characterized and carefully evaluated for a possible radome application. Green machining was also carried out to make a 3D product.

CHAPTER 2

EXPERIMENTAL MEDHODS

Mullite ($3Al_2O_3.2SiO_2$, Nabaltec), titanium oxide (TiO_2, Aeroxide, P-25 Evonik) were used as starting materials. The properties of mullite and TiO_2 are tabulated in Tables 2.1 and 2.2, respectively. Acrylamide (AM) (Sigma, 40 wt% solution, C_3H_5NO) and metyhlenebisacrylamide (MBAM) (Sigma-Aldrich, $C_7H_{10}N_2O_2$) were used to prepare monomer solutions. Monomer stock solutions (14wt %) at various AM/MBAM ratios of 6, 9, 12, 15, 20 were prepared by magnetic stirring and their weight percentages are given in Table 2.3.

Table 2.1. Properties of mullite [66]

Properties	Values
Mineralogical composition	90-95 % mullite 5-10 % glassy phase 1 % Al_2O_3
Specific density (g/cm^3)	3.13
Chemical composition	72% Al_2O_3 26% SiO_2 0.3% Fe_2O_3 0.2% TiO_2 0.05% CaO 0.1% MgO 0.2% Na_2O 0.6% K_2O
D_{50}, μm	3-5

Table 2.2. The properties of TiO_2 [67,68]

Properties	Values
Particle size, nm	21
Specific surface area, m^2/g (BET)	35 to 65
Melting point, °C	1855
Loss on drying (2 hours at 105°C)	$\leq$ 1.5%
Chemical composition	$\leq$ 0.3% Al_2O_3 $\leq$ 0.2 % SiO_2 $\leq$ 0.01% Fe_2O_3 $\leq$ 0.3 % HCl
Phases	85 % anatase and 15 % rutile

Table 2.3. The weight of AM, MBAM and water in monomer solutions and the solubility of MBAM in water

AM:MBAM ratio	H_2O in AM (gr)	AM (gr)	MBAM (gr)	Additional H_2O (gr)	Total H_2O (gr)	solubility of MBAM in water
20:1	8.957	5.971	0.299	29.543	38.5	0.78 %
15:1	8.775	5.85	0.39	29.725	38.5	1.01 %
12:1	8.681	5.788	0.48	29.819	38.5	1.25 %
9:1	8.465	5.643	0.627	30.036	38.5	1.63 %
6:1	8.062	5.374	0.896	30.438	38.5	2.32 %
3:1	7.055	4.703	1.568	31.446	38.5	4.07 %

A powder mixture containing mullite and 3.4 wt% TiO_2 together with 2 wt% dispersant (40 wt% ammonium salt of polyacrylic acid, Coatex P90) adjusted to dry weight percent of the total powders were mixed in a PP bottle by ball milling using ZrO_2 balls in water and then dried on a hot plate at 100°C with continuous stirring. Then, the dried slurry was put in a drying oven to evaporate remaining water completely for 48 hours. After drying, the powders were ground by mortar and pestle. Gel cast slurries (45 vol% solid) were prepared using powder mixture, monomer solution, ammoniumpersulfate (APS) ($(NH_4)_2S_2O_8$, Sigma-Aldrich) and tetramethylenediamine (TEMED) ($C_6H_{16}N_2$, Sigma-Aldrich) in a speed mixer (FlackTek, DAC 150.1 FVZ). First, monomer solution and powder mixture were mixed at 3500 rpm for 5 minutes, then APS was admixed at 3500 rpm for 5 minutes,

finally TEMED was admixed at 1000 rpm for 10 seconds. TEMED was not added to some gel cast slurries to investigate its effect on physical properties. The gel cast slurries with and without TEMED were poured in aluminum molds to shape green samples. Samples with and without TEMED were cured at room temperature and 70°C, respectively, as a function of time before they were demolded. The flowchart of the gel process is given in Figure 2.1. Viscosity behavior of the slurries with TEMED was determined by using Brookfield rheometer (Model DV3T).

Before sintering, binder burnout process was carried out. The burnout process schedule is given in Figure 2.2. Temperature-time profile for burnout process and temperature of liquid phase formation were determined from Thermogravimetric-Differential Thermal Analysis (Hitachi STA 7300). The samples were heated at 5ºC/min and sintered in air at 1450°C, 1500°C and 1540°C for 2 h. All samples were furnace cooled at 5ºC/min to room temperature. Phase formation was checked by using X-ray diffractometer (Rigaku, Miniflex600). The microstructures and elemental analysis were analyzed by a Scanning Electron Microscopy (SEM) and Energy Dispersive Spectrometry (EDS) (Hitachi, TM4000 Plus), respectively. Elements detected by EDS were calculated to stable oxide forms.

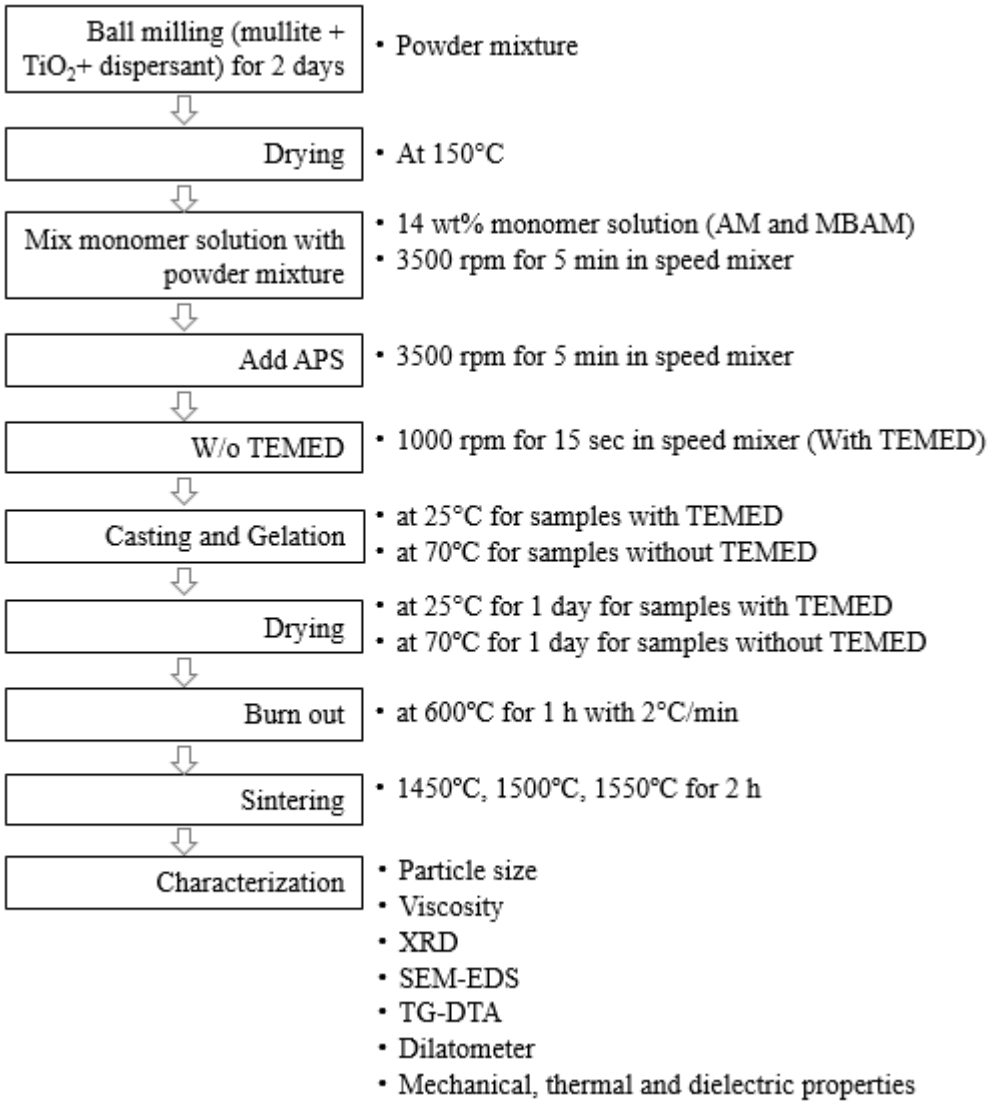

Figure 2.1. The flowchart of gel casting process

Archimedes' method was used to calculate bulk densities of the sintered ceramics. The dried sample weights were measured by a precision scale. The samples were boiled in a beaker for an hour. After cooling, the suspended weights in water were measured three times, and then averaged. Then, the samples were lightly wiped with moist cloth and then, measured in air. Then, density was calculated, according to [69];

$$B.D = \left[\frac{W_a}{W_e - W_x}\right] xd \qquad \textbf{(2.1)}$$

$$A.P\ (\%) = \left[\frac{W_e - W_a}{W_e - W_x}\right] x100 \quad \textbf{(2.2)}$$

$$W.A = \left[\frac{W_e - W_a}{W_a}\right] \quad \textbf{(2.3)}$$

where W_a is the dried weight (gr), W_x is the weight of sample in liquid (gr), W_e is the weight of sample impregnated with water (gr), and d is density of water at the measurement condition (g/cm^3),A.P is apparent porosity and W.A is water absorption.

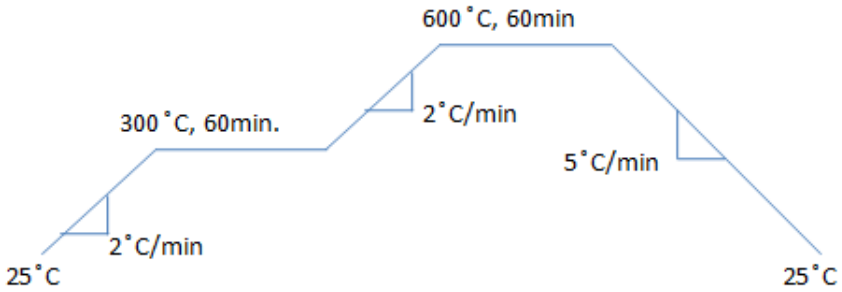

Figure 2.2. Temperature-time profile for binder burnout process

Hardness and fracture toughness of the sintered samples were determined by Micro Vickers hardness tester (Shimadzu HMV-G) applying 20 N load for 10 seconds. Before measurements, samples were ground at 120, 240, 320, 400, 600, 800, 1000 grit SiC papers by a grinding machine. Finally, samples were polished with 3µm and 1µm diamond cloths. Vickers hardness was calculated according to ISO 6507-1:2005 standard;

$$H = 01891\frac{P}{a^2} \quad \textbf{(2.4)}$$

where H is Vickers hardness, P is test force (N) and a is average length of diagonal lines of the indentation (mm). Fracture toughness was calculated using the formula given by Lawn et al. [70];

$$K_c = \delta \frac{\sqrt{E}.\mathrm{P}}{\sqrt{H} \cdot \sqrt{c^3}} \quad \textbf{(2.5)}$$

where K_c is fracture toughness (MPa.$\sqrt{\mathrm{m}}$), E is Young's modulus (MPa), c is half of the average crack length (m), a is half of the average length of indentation diagonal lines (m), and δ is a non-dimensional constant which is primarily a function of the indenter geometry. It is given as 0.026 for the hardness tester used.

Samples at nearly 3x4x50 mm were used to determine both elastic modulus and flexural strength. The surface of sample was ground to dimension at the green state and edge corners were also lightly ground before sintering. The flexural strength was measured by a 3-point bending test (Instron 5569, 500 kg load cell) with a cross head speed of 0.5 mm/min and 40 mm span length, according to ASTM standard C1161-02C;

$$S = \frac{3 \cdot P \cdot L}{2 \cdot b \cdot d^2} \quad \textbf{(2.6)}$$

where P is break force (N), L is support span (mm), b is specimen width (mm), and d is specimen thickness (mm). Elastic (or Young's) modulus was calculated by measuring natural resonance frequency method (Grindo Sonic MK5). The specimens were lightly hit from the middle by an impulser and a transducer located at the end of the specimen recorded the resultant resonance frequencies. The test was repeated until resonance frequencies were repeatable to each other. Young's modulus was then calculated according to ASTM standard C1259-15;

$$E = 0.9465 \cdot \left(m \cdot f_f^2 / b\right) \cdot (L^3/t^3) \cdot T_1 \quad \textbf{(2.7)}$$

$$T_1 = 1 + 6.585 \cdot (1 + 0.2023 \cdot \mu + 2.173 \cdot \mu^2) \cdot (t/L)^2 - 0.868 \cdot (t/L)^4 - \left[\frac{8.34 \cdot (1 + 0.2023 \cdot \mu + 2.173 \cdot \mu^2) \cdot (t/L)^4}{1 + 6.338 \cdot (1 + 0.1408 \cdot \mu + 1.536 \cdot \mu^2) \cdot (t/L)^2}\right] \quad \textbf{(2.8)}$$

where E is Young's modulus (Pa), m is mass of the bar (g), b is the width of the bar (mm), L is the length of the bar (mm), t is the thickness of the bar (mm), f_f is fundamental resonant frequency of the bar (Hz), and μ is Poisson's ratio. The statistical analysis of flexural strength was conducted by using Weibull approach. Probability of failure (P) vs. failure stress (S) curve was first drawn. Then, a linear fit was applied to the data points. The characteristic strength (σ) was finally calculated as [71];

$$\sigma = e^{c/m} \quad \textbf{(2.9)}$$

where m is slope of the curve and c is the constant variable in the linear equation of y=mx+c. The thermal conductivity was calculated from the thermal diffusivity, specific heat and density measurements from the following formula [72],

$$k = \alpha \cdot \rho \cdot Cp \quad \textbf{(2.10)}$$

where k is thermal conductivity (W/m.K), α is thermal diffusivity (m^2/s), ρ is density (kg/m^3) and Cp is specific heat (J/kg.K).The thermal diffusivity was measured using a laser flash apparatus (Netzsch LFA 457) and specific heat was determined by a differential scanning calorimeter (DSC) (Netzsch STA 449F3A). The thermal

expansion coefficient (CTE, ppm/°C) was measured using a dilatometer (Linseis, L-76 platinum) with a heating rate of 10°C/min in the temperature range of 25–600°C. The dielectric properties were measured by an impedance analyzer at 5 MHz (Hioki M3570).Parallel surfaces of the samples were first coated with Ag paste and then baked at 600°C for 15 min. The dielectric constant was calculated from capacitance measurement at room temperature according to the following formula [73];

$$K = \frac{C \cdot d}{\varepsilon_0 \cdot A} \qquad \textbf{(2.11)}$$

where K is dielectric constant, C is capacitance (F), d is thickness of specimen (m), ε_0 is permittivity of vacuum (F/m) and A is area of specimen (m^2). The microwave dielectric properties were measure during a network analyzer (Keysight, N1500A high temperature probe). For this measurement, the sample was two side lapped, rather than Ag coating.

The thermal shock resistance was determined by an indentation-quench method [74]. First, pre-cracking was done through indentation with a Vicker hardness tester. Then samples were heated to different temperatures of 200°C, 400°C, 600°C and kept for 20 minutes to provide temperature uniformity. Then, the samples were quenched into 3 liters water kept at 22°C. Then, the crack propagation and extension were measured using an optical microscope (Nikon, Eclipse MA-100).

CHAPTER 3

RESULTS AND DISCUSSION

3.1 Phase Analysis and Densification

Commercial mullite powder was produced by sintering the basic raw materials close to the melting or decomposition temperature (approximately, 1840°C), and then cooled down with high mullite forming rates. However, Table 2.1 shows that 5-10 wt% glass phase was reported, possibly due to vitrification. The exact chemical composition was selected in the stable single phase mullite solid solution region (see Figure 1.16) for the powder production. Then, the sintered pellets were mechanically crushed down to a defined size of d_{50}=3-5 μm [66]. XRD pattern of the as-received mullite powder is shown in Figure 3.1. All peaks belonged to mullite (Card number 00-015-0776). It is clearly seen that there is a background which corresponds to amorphous phase between 2θ ~ 10-30° already present in the mullite powder.

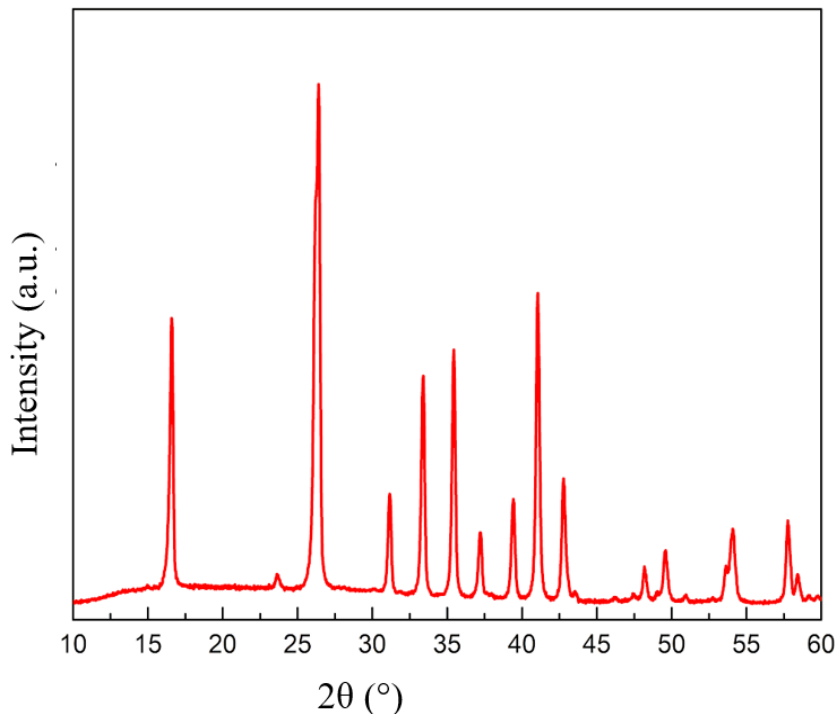

Figure 3.1. XRD pattern of the as-received mullite powder

Table 2.2 shows that TiO_2 is a mixture of anatase (Card number 00-021-1272) and rutile phases (Card number 00-021-1276). Figure 3.2 shows the XRD pattern of the as-received TiO_2 powder. Anatase and rutile phases are marked in the pattern.

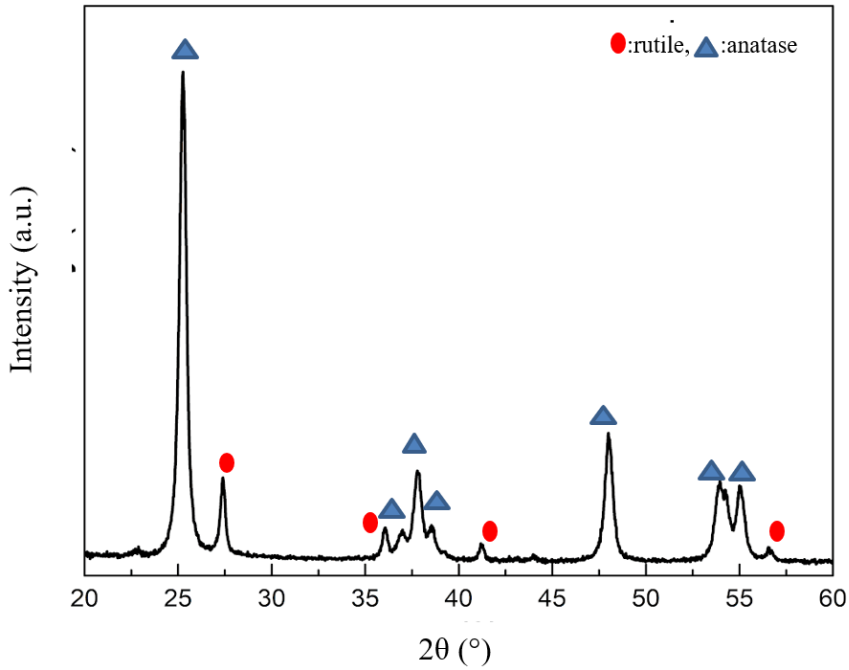

Figure 3.2. XRD pattern of the as-received TiO_2 powder

Ball milling was applied in order to decrease particle size of initial mullite powder. In order to increase the grinding efficiency, 2 wt% dispersant was added to increase the colloidal stability of the ground particles during milling. Figures 3.3 and 3.4 show the variation of particle size distributions of the mullite powder measured after ball milling. The median (d_{50}) particle size was decreased considerably with increasing milling time between 16 (0.51μm) and 30 hours (0.27 μm) and then remained almost constant up to 48 hours (0.28 μm). Therefore, 48 hours milling was applied in our study. After 48 milling, d_{10}, d_{90} and mean particle size were 0.16, 1.2 and 0.56μm, respectively. Figure 3.4 compares histograms after each ball milling step. Bimodal particle size distribution became narrower and near unimodal after 36 h ball milling. Figures 3.3 and 3.4 prove that d_{50} of 3-5 μm of the initial mullite powder (see Table 2.1) was successfully decreased to less than 0.3 μm, which was very suitable for colloidal processing methods.

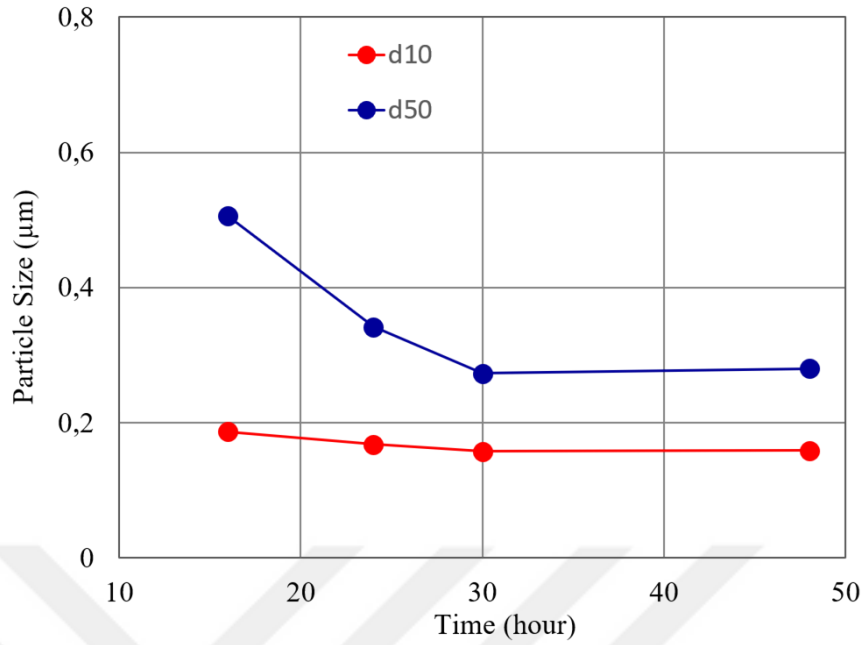

Figure 3.3. Median particle size variations as a function of ball milling time

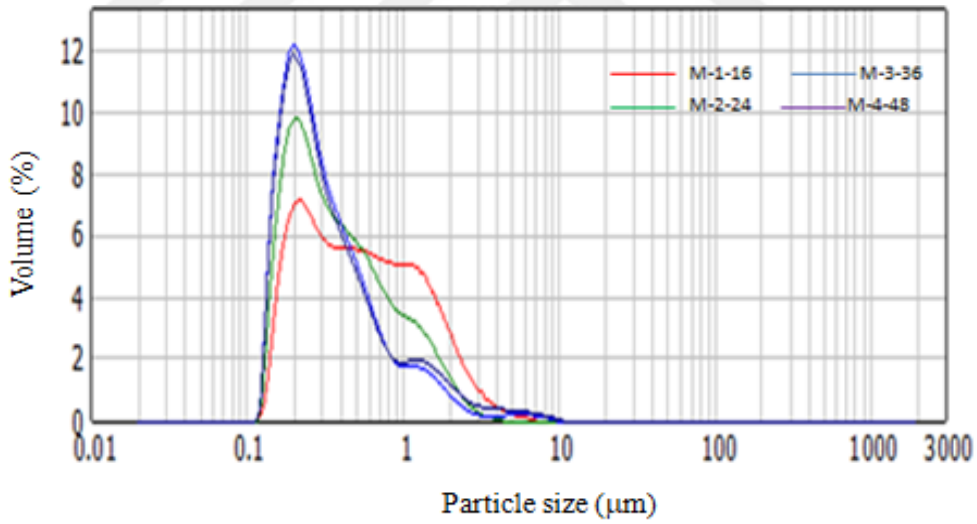

Figure 3.4. The particle size of mullite as a function of milling time

The isoelectric points (IEP) of mullite and TiO_2 occur at pH 5.8 and between 6-6.4, respectively, where the total positive charge is equal to the total negative charge at the IEP [75-76-77]. The stability of slurry is determined from zeta potential measurement in that a large negative or positive zeta potential value indicates good stability of slurry because of particles tending to repel each other [78]. An unstable slurry would be expected as zeta potential values are between +30 and -30 mV. For

colloidal stability of a dispersion, dispersants are commonly used. For example, anionic charges on particles are induced by addition of ammonium salt of polyacrylic acid [79,80], resulting in negatively charged surfaces by means of electrosteric stabilization mechanism. pH of the gel-cast slurry was measured to be 8.2 when dispersant was added, similar to reported pH value for mullite [75]. pH of 8.2 was more basic than respective IEPs, proving that all mullite and TiO_2 particles were negatively charged.

TEMED was added to accelerate curing process. Figure 3.5 shows starting time of curing in the slurries with TEMED at various AM/MBAM ratios of 6, 9, 15 and 20 from viscosity measurements. In this method, the very first starting time of curing process was easily monitored by means of sudden viscosity increase. Note that when the first curing started, it initiated from the bottom of the rheometer tube while upper part of the slurry was still wet. Drying times were ranged from 18 to 28 seconds in that the highest drying time of slurry was 27 seconds at the ratio of 20 and the lowest drying time of slurry was 18 seconds at the ratio of 9. Figure 3.5 strongly indicates that curing started very fast in less than 30 seconds, irrespective of the ratio, when TEMED was present. Note that a monomer solution at AM/MBAM ratio of 3 was not prepared due to about 2 wt% solubility limit of MBAM in water [81]. Therefore, 4.07 wt% MBAM was required to prepare a monomer solution at AM/MBAM ratio of 3 (see Table 2.3). A second monomer must be added as a cosolvent for the MBAM to prepare monomer solution at the ratio of 3 [81].

Figure 3.6 shows the completion time of curing with/out TEMED at various AM/MBAM ratios of 6, 9, 12, 15 and 20 in the aluminum molds. These values were ranged from 3.2 to 4.5 minutes for the samples with TEMED and from 35 to 65 minutes for the samples without TEMED. For example, the curing time was 65 minutes without TEMED and 3.2 minutes with TEMED at the ratio of 6.

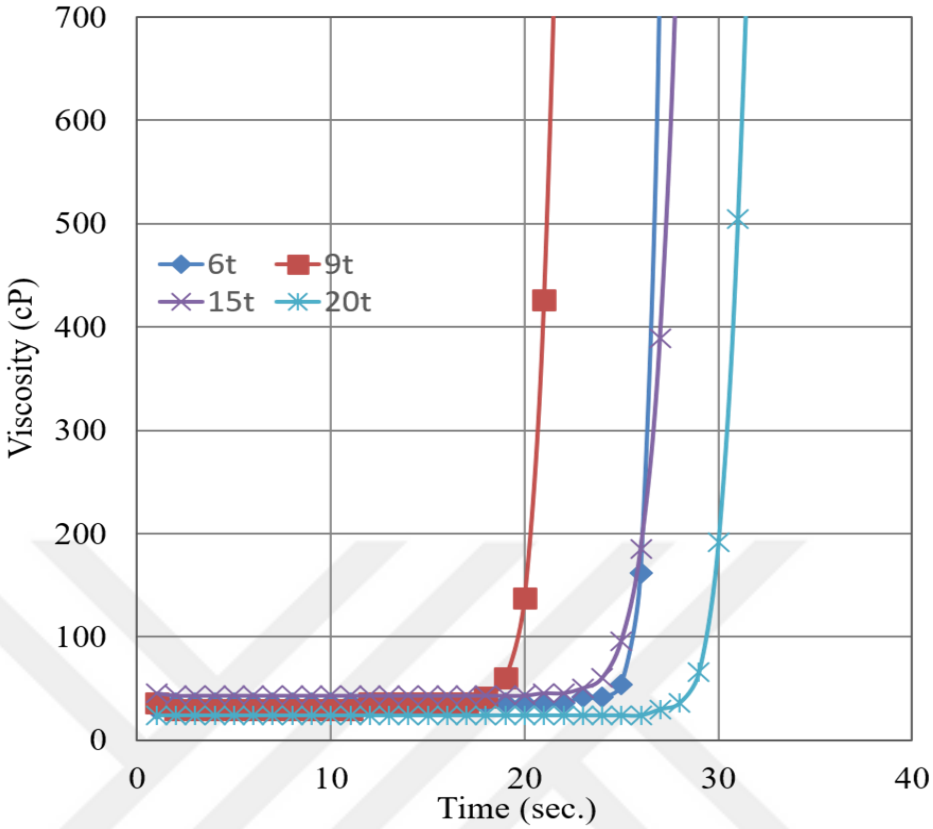

Figure 3.5. The curing of slurries with TEMED at different AM/MBAM ratios

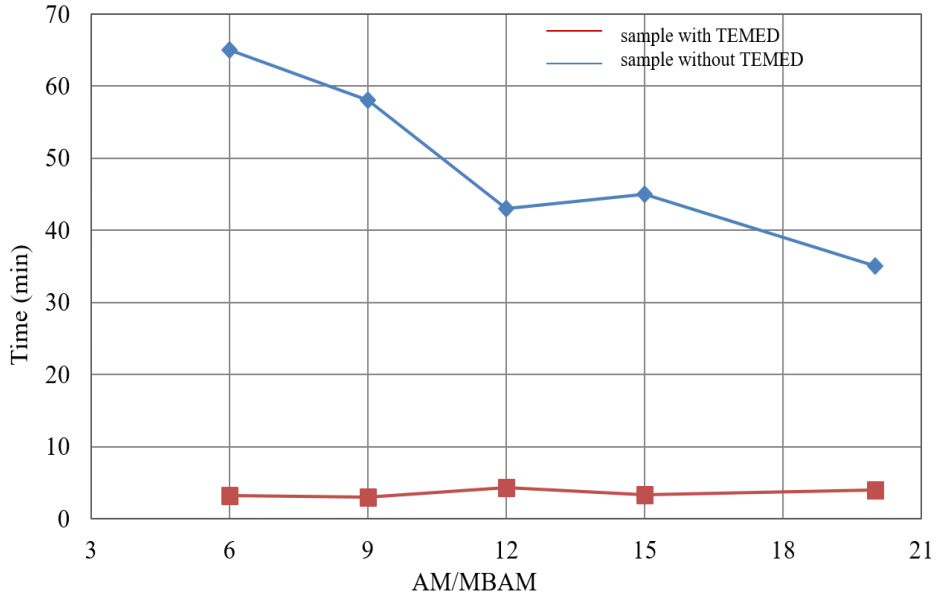

Figure 3.6. The complete curing time of slurries with/out TEMED at different AM/MBAM ratios

Curing starts at the bottom of the mold and continues upward. Viscosity measurement (Figure 3.5) indicates the start of the first curing time at the bottom, however, curing in a mold (Figure 3.6) indicates the completion of the curing as measured from the top of the cured slurry (or green sample). Curing starts at the bottom of the mold because the presence of oxygen hinders polymerization and gelation. As a result, spallation forms on the surfaces in contact with air during the curing process [82]. APS with TEMED forms oxygen free radicals which initiates the process. Hence, main aim of using TEMED with APS is to lower as well as to control curing time [5]. As soon as the curing is completed, gelled sample must be quickly removed from the mold to allow uniform drying from all surfaces. Otherwise, moisture or drying gradient is generated within the sample, causing stress build-up and ultimately cracking during either drying, burnout or sintering cycles.

Polymers used in gel casting must be removed from the green body before sintering. Therefore, binder removal is a critical step and must be carried out slowly to prevent cracking. Hence, a TG-DTA analysis was performed to determine burnout profile of the organic additives used and shown in Figure 3.7 for a green body prepared with TEMED at AM/MBAM ratio of 20. There were two low temperature endothermic peaks located nearly at 354°C and 450°C, indicating combustion of the organic additives due to mainly NH_2 groups [83]. Therefore, green samples were subjected to a burned out profile given in Figure 2.2. Initially, the polymer amount added was 7.3 % excluding water. However, the weight loss was nearly 6.2 % up to 600°C, and a weight loss of 7.3 % was reached at nearly 980°C (Figure 3.7). This delay in temperature stemmed from the different heating profiles in that the TG-DTA analysis was carried out continuously at 5°C/min without any given dwelling but the samples were heated at much lower heating rate of 2°C/min and with an intermediate step at 300°C for 60 min and an extra dwell for 60 min at 600°C (see Figure 2.2), allowing enough time for complete removal of the organics. Therefore, 7.12 wt% weight loss due to organic burnout was measured after the burnout schedule given in Figure 2.2, stating that almost all organics were successfully removed from the body.

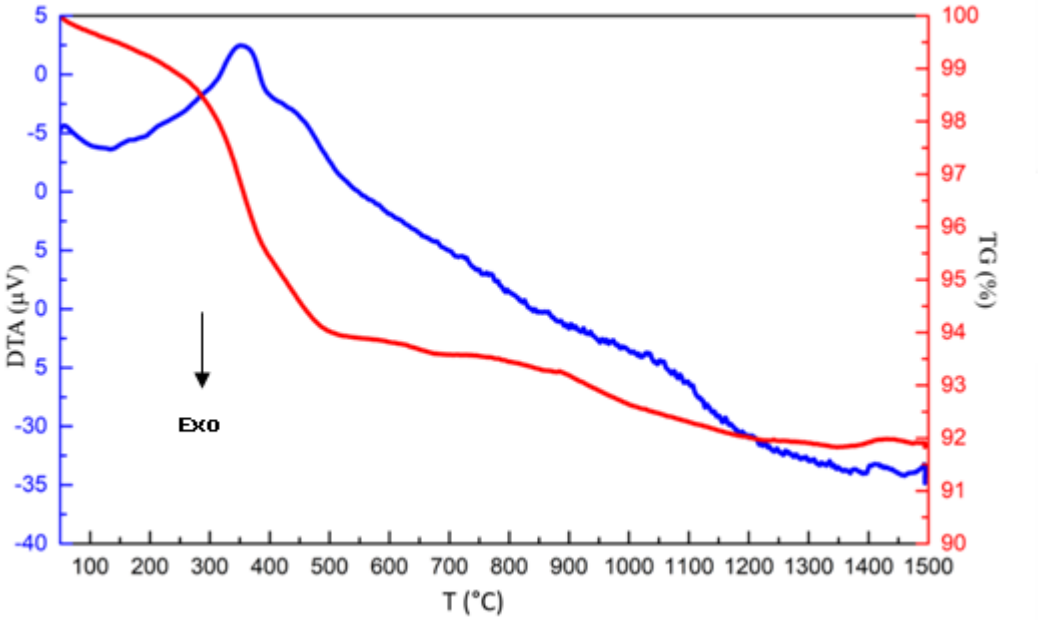

Figure 3.7. Differential thermal analysis of powder at AM/MBAM ratio of 20

Figure 3.8 shows the variation of relative density as a function of both sintering temperature and AM/MBAM ratios for the samples prepared without TEMED. All samples showed similar densification behavior irrespective of the monomer ratio. At 1450°C, the relative densities between 82 % and 84 % were obtained. Densification increased sharply and reached to 97-98.2 % relative density for all samples at 1540°C. The samples with TEMED also followed exactly the same densification paths. Figure 3.7 shows a slight endothermic peak located at nearly between 1400°C and 1450°C, which corresponds to a liquid formation. Therefore, an enhanced densification after 1450°C was attributed to the presence of a liquid phase formed by TiO_2. Solution-reprecipitation process during liquid phase sintering enhanced diffusion, resulting in sharp density increase after 1450°C. Similar densification results were also obtained in textured mullite ceramics doped with 3 wt% and 5 wt% TiO_2 [84]. These results suggest that all samples with and without TEMED can be sintered to relative densities as high as 97-98.2 % at 1540°C which states that AM/MBAM ratios and TEMED don't significantly change the relative densification. All mechanical, thermal and dielectric characterizations were carried out on samples sintered at 1540°C for 2 h, unless otherwise was stated hereafter. Table 3.1 summarizes the bulk density, relative density and apparent porosity of the samples prepared with/out TEMED at different AM/MBAM ratios. The apparent porosity (or

open porosity) was less than 0.62 %. In addition, water absorption was 0 % for all samples, stating that all pores were closed but little fraction of pores located on the outer surface was open.

Figure 3.7 further indicates that weight loss in the samples continued with increasing temperature, even after polymer burnout temperature of 980°C. The total weight loss up to 1500°C was nearly 8.2 % (7.3 % due to polymer burnout). A diffuse and shallow endothermic peak located at nearly 1100°C could be attributed to weight loss due to alkali metal volatilization. To prove possible weight loss other than organics, initial and final weights of the samples were measured after sintering and it was found that the weight loss was 0.89 % ±0.06, which was very close to the initial amounts of 0.6 wt% K_2O and 0.2 wt% Na_2O (see Table 2.1). K_2O and Na_2O volatilization has also been reported from silica melts containing SiO_2, CaO, Na_2O and K_2O between 1240°C and 1670°C [85].

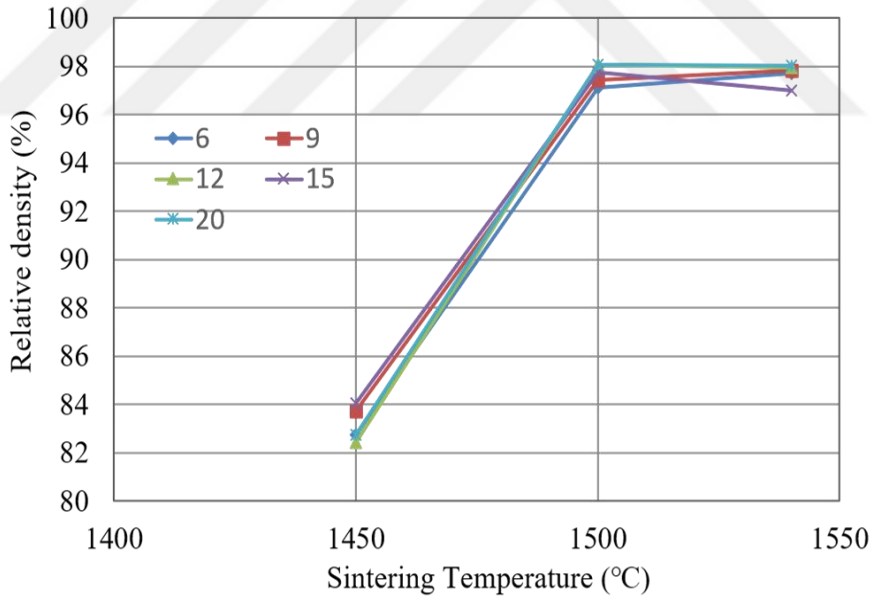

Figure 3.8. The Relative densities of samples without TEMED at different AM/MBAM ratios

Table 3.1. The bulk density, relative density, and apparent porosity of the samples prepared with/out TEMED at different AM/MBAM ratios (t refers to TEMED)

Samples	Bulk density (g/cm^3)	Relative density (%)	Apparent porosity (%)
6	3.07	98.0	0.29
9	3.06	97.8	0.24
12	3.06	97.9	0.62
15	3.04	97.0	0.00
20	3.07	98.0	0.36
9t	3.07	98.0	0.17
12t	3.09	98.2	0.18
15t	3.06	97.9	0.14
20t	3.07	98.2	0.16

Figure 3.9 presents XRD pattern of the sintered mullite prepared with TEMED at AM/MBAM ratio of 20. XRD reveals that, in addition to the main mullite phase (card number 00-015-0776), minor amounts of rutile TiO_2 (card number 00-021-1276) and corundum (α-Al_2O_3) (card number 01-071-1128) were detected. There was again a background between 2θ ~10-30°, although it was much less than that of the as-received powder (see Figure 3.1), which proved the existence of an amorphous phase remained after sintering.

The weight ratio of TiO_2 is important due to solubility limit of TiO_2 in mullite crystal structure. A total of 3.6 wt% TiO_2 was used in this study; 3.4 wt% of TiO_2 intentionally added (nano-sized P25) and 0.2 wt% TiO_2 from powder synthesis. After sintering at 1540°C for 2 h, TiO_2 was detected as rutile phase, which proves that TiO_2 did not completely dissolve in mullite. Hong and Messing [86] studied the phase development in diphasic mullite gel doped with 5 wt% TiO_2 (Ti-isobutoxide-derived fine TiO_2) and reported that only mullite and rutile were detected after sintering at 1650°C for 5 h. Unreacted rutile was attributed to the large initial particle size and/or nonuniform distribution. Gönenli and Messing [84] studied the effect of TiO_2 (3 and 5 wt%, nano-sized P25) on textured mullite and they did not observe any unreacted TiO_2 after sintering at 1500°C for 6 h. However, Baudin and Mayo [87] proposed the solubility limit as 3 wt% and reported that aluminum titanate (Al_2TiO_5)

formed above this limit. This phase was not detected by Hong and Messing [86] and Gönenli and Messing [84]. Duran et al. [88] also used 3.4 wt% TiO_2 to promote densification thru liquid phase sintering in reactive sintering of Al_2O_3 and $ZrTiO_4$ to produce mullite-ZrO_2 composites. It is acceptable to observe various results because the solubility limit of TiO_2 in mullite has been reported to be between 2 and 6 wt% depending on synthesis conditions [89]. Note that anatase transformation to rutile, using nano-sized P25 powder, was completed after heating to 700°C at 5°C/min [90]. In our case, unreacted TiO_2 can be attributed to the possible agglomeration during ball milling, rather than nonuniform distribution, because 2 wt% dispersant was added to colloidally disperse both mullite and TiO_2 particles. But, nano-sized TiO_2 particles definitely needed more dispersant than mullite due to its much lower particle size or higher surface area.

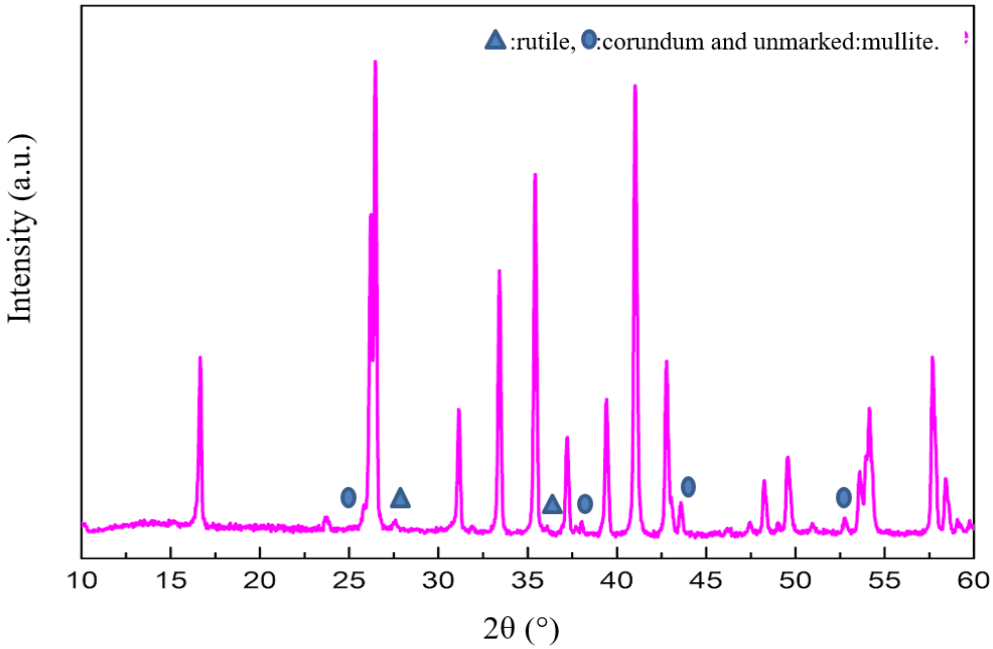

Figure 3.9. XRD pattern of the sintered mullite ceramics

Figure 3.10 shows backscattered SEM image of the sample prepared with TEMED at AM/MBAM ratio of 15. Glassy regions (represented as G) present like islands among the grains were clearly seen even after sintering (i.e., without devitrification) because the starting powder had 5-10% glassy phase (see Table 2.1). The existence

of the amorphous phase after sintering was also confirmed by XRD as seen in Figure 3.9. There were some hexagonal-shaped grains (or platelets), which were determined to be Al_2O_3 (represented as A) by EDS analysis. It was expected because starting powder had 1 % corundum (see Table 2.1). Figures 3.11 and 3.12 present backscattered SEM images of the samples prepared with/out TEMED at various ratios of AM/MBAM. Densities were close to each other (see Figure 3.8) and all samples had similar microstructure evolutions irrespective of TEMED and AM/MBAM ratios. In addition to the presence of glassy phase and plate-like Al_2O_3 grains, mostly elongated (anisotropic or acicular) and faceted mullite grains were observed in the microstructures. A presence of liquid (i.e., liquid phase sintering) was required for the formation of elongated grains [91]. Hong and Messing [92] investigated the effect of TiO_2 on microstructure development and reported that TiO_2 facilitated anisotropic grain growth of mullite by means of dissolution of smaller grains and precipitation on larger grains during liquid phase sintering. There are two other common features in the microstructures, that is, sharp-cornered and faceted pores, and white grains. The former is a common characteristic of the systems experiencing anisotropic grain growth whereby different growth velocities at different crystallographic directions cause random growth of grains, among which angular pores are inevitably generated [93]. The latter was analyzed by EDS and found that considerable amounts of ZrO_2 and TiO_2 were detected. ZrO_2 was possibly contaminated during milling of powder with ZrO_2 balls. In addition, EDS gave TiO_2 all the time but at various concentrations due to both TiO_2 dissolved in the mullite lattice and TiO_2 remained unreacted. Weight ratios of the main elements in the white spots and matrix were Zr/Al/Si/Ti=34.6/13.5/3.3/8.6 and Zr/Al/Si/Ti=0.0/37.5/12.5/2.1, respectively. Al and Si detected in the white spots were possibly due to signals from the neighboring matrix grains because the white spots were very small in size. Note that EDS analysis is a qualitative method and does not give exact ratios. Therefore, the analysis was repeated 6 times and then the values were averaged. These results show that the white spots contained mostly ZrO_2 and unreacted rutile TiO_2. Possible stable phases such as SiO_2, ZrO_2, Al_2SiO_5, $ZrTiO_4$ and Al_2TiO_5 were not detected in XRD within the detection limit except for rutile TiO_2 (see Figure 3.9). Gönenli and Messing [84] also reported similar white

grains in acicular Al-borate ($9Al_2O_3.2B_2O_3$) templated mullite ceramics and further explained that decomposition of Al-borate at high temperatures resulted in Al_2O_3 formation due to the evaporation of borate which then precipitated to the grain boundaries.

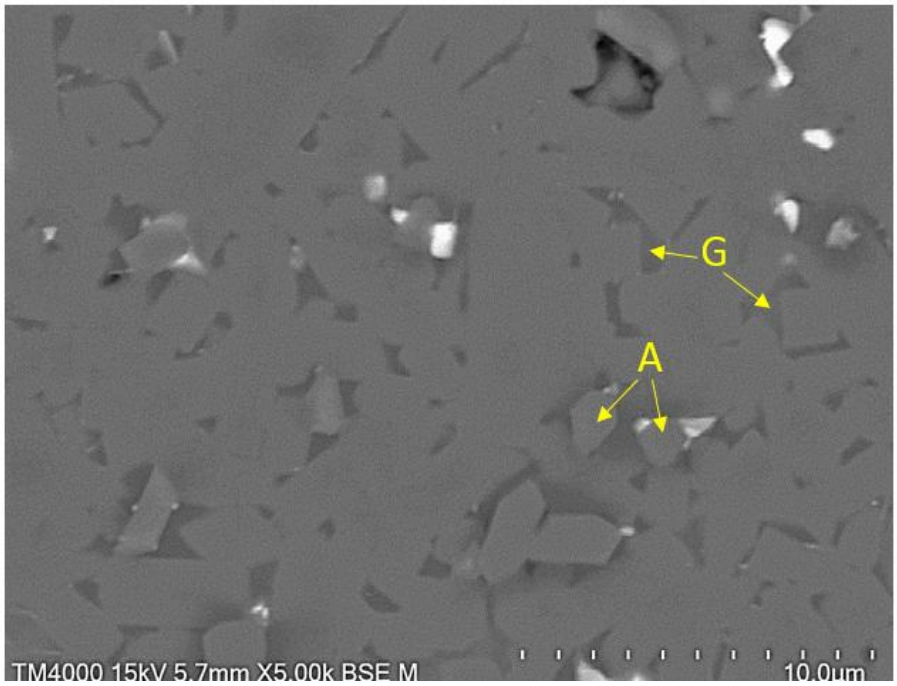

Figure 3.10. Backscattered SEM image of the sample prepared with TEMED and AM/MBAM ratio of 15

Starting mullite powder had oxides such as 0.3% Fe_2O_3, 0.2% TiO_2, 0.05% CaO, 0.1% MgO, 0.2% Na_2O and 0.6% K_2O at various concentrations in addition to Al_2O_3 and SiO_2 (see Table 2.1). Schneider et al. [60] reviewed the structure and properties of mullite ceramics and explained various cation incorporations into crystal structure in detail. Mullite incorporated Ti^{3+}, Ti^{4+}, Fe^{2+}, and Fe^{3+} at different amounts, depending on the synthesis conditions. The maximum solubility limit was controlled by radii and oxidation states of the transition metal ions; the highest degrees of incorporation were observed for Fe^{3+} and Ti^{4+}. Alkali and alkaline earth cations entered the mullite structure at low quantities. For example, Na^+ and Mg^{2+} incorporations were about 0.4 wt% Na_2O and 0.5 wt% MgO, respectively. Zr^{4+} entered the structure at low amounts of ≤0.8 wt% ZrO_2. In our case, ZrO_2

contamination was evident from the white spots (see Figures 3.10 to 3.12) and EDS analysis, as mentioned above. However, ZrO_2 was not detected in the matrix by EDS, stating that ZrO_2 did not dissolve in mullite matrix; rather, it segregated as separate phase.

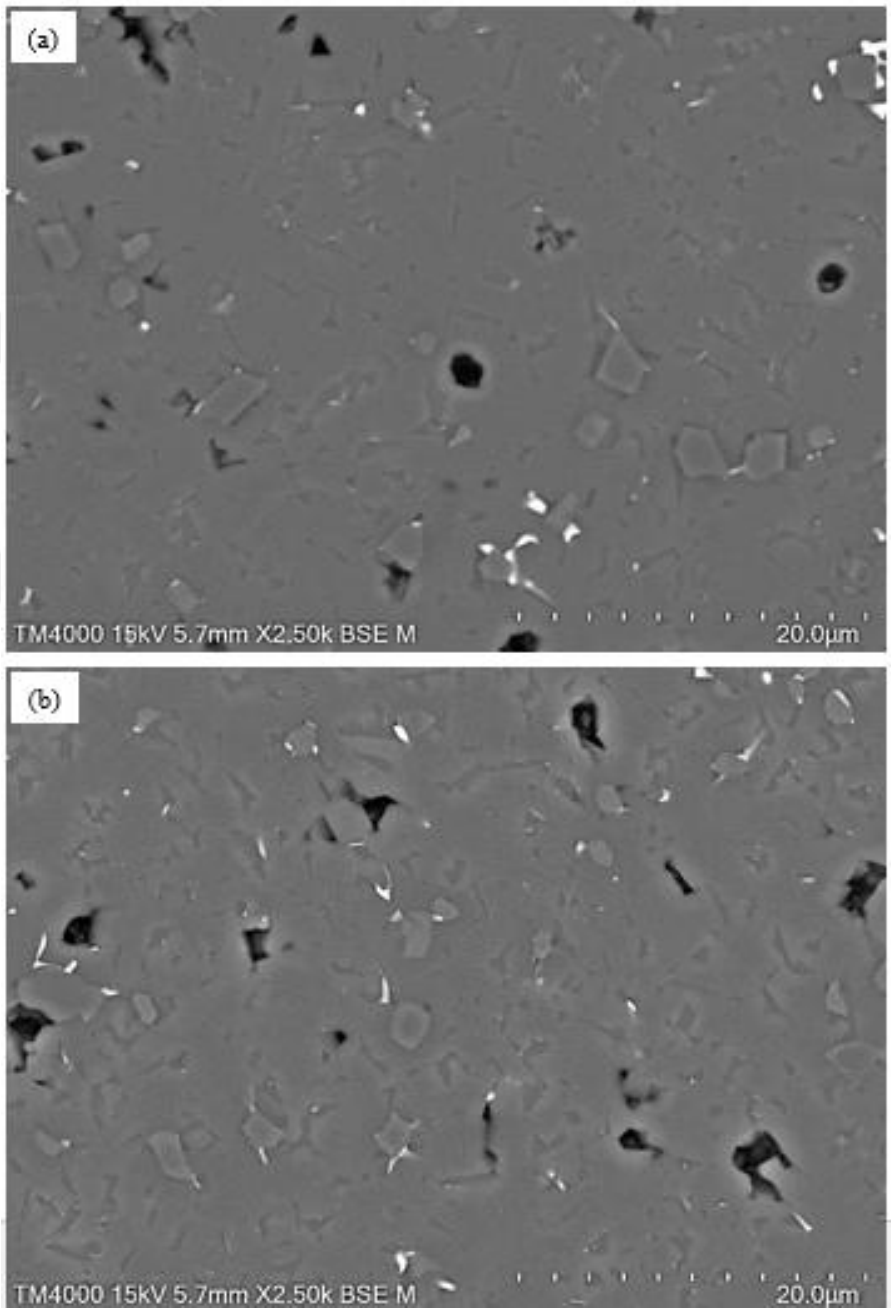

Figure 3.11. Back-scattered SEM images of the samples prepared without TEMED at AM/MBAM ratios of (a) 9, (b) 12, (c) 15, and (d) 20

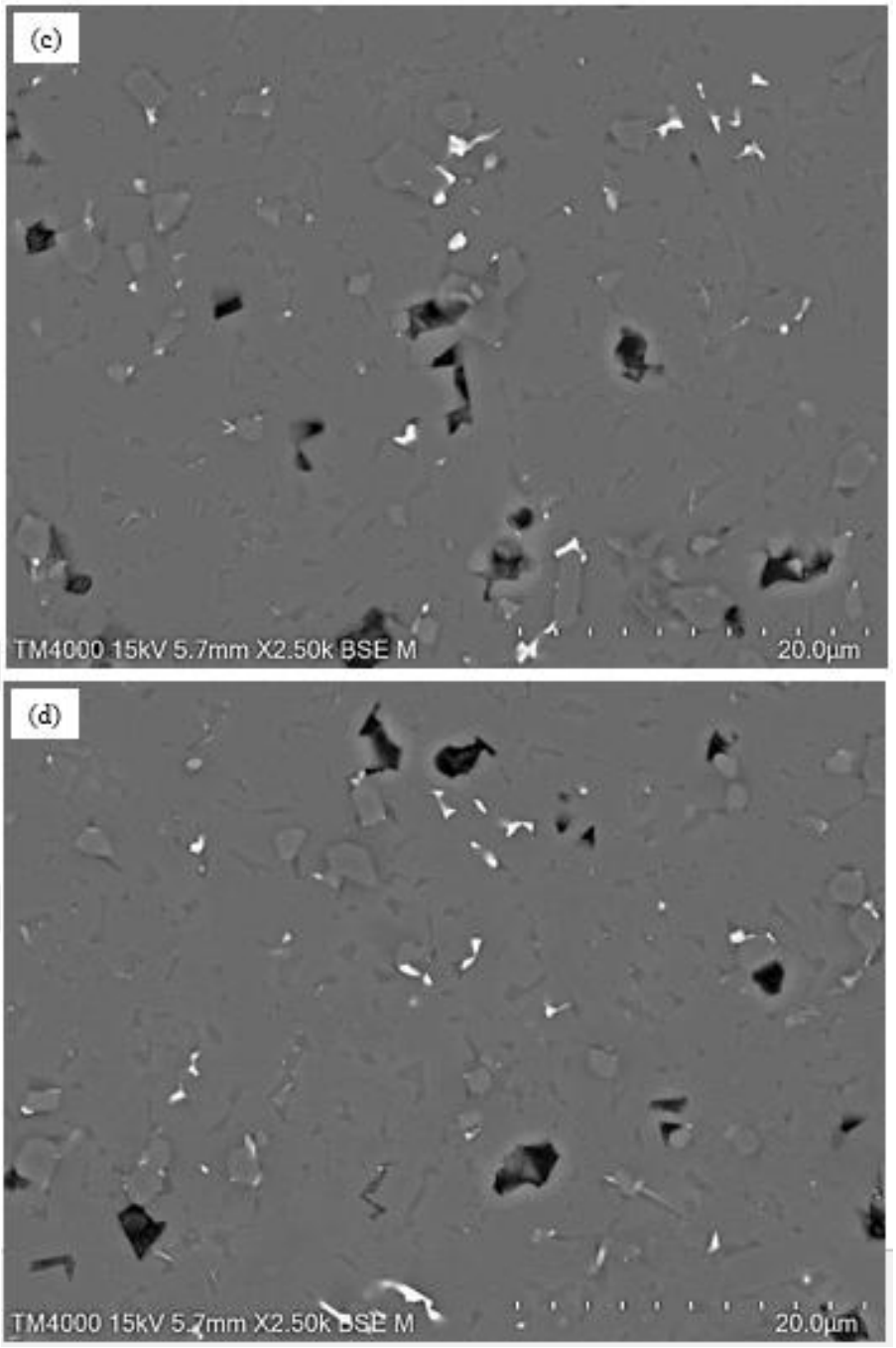

Figure 3.11 (continued). Back-scattered SEM images of the samples prepared without TEMED at AM/MBAM ratios of (a) 9, (b) 12, (c) 15, and (d) 20

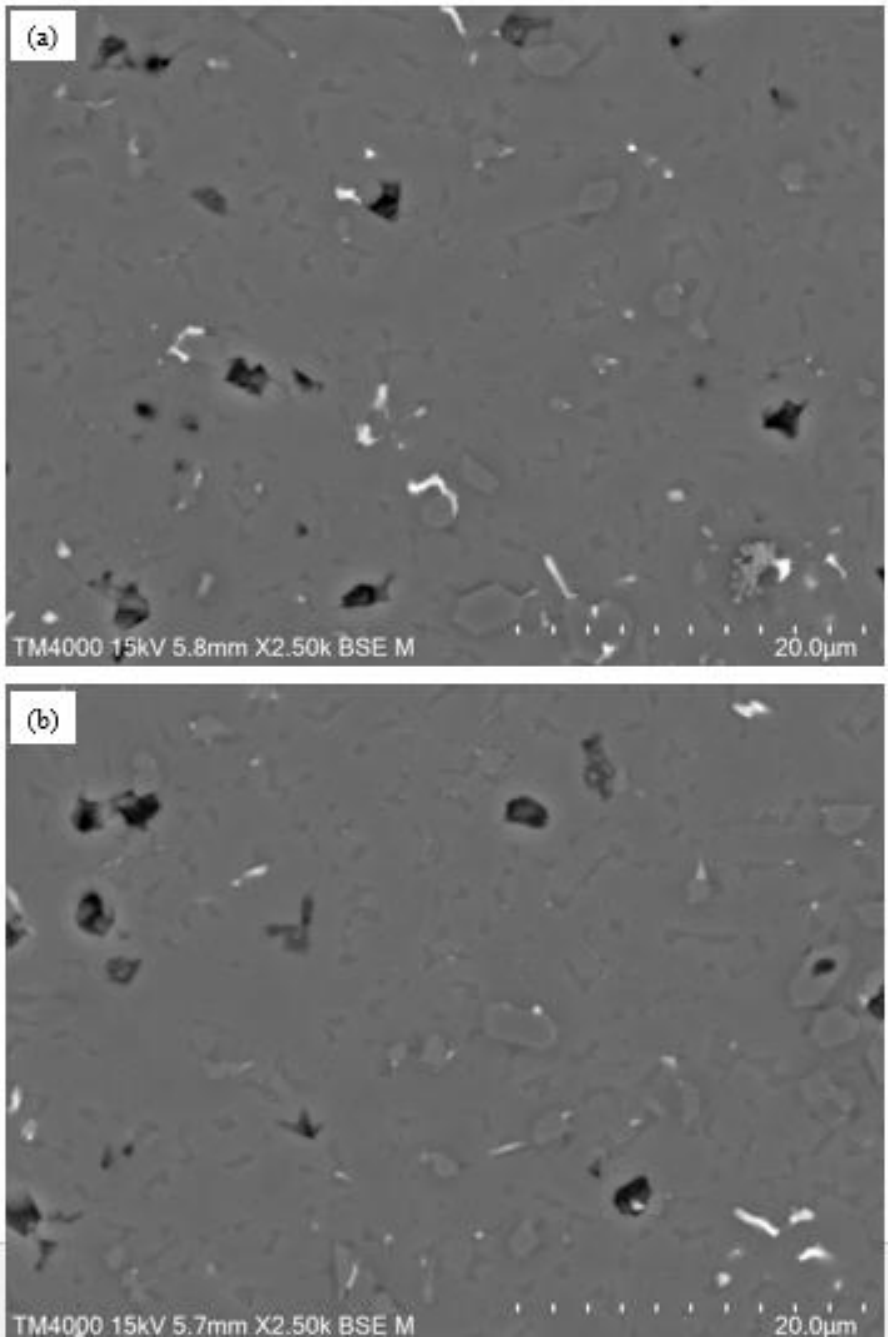

Figure 3.12. Back-scattered SEM images of the samples prepared with TEMED at AM/MBAM ratios of (a) 6, (b) 9, (c) 12, and (d) 15

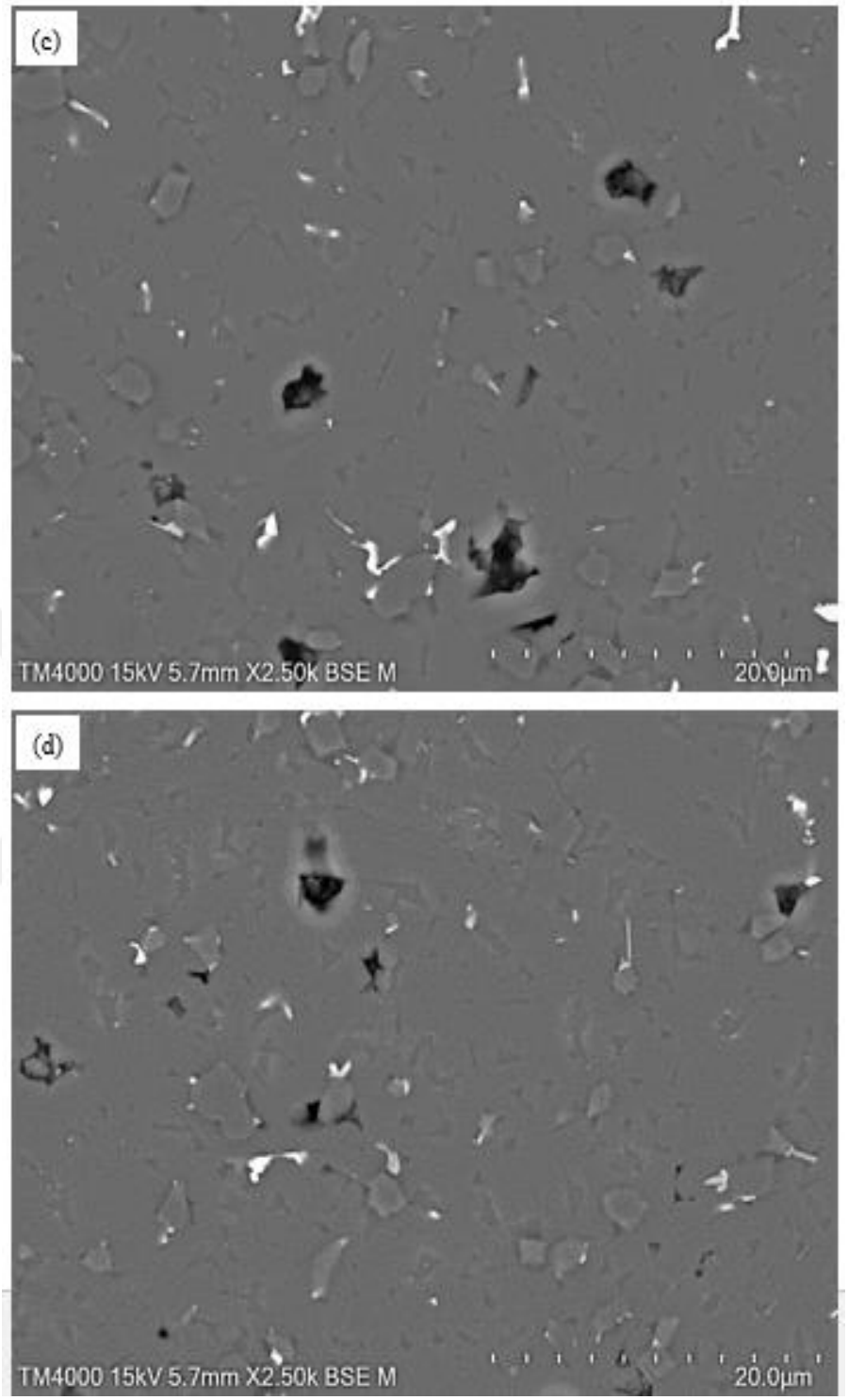

Figure 3.12 (continued). Back-scattered SEM images of the samples prepared with TEMED at AM/MBAM ratios of (a) 6, (b) 9, (c) 12, and (d) 15

3.2 Mechanical Properties

Figure 3.13 compares hardness results of the samples with/out TEMED at various AM/MBAM ratios, using Equation 2.4. Average values ranged from 1077 HV to 1089 HV for all samples. The theoretical hardness value of mullite is 1070-1120 HV [57, 58]. Figure 3.14 shows hardness indentation pictures of the samples prepared with/out TEMED at AM/MBAM ratio of 15. Similar to the densification results, AM/MBAM ratios and TEMED didn't significantly change the hardness of the samples.

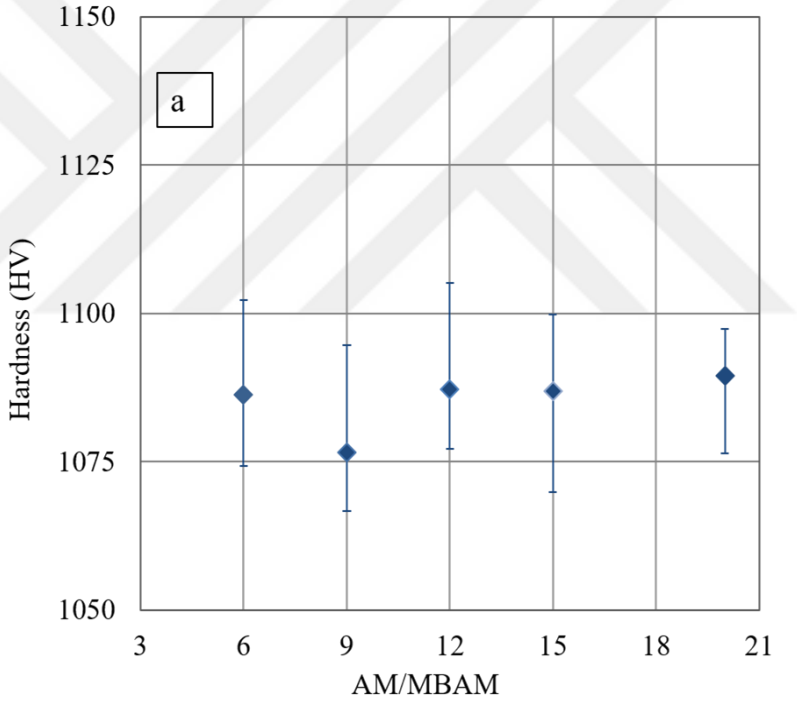

Figure 3.13. The hardness of the samples without TEMED (a) and with TEMED (b) at different AM/MBAM ratios

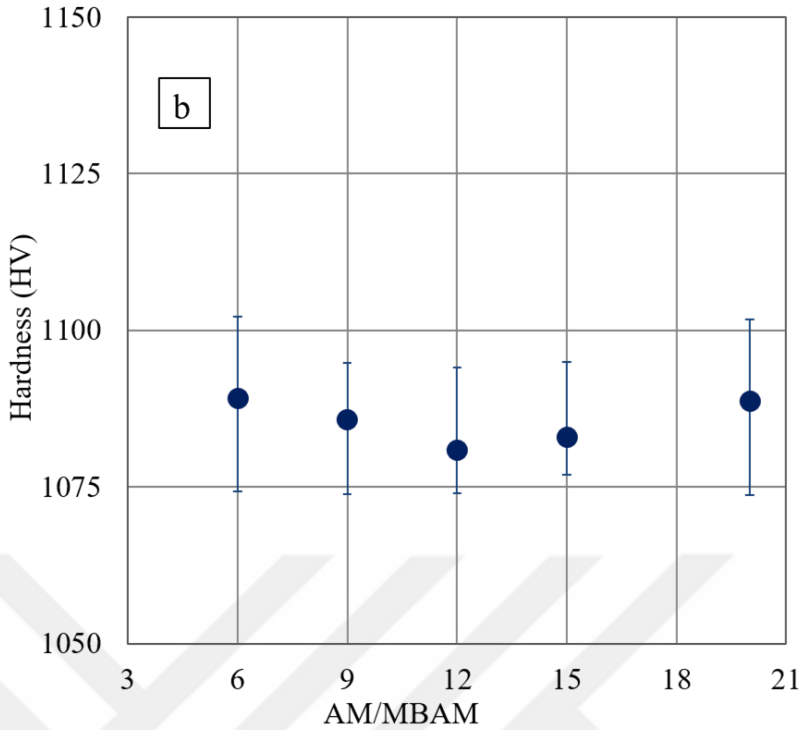

Figure 3.13 (continued). The hardness of the samples without TEMED (a) and with TEMED (b) at different AM/MBAM ratios

Figure 3.15 shows the fracture toughness of the samples prepared with/out TEMED at various AM/MBAM ratios, using Equation 2.5. These values were ranged from 2.4 to 2.5 MPa.$\sqrt{m}$. Figure 3.16 shows a fracture toughness picture of the sample prepared with TEMED at AM/MBAM ratio of 15. Reported fracture toughness of mullite ranged between 2.25 and 2.55 MPa.$\sqrt{m}$ [94]. The AM/MBAM ratios and TEMED didn't change the fracture toughness significantly, and results close to the literature values were obtained.

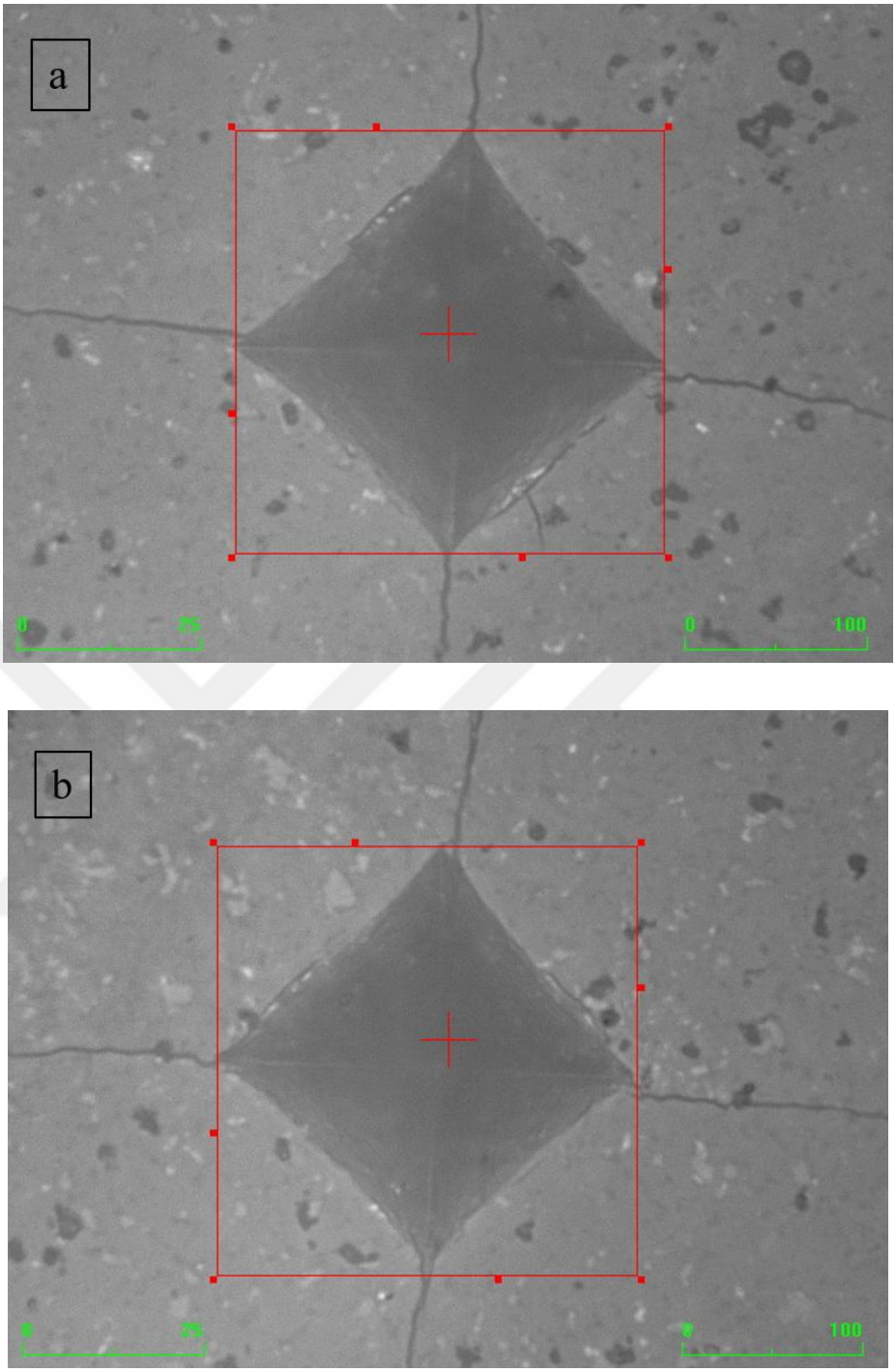

Figure 3.14. The hardness indentation pictures of the samples with TEMED (a) and without TEMED (b) at AM/MBAM ratio of 15

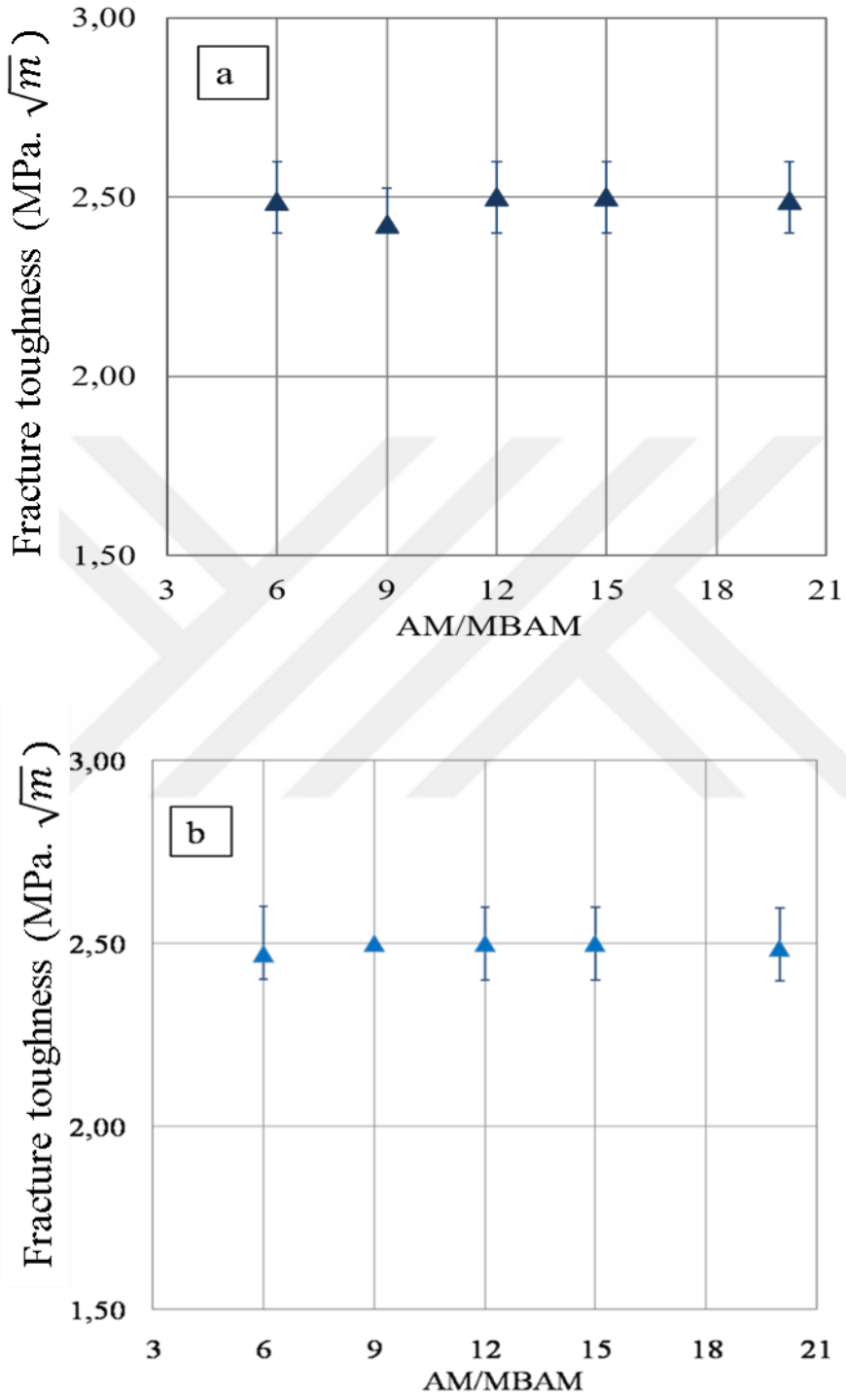

Figure 3.15. The fracture toughness of the samples without TEMED (a) and with TEMED (b) at different AM/MBAM ratios

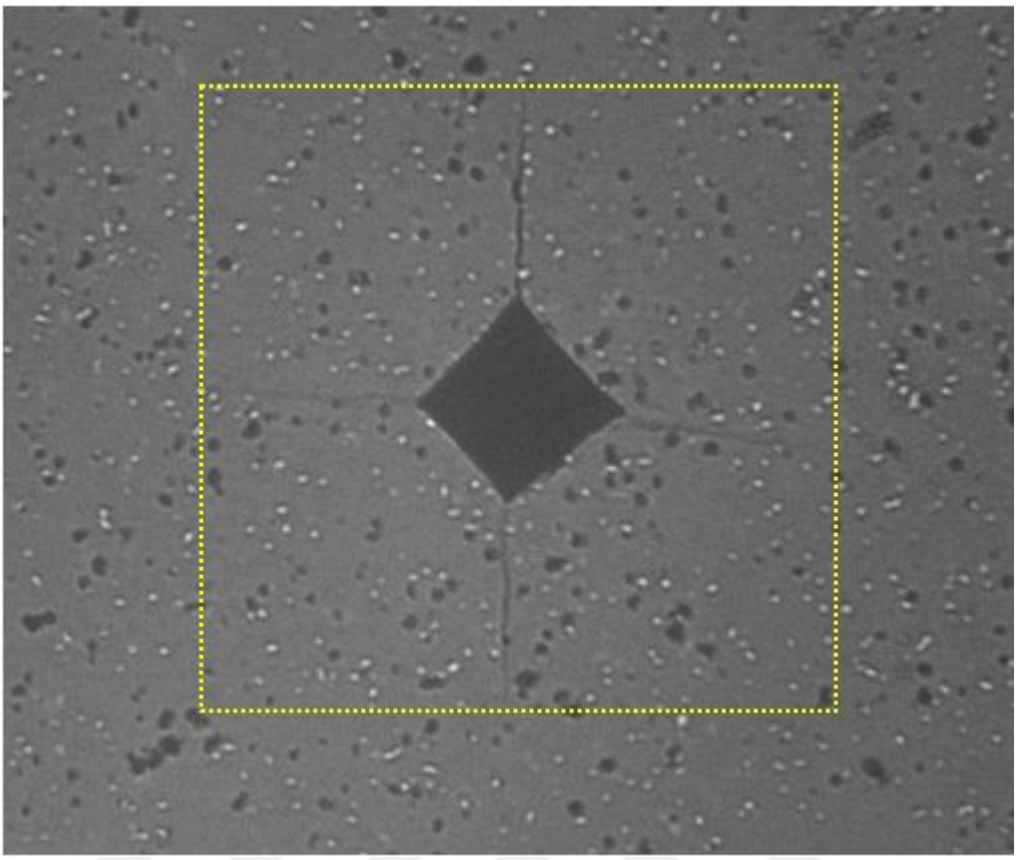

Figure 3.16. The fracture toughness result samples with TEMED at AM/MBAM ratio of 15

Figure 3.17 shows an SEM picture taken from the fracture surface of mullite prepared using TEMED at AM/MBAM ratio of 20. It reveals that fracture path consists of both intergranular (relatively rough regions) and intragranular (relatively flat regions) fractures. Figure 3.18 shows crack propagation pathways in the samples prepared with TEMED at AM/MBAM ratios of 15. Grain shape and its angle to propagating crack is very critical to determine crack deflection and crack bridging mechanisms. Grains 1 and 2 were equiaxed in shape and crack was deflected around them. However, Grain 3 was acicular in shape and located perpendicular to crack. Therefore, crack proceeded thru the grain but faceted rectangular pore successfully bridged the crack. Effect of elongated grains was more clearly seen for Grains 4, 5 and 6. Grain 4 was located with a deviation angle of about 45°, Grain 5 was perpendicular and Grain 6 was parallel to the propagating crack. Crack was successfully deflected when the elongated grains were either parallel or located at a deviation angle. However, when the elongated grains were perpendicular, they were

ineffective in bridging/deflecting the advancing cracks. Instead, crack proceeded directly thru them. Therefore, intragranular and intergranular fractures were observed in the mullite ceramics (see Figure 3.17) because mullite has a tendency to anisotropic grain growth [84,88]. When the ceramic is not textured, the grain growth is random in 3D, resulting in smaller and thicker acicular grains at various deviation angles to the propagating crack. Paek et al. [95] investigated crack propagation in random and textured Al_2O_3 ceramics having a weak interface of monazite phase. They reported that random samples had a deviation angle to propagating crack as opposed to nearly parallel and perpendicular in the textured samples. They further stated that intergranular fracture mode was improved by texturing.

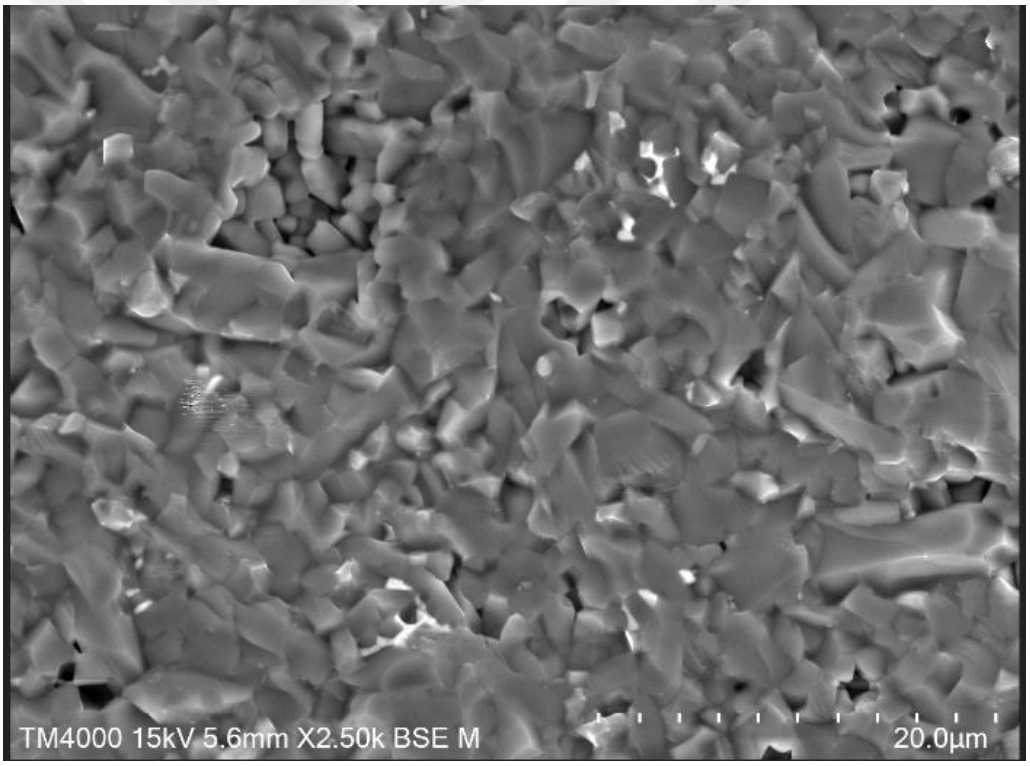

Figure 3.17. Back scattered SEM pictures of fracture surface mullite sample with TEMED at AM/MBAM ratios of 20

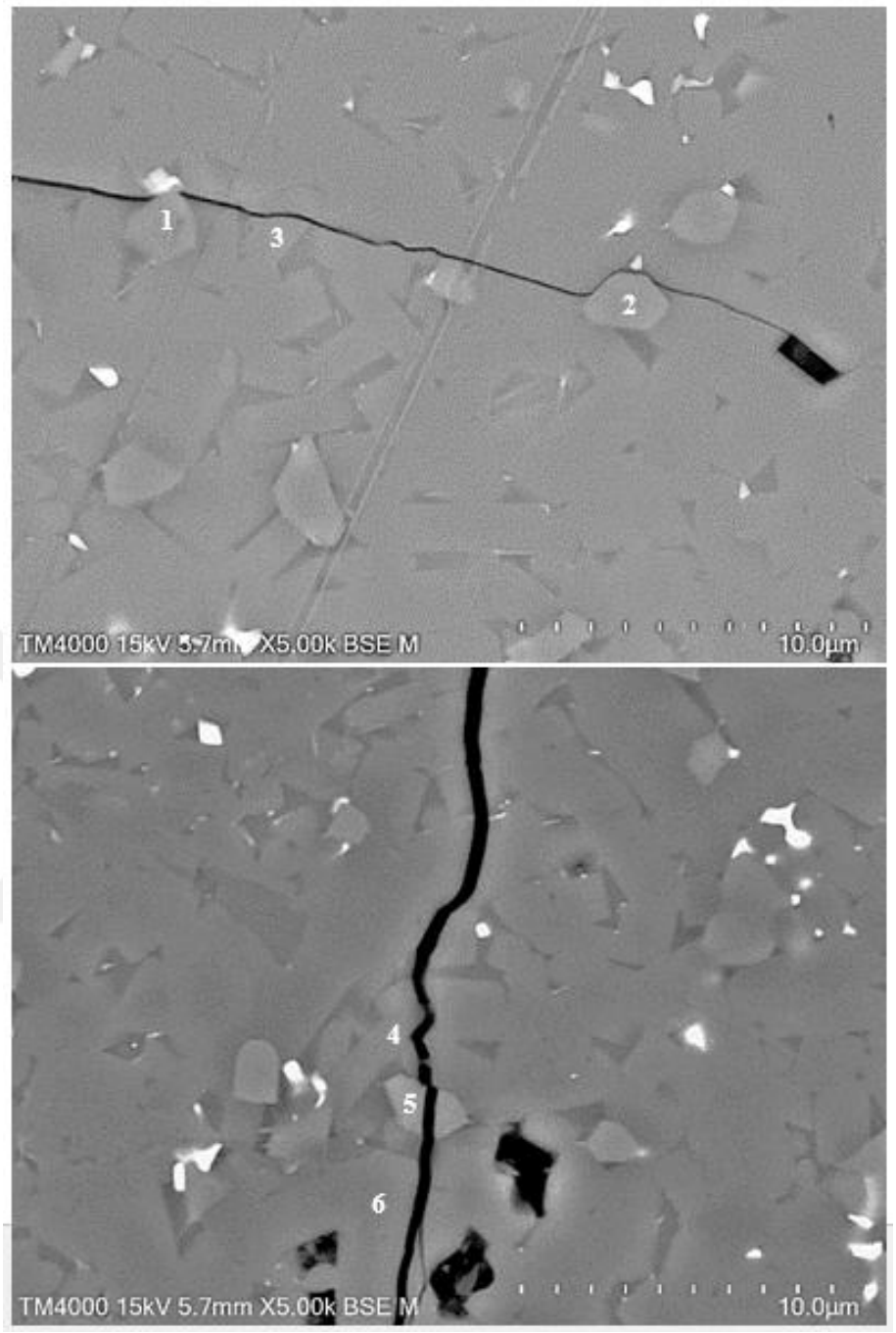

Figure 3.18. The crack propagation in the samples prepared with TEMED at AM/MBAM ratios of 15

Figure 3.19 shows the variation of flexural strength of the samples prepared with/out TEMED at various AM/MBAM ratios, as determined from 3-point bending tests using Equation 2.6. The averaged flexural strength values ranged from 172 MPa to 182 MPa for the samples with TEMED (Figure 3.19a), and from 130 MPa to 210 MPa for the samples without TEMED (Figure 3.19b). In the latter case, flexural

strength first increased up to 210 MPa at AM/MBAM ratio of 15 and then suddenly decreased to 130 MPa at AM/MBAM ratio of 20. These results indicate that the presence of TEMED significantly affected the flexural strength of samples, as opposed to the trends observed for the densification, hardness and fracture toughness results.

The surface quality and geometry of the samples with TEMED were better than that of without TEMED. In addition, removal of the samples from the mold was very easy with minimal applied mechanical stress due to fast curing in the presence of TEMED. Figure 3.20 shows dried samples prepared with/out TEMED at AM/MBAM ratio of 20. As a result of a severe distortion in the geometry of the sample prepared without TEMED (Figure 3.20a), the sample had the lowest flexural strength of 130 MPa even though a test bar was prepared by grinding and polishing. The samples prepared with TEMED had uniform shapes all the time (Figure 3.20b), and hence they had flexural strength values very close to each other. Unfortunately, the flexural strength of sample without TEMED at AM/MBAM ratio of 6 was not able to be measured due to severe warping and cracking after sintering. In addition, this sample had the longest curing time of 65 minutes (see Figure 3.6) and it was very difficult to demold. In contrast to the flexural strength, the AM/MBAM ratios and TEMED do not significantly change toughness and hardness values because of the indentation method in a micron-sized area as compared to all volume consideration by the 3-point bending test to determine flexural strength. In addition, sample condition (e.g., sharp edges, micro cracks on the surface and residual stress) is very critical for the 3-point bending test. Therefore, there observed a common problem of longer drying times (between 35 to 65 minutes) and shape distortions in the samples prepared without TEMED, which negatively affected the flexural strength. Particularly, weak points due to stress gradients induced during demolding and drying stages were responsible for large strength variations due to start of curing at the bottom of the mold and progression upward. The curing time was much lower by using TEMED, which allowed fast demolding and uniform drying from all surfaces and yielded uniform samples. Therefore, very close averaged flexural strength values were measured.

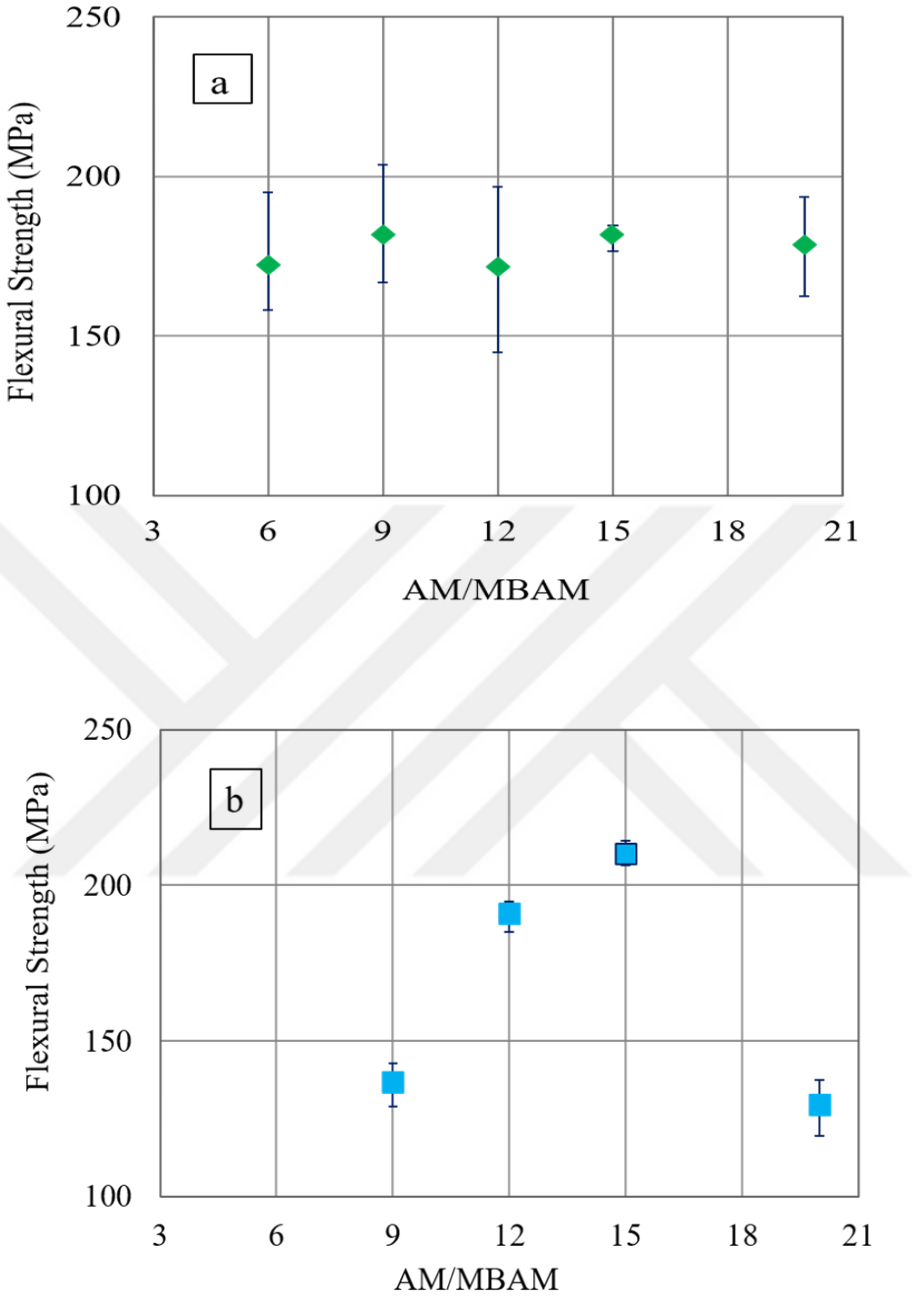

Figure 3.19. The flexural strength of samples with TEMED (a) and without TEMED (b) at different AM/MBAM ratios

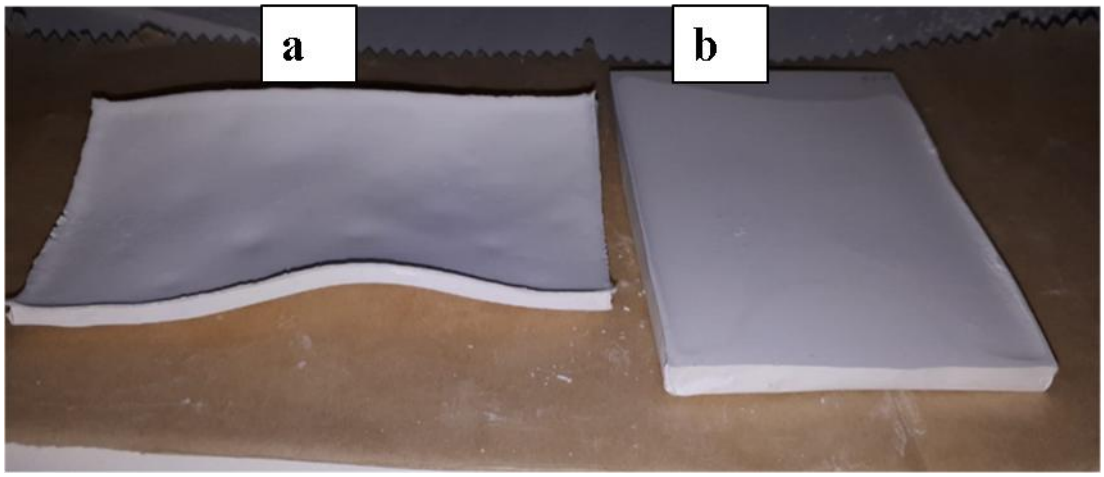

Figure 3.20. Dried samples prepared at AM/MBAM ratio of 20 without (a) and with (b) TEMED

Fracture strength and Weibull modulus are generally used to determine reliability of the ceramics for structural applications. The surface finishing quality, microstructure and amount of inclusions affect Weibull modulus [96]. Figure 3.21 shows statistical Weibull analysis of the flexural strength. The Weibull modulus (m) was determined from a linear fit to the data points with an R^2=0.983 and found to be 12.33 for the samples prepared with TEMED. Weibull modulus generally ranges between 3 and 15 for ceramics [96] and a high value above 10 can be defined as tough ceramic components [71]. In other words, a higher m means lower spreading of fracture strength and more reliable material [96]. Hence, the ceramics prepared using TEMED exhibited tough behavior. Constant variable (c) in the linear equation was 64.44. The characteristic strength was found to be 186 MPa, using Equation 2.9, below which no failure is expected. The m and c were also found as 4.98 and 25.85, respectively, with an R^2=0.89 for the samples prepared without TEMED. A lower m indicates higher spreading of fracture strength and less reliable material, as evidenced from Figures 3.19b and 3.20a. Yan et al. [97] prepared Al_2O_3 samples by dry pressing at various pressures and cold isostatic pressing in order to modify particle packing homogeneity in the green samples. They obtained Weibull modulus between nearly 4 and 14 after sintering. They attributed this variation to the processing variables such as green density, packing homogeneity, uniform grain size and homogeneous microstructure. Even though gel casting is a colloidal method

providing a high degree of homogeneity, processing variables, particularly TEMED in our study, significantly alter Weibull modulus or reliability of the ceramics.

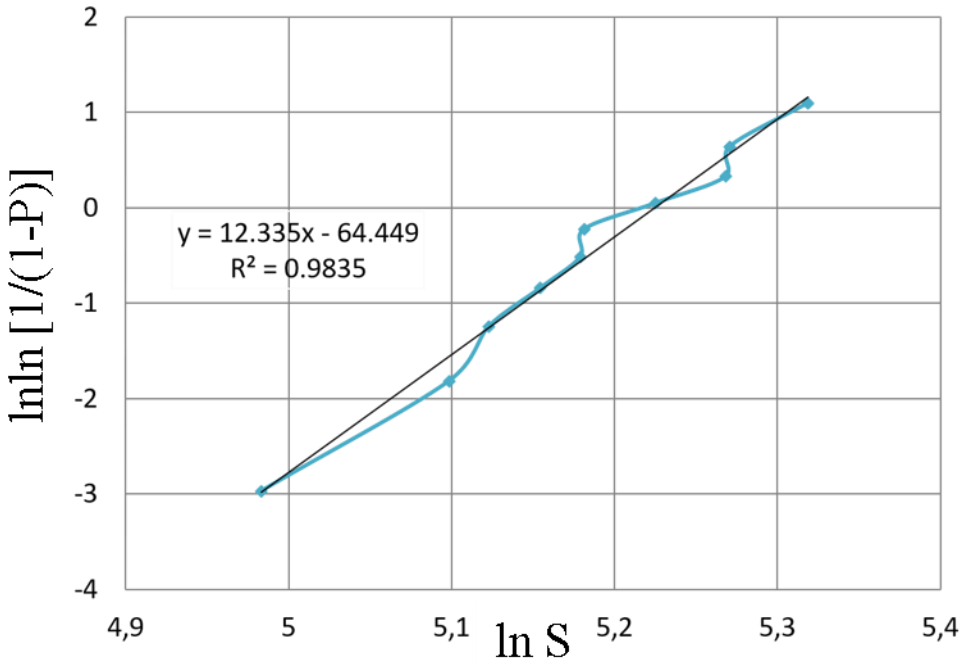

Figure 3.21. Statistical analysis of flexural strength using Weibull approach

Figure 3.22 shows variation of Young's modulus as a function of relative density. Elastic modulus was calculated by measuring natural resonance frequency, using Equation 2.7. Young's modulus decreased from 185 MPa at 96.2 % relative density to 161 GPa at 91.4 % relative density due to the effect of porosity. Young's modulus of dense mullite was between 143 GPa and 230 GPa [57]. The presence of defects such as pores leads to lower mechanical properties of materials. The influence of pores on Young's modulus (E) was proposed by L. Fuglsang [98] and given as;

$$E = \frac{E_o(1 - P_e)}{1 + aP_e} \qquad \textbf{(3.1)}$$

where P_e is volume fraction of porosity, E_o is elastic modulus of pore-free material and a is pore shape (a=1 for spherical pores). As porosity increases, Young's modulus decreases.

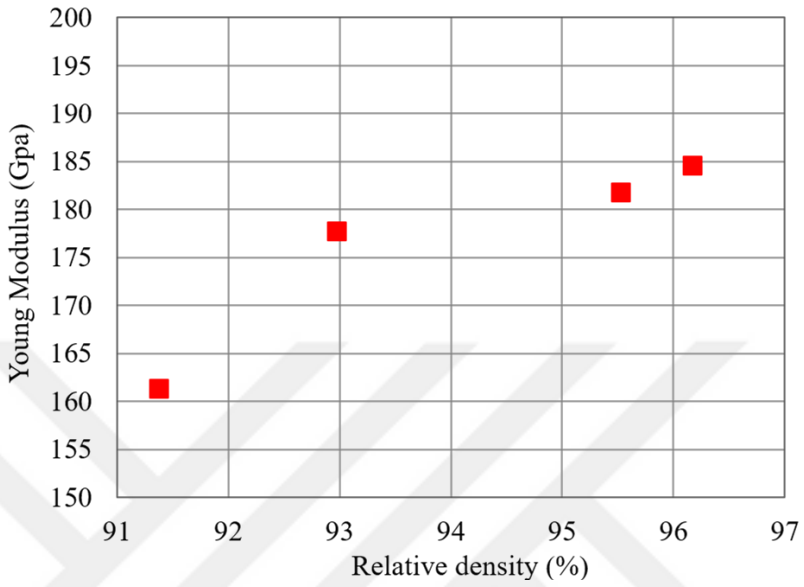

Figure 3.22. Young's modulus at different densification levels

3.3 Thermal properties

Figure 3.23 shows thermal diffusivity, specific heat capacity and thermal conductivity of mullite prepared with TEMED at AM/MBAM ratio of 20. The thermal conductivity was calculated from the thermal diffusivity, specific heat and density measurements, using Equation 2.10. Thermal conductivity was found to increase with temperature and vary between nearly 1.5 and 3.75 W/m.K in the temperature range between 50°C and 550°C. Thermal conductivity for mullite has been reported to be 1.5-2 W/m.K between 25°C and 100°C [99], which is consistent with our results. Thermal conductivity in materials depends on carrier types such as free electrons and phonons. In contrast to lower thermal conductivity of ceramics (e.g., generally between 2 and 50 W/m.K at room temperature) [100], metals have higher thermal conductivity varying between 20 and 400 W/m.K [100], because of the free electrons carrying heat. The contribution of electrons in heat transport is much more effective than that of phonons, because scattering of the former is more

difficult. In nonmetallic materials such as ceramics, phonons are major contributor in heat conduction but their contribution can be limited due to scattering by lattice imperfections and lattice vibrations [100]. That is why the thermal conductivity of ceramics are lower than metals.

In crystalline ceramics, the scattering of phonons from mainly lattice vibrations increases with increasing temperature, which results in lower thermal conductivities. The thermal conductivity of mullite as a function of temperature was investigated by Schneider et al. [60]. They reported that the thermal conductivity of fully crystalline mullite decreased from 6 W/m.K at 20°C to 3 W/m.K at 1400°C. However, Figure 3.23c shows in our samples that thermal conductivity increases with temperature, which is opposite to fully crystalline mullite conductivity. This result is in fact expected because mullite used in this study contained 5-10 % glassy phase (see Table 2.1). In contrast to the crystalline ceramics, thermal conductivity of glasses and other amorphous materials such as glass ceramics increases with increasing temperature because conduction is by means of atomic or molecular migration [101], which positively contributes to the conduction mechanism with increasing temperature, as was the case shown in Figure 3.23c. Glassy regions were clearly seen in Figure 3.10 and the presence of glass phase was observed as a background in the XRD pattern (see Figures (3.1 and 3.9). Stoichiometric mullite ($3Al_2O_3.2SiO_2$) has 72% Al_2O_3 and 28% SiO_2 but our mullite composition had 72% Al_2O_3 and 26% SiO_2 together with other oxides (see Table 2.1). Therefore, glass composition was expected to be rich in Al_2O_3 and SiO_2 together with other minor oxides. Thermal conductivity of soda lime glasses increased from 0.8 W/m.K at -100°C to 1 W/m.K at 0°C and to 1.15 W/m.K at 100°C [102]. Therefore, thermal conductivity in mullite containing glassy phase was determined by a combined effect such that phonon scattering in the crystalline phase decreased and atomic or molecular migration [101] in the amorphous phase increased the conductivity. The overall effect in Figure 3.23c was that conductivity increased with temperature, stating that amorphous phase embracing the crystalline grains (as seen in Figure (3.10)) dominated the conductivity.

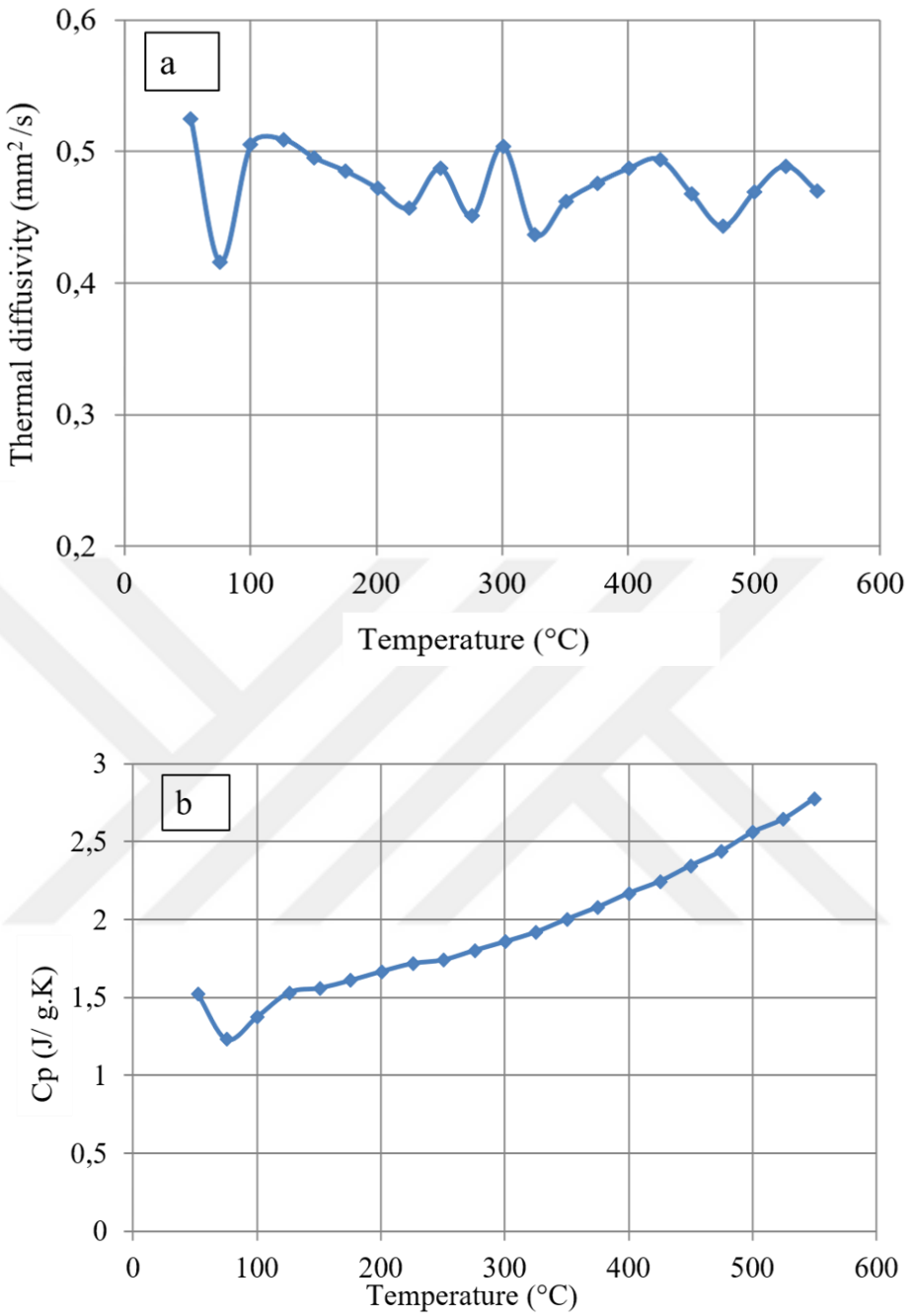

Figure 3.23. Thermal properties of the sample with TEMED at AM/MBAM ratio of 20 (a) thermal diffusivity, (b) C_P and (c) thermal conductivity as a function of temperature

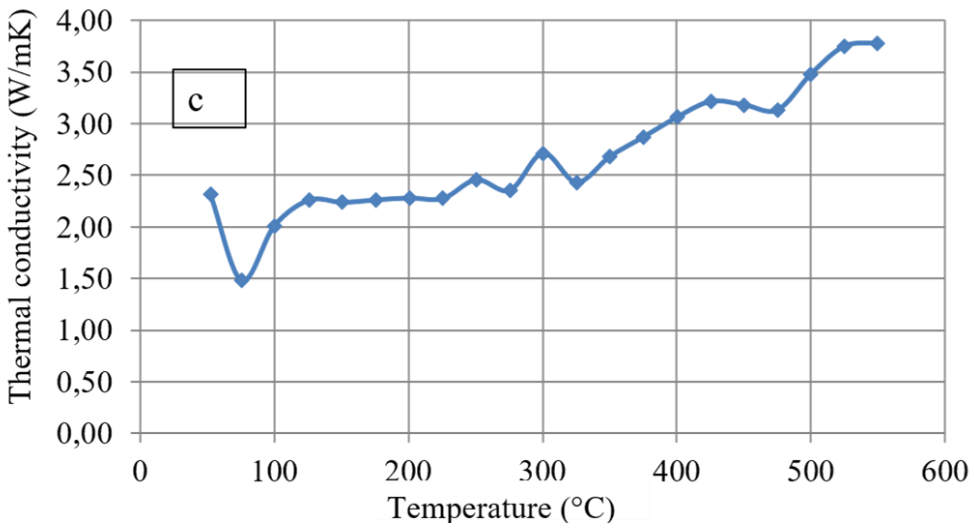

Figure 3.23 (continued). Thermal properties of the sample with TEMED at AM/MBAM ratio of 20 (a) thermal diffusivity, (b) C_P and (c) thermal conductivity as a function of temperature

Thermal expansion coefficient (CTE) of the sample prepared at AM/MBAM ratio of 20 is given in Figure 3.24. A non-linear thermal expansion was observed below 300°C which indicates that temperature exposure time was not long enough to initiate expansion in the sample due to low thermal conductivity [103]. To determine CTE, a linear fit to the relative expansion vs. temperature data was drawn between 30°C and 800°C with an R^2=0.995, as shown in Figure 3.25, and the slope gave a CTE of 5.26 ppm/°C. The CTE of mullite was 5.3 ppm/°C between 25°C and 1000°C [59]. There seems to be a slight slope change at around 500°C. Therefore, two linear fits were separately applied between 30-500°C and 500-800°C. The CTE between 30°C and 500°C was 4.7 ppm/°C with an R^2=0.997, and the CTE between 500°C and 800°C was 6.0 ppm/°C and R^2=0.999. In fact, this slight slope change can be ignored based on the R^2 values being very close to 1, but it may be attributed to a glass transition temperature (T_g) because of the presence of a glass phase (see Table 2.1, Figure 3.1 and Figure 3.9). Further investigation is required to understand the effect of glassy phase on T_g.

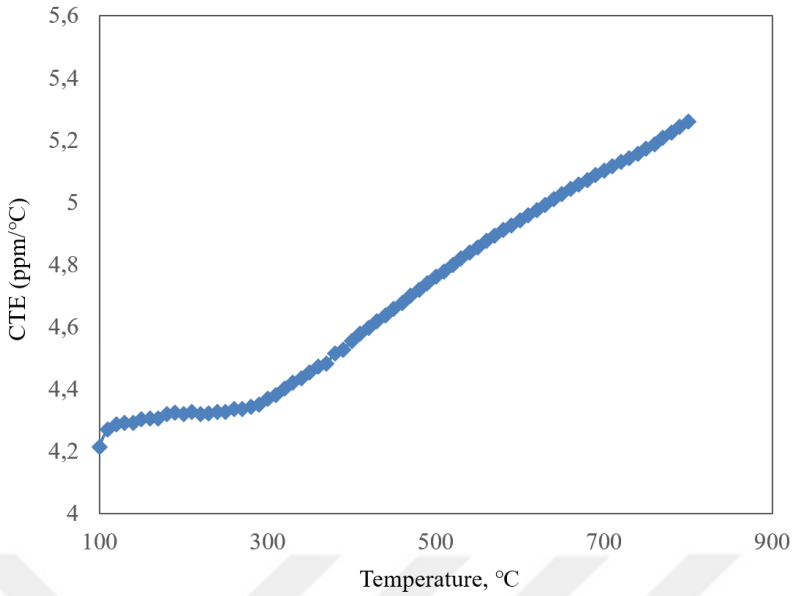

Figure 3.24. Thermal expansion coefficient as a function of temperature

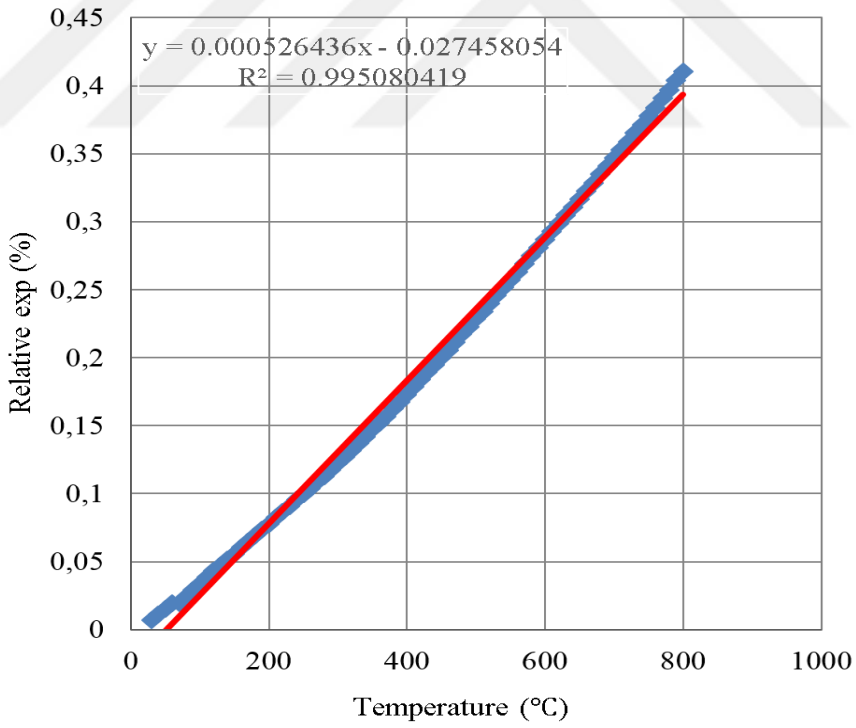

Figure 3.25. Relative expansion as a function of temperature

Thermal shock effect on fracture toughness and crack propagation of the samples with TEMED at AM/MBAM ratio of 20 was investigated by indentation-quench method [74]. First, pre-cracking was formed with a Vicker hardness indenter. Second, the samples were quenched into water from different temperatures. Then, the crack propagation was measured. Hardness and fracture toughness were calculated using Equations 2.4 and 2.5. Note that Young's modulus measured at room temperature was used for all quenching temperatures. The change in fracture toughness and crack extension as a function of quenching temperature is shown in Figure 3.26. Note that fracture toughness was 2.5±0.01 MPa.$\sqrt{m}$, crack length was 173.5 μm, and hardness HV was 1086 at 25°C. Fracture toughness almost remained constant up to 200°C and then steadily decreased without any sharp drop to totally zero level. In other words, crack size increased due to temperature induced crack propagation with increasing quenching temperature. Hence, correspondingly, fracture toughness decreased with increasing crack size. The same method was also applied to correlate quenching-induced mechanical properties in other ceramics. Flexural strength as measured by a 3-point bending method indicated that it sharply dropped to almost zero at ~160°C due to extensive crack propagation in soda-lime-silica glass [104] and to a lower value at ~300°C due to crack propagation and arresting in dense polycrystalline Al_2O_3 [105].

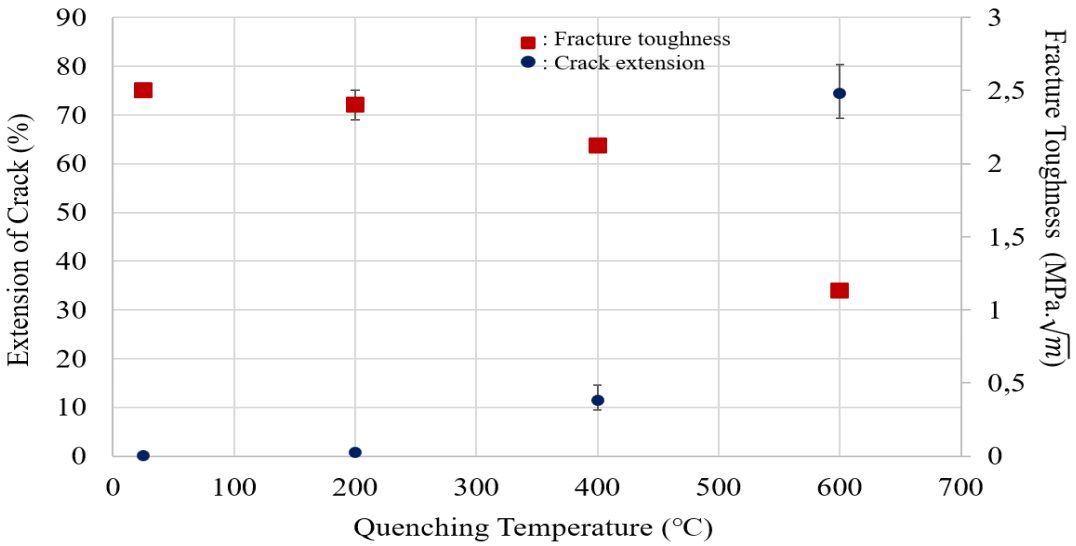

Figure 3.26. Change in fracture toughness and crack extension as a function of temperature

The average hardness, fracture toughness, and crack extension are summarized in Table 3.2. Decrement in fracture toughness was 4 % after 200°C. The biggest change in fracture toughness and average crack extension were observed at 600°C as 55 % and 74.3 %, respectively. Critical temperature difference of quenching was reported to be from a temperature where a 10 % crack extension was observed [74]. Hence, critical quenching temperature was about 400°C which yielded 11.5 % crack extension in our studies. The micrographs of the crack extensions as a function of temperature are shown in Figure 3.27. Above 600°C, the extension of crack could not be clearly determined due to its longer crack path.

Table 3.2. The results of average fracture toughness and crack extension after quenching (+ denotes increment and – denotes decrement with respect to the 25°C values)

Quenching Temperature (°C)	Average Hardness (HV)	Average fracture toughness change (%)	Average crack extension (%)
200	1088	- 4	+ 0.6
400	1072	- 15	+ 11.5
600	1036	- 55	+ 74.3

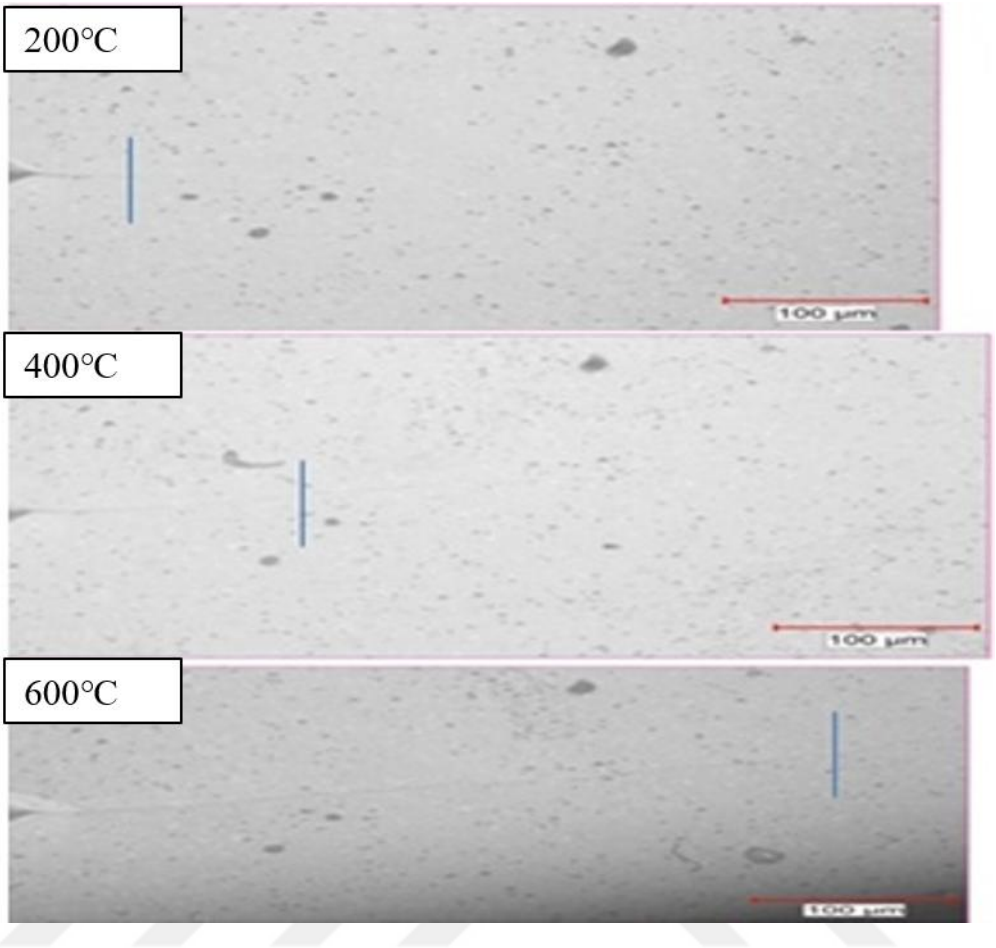

Figure 3.27. Extension of crack at 200°C, 400°C and 600°C.

Thermal shock behavior is influenced by some thermo-mechanical parameters such as Young's modulus, flexural strength, fracture toughness, thermal expansion coefficient, thermal conductivity, and heat transfer rate (i.e. surface conductance). There are commonly used five thermal shock parameters (R, R′, R″, R‴, and R⁗) to define thermal shock resistance (TSR) [106]. R, R′, and R" are related to the ease of nucleation of fracture flaws in a material, and R‴ and R⁗ are related to the resistance to the crack propagation. The R parameter (see Equation 1.6) typically reveals the worst case condition where heating or cooling occurs under conditions of infinite heat transfer [107]. The R parameter of the sample with TEMED at AM/MBAM ratio of 20 was calculated from Equation 1.6 using the values given in Table 3.3. The result reveals that mullite can withstand a temperature difference (ΔT) of 142.4°C. The same value was reported as 101°C [108] and 80 [23] for Al_2O_3, which indicates that mullite has a better TSR than Al_2O_3. In addition, R=114°C was

calculated for mullite using the literature values [23]. The TSR values calculated (e.g., the R) and measured (e.g., indentation-quenching) are different from each other but both of them are used to make some sound comparisons between different materials.

Table 3.3. Thermal shock resistance (TSR) of the sample with TEMED at AM/MBAM ratio of 20.

Parameters used in Eqn. 1.6	Values
Flexural strength, MPa	179
Young's modulus, GPa	184
Poisson's ratio [109]	0.25
CTE, ppm/°C	5.26
TSR (R), °C	142.4

3.4 Dielectric properties

Dielectric constant of mullite was measured at 1 GHz and 10 GHz by using a network analyzer. The dielectric constants were found to be 7.6 and 7.4 at 1 GHz and 10 GHz, respectively. Also, dielectric constant was calculated to be 7.4 at 5 MHz, using Equation 2.11. The loss tangent was measured to be 0.0031 at 5 MHz. In literature, dielectric constant of mullite has been reported between 6.5 and 8.1 up to 14 GHz [36]. Lower dielectric constant is desired for wide frequency band application in radomes [23]. Also, transmission speed of signal increases with decreasing dielectric constant (see Equation 1.4). For example, signal transmission delay time of mullite is 17 % less than those of Al_2O_3 due to higher dielectric constant of Al_2O_3 (9.8) [48]. Therefore, low dielectric constant and loss values of mullite ceramics are suitable for radome applications. In order to decrease dielectric constant further for the same ceramic composition, porosity must be introduced due to its low dielectric constant (see Equation 1.5). Therefore, a mullite ceramic with a relative density of 88% was produced and its dielectric constant was measured to be nearly 6.7 at 1-10 GHz. In this case, all mechanical and thermal properties must be considered together for actual applications because porosity affects those properties as well.

3.5 Application

Gel casting is a colloidal process and viable method to manufacture large and complex parts. In order to prepare a large volume sample, mechanical mixing was used due to the limited mixing capacity of the speed mixer (e.g., 50 grams). Because the samples prepared with TEMED had better mechanical and thermal properties than those prepared without TEMED, a slurry containing TEMED and AM/MBAM ratio of 12 was used to prepare a slurry of nearly 6 kg. In addition, TEMED provided uniform geometry and shape at shorter curing times (e.g., 3-5 minutes). Figure 3.28 compares various green sample sizes prepared and Figure 3.29 shows green machined mullite ceramics.

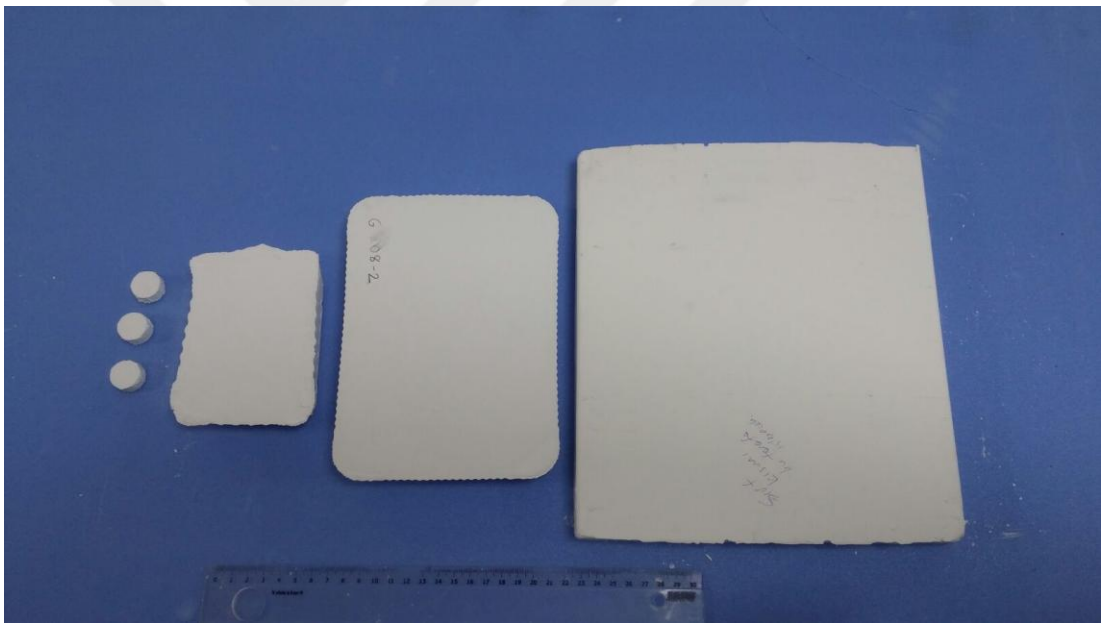

Figure 3.28. Green ceramics at various sizes

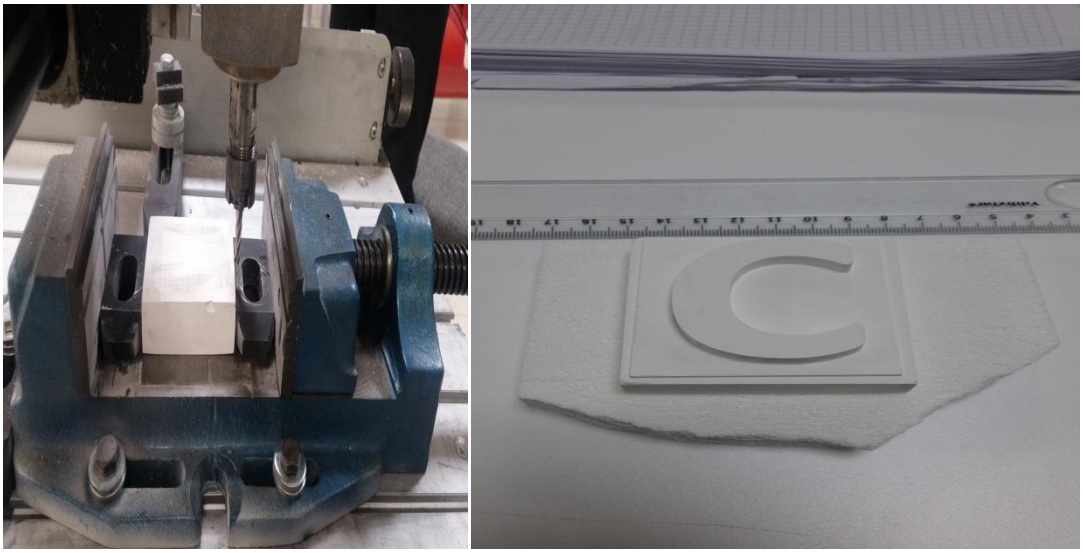

Figure 3.29. Green machining of a mullite block

There are a lot of commercial candidate materials for radome applications such as Al_2O_3, pyroceram, $3Al_2O_3.2SiO_2$ (mullite), BN, BeO, $2MgO.2Al_2O_3.5SiO_2$ (cordierite) and Si_3N_4 [22] . A suitable material for radome application is selected by considering all mechanical, dielectric and thermal properties together. The properties of the samples prepared with/out TEMED in this study are summarized in Table 3.4. Radome performance is limited with higher dielectric constant from band width point of view, so a lower dielectric constant is required. The dielectric constant of dense mullite in this study is nearly 7.5 up to 10 GHz. The dielectric constants of Al_2O_3, AlN, Si_3N_4, BeO and $2MgO.2Al_2O_3.5SiO_2$ are 9.5, 8.9, 8.1, 6.5 and 5.0 up to 14 GHz, respectively [36]. Hence, the dielectric constant of mullite is lower than those of Al_2O_3, AlN and Si_3N_4. Also, dielectric constant affects signal transmission delay time of the radome such that signal transmission delay time of mullite is 17 % less than that of Al_2O_3 as a result of lower dielectric constant of the former [48]. Also, larger change in dielectric constant with temperature can lead to design problems for wide frequency band applications [23]. The dielectric constant change per 100°C for Al_2O_3, pyroceram, $3Al_2O_3.2SiO_2$, BN, BeO is 1.20 %, 0.5%, 0.4 %, 0.6 %, and 1.5 %, respectively, [23] which shows that mullite is among the lowest one. In general, the R parameter (see Equation 1.6) reflects materials suitability from thermo-mechanical parameters point of view, including flexural strength, Poisson's ratio, thermal expansion coefficient and Young's modulus. The calculated R (or ΔT, °C)

values using data given in Table 1.3 for Al_2O_3, BN, Si_3N_4, and BeO are 80°C, 325°C, 321°C, and 71°C, respectively. The R value for the dense mullite in this study was 142.4°C (see Table 3.3). Although Si_3N_4 and BN have much higher R values, higher sintering temperatures under controlled atmosphere are required for Si_3N_4 (e.g., 1825-2080°C) [45] and hot-pressing for BN [47]. In addition, BeO is a toxic material [46]. Therefore, our results prove that mullite is a suitable candidate ceramic for radome applications because it has a higher R value than Al_2O_3 and has advantages in terms of sintering in air as opposed to Si_3N_4 and BN ceramics. In addition, mullite can withstand quenching from nearly 400°C, as determined by the indentation-quenching method.

Table 3.4. The mechanical, thermal and dielectric results of the mullite ceramics sintered at 1540°C for 2 h.

Properties	**TEMED**	**NO TEMED**
Bulk density (g/cm^3)	3.04-3.07	3.04- 3.07
Hardness, HV	1081-1089	1077-1089
Fracture toughness, MPa. $\sqrt{m}$	2.4-2.51	2.4-2.5
Flexural strength, MPa	172-182	130-210
Young Modulus, GPa	161 (91.4 % RD) 185 (96.2 % RD)	-
Dielectric constant	7.4 at 5 MHz ~7.5 at 1-10 GHz	-
Dielectric loss	0.0031 at 5 MHz	-
Thermal shock resistance by indentation-quenching method (ΔT), °C Thermal shock resistance by calculation (the R value) (ΔT), °C	400 142.4	-
Thermal conductivity (50-550°C), W/m.K	1.5-3.75	-
Thermal expansion coefficient (CTE) (30-800°C), ppm/°C	5.26	-

CHAPTER 4

CONCLUSION

Gel casting is a colloidal processing route to produce large and 3-D complex shapes at near net dimensions. The main advantage is the high degree of homogeneity in the slurry due to cross-linking of the monomers, yielding high quality final ceramics with minimum molding defects, high green density and stiffness. Initiator and catalyzer are used to form oxygen free radicals to initiate the cross-linking or polymerization of the monomers and to control curing of the slurry. The most important problem is the drying of green bodies because a fast rate of liquid evaporation can induce stresses, which easily leads to the formation of cracks.

Radome is an enclosure material which protects an antenna or radar system from wind, rain, ice, UV, etc. It is a material of electrically transparent to electromagnetic energy through which power loss must be minimum in transmission. Therefore, low dielectric constant and loss are one of the desired properties together with high strength, high thermal shock resistance and high thermal stability. There are a lot of candidate materials for radomes such as Al_2O_3, pyroceram, $3Al_2O_3.2SiO_2$, BN, BeO, $2MgO.2Al_2O_3.5SiO_2$ and Si_3N_4. Mechanical, dielectric and thermal properties must be considered all together and optimized based on the radome requirements such as velocity, flight time, vibration, temperature fluctuation, etc.

In this thesis, it was aimed to investigate fabrication of mullite ceramics by gel casting method because this method has not been studied towards producing dense mullite ceramics in literature. Mullite was the choice of ceramic due to its excellent creep resistance and thermal shock resistance at high temperatures, and low dielectric properties suitable for electronic substrate and radome applications. Gel casting parameters such as monomer types (e.g., acrylamide-AM and metyhlenebisacrylamide-MBAM), AM/MBAM ratios (e.g., 6, 9, 12, 15, 20), effect of initiator (e.g., ammoniumpersulfate-APS) and catalyst (e.g., tetramethylenediamine-TEMED) were studied in detail. Densification behavior, dielectric properties (dielectric and tangent loss), mechanical properties (fracture

toughness, hardness, Young's modulus and flexural strength) and thermal properties (thermal expansion coefficient, thermal conductivity and thermal shock resistance) were characterized and carefully evaluated for a possible radome application.

Commercial mullite powder had a mean particle size of 3-5 μm and 5-10% glass phase. Ball milling was applied for 48 h and mean size was successfully decreased to 0.28 μm, which was very suitable for colloidal processing. 3.4 wt% nano TiO_2 (e.g., 21 nm) was added to form a liquid phase to aid densification. TiO_2 consisted of a mixture rutile 85 % anatase and 15 % rutile phases. 2 wt% ammonium salt of polyacrylic acid was used as anionic dispersant for colloidal stability of the particles. Monomer stock solutions (14 wt%) at various AM/MBAM ratios were prepared and used in gel casting. TEMED was added to accelerate curing process in some gel slurries. All gel casting slurries were prepared using a speedmixer rotated at 3500 rpm for 5 minutes.

TEMED with APS was used to lower as well as to control curing (gelation or polymerization) time. They formed oxygen free radicals which initiated the process and affected the gelation time. Curing was completed in 3 to 5 minutes at 25°C for the samples with TEMED and in 35 to 65 minutes at 70°C for the samples without TEMED. As soon as the curing was completed, gelled samples were quickly removed from the aluminum molds to allow uniform drying from all surfaces and not to induce any stress gradient.

Polymers used in gel casting were successfully removed from the green body at 600°C with a heating rate of 2°C/min, based on a TG-DTA analysis. All samples with and without TEMED reached to relative densities of 97 to 98.2 % after liquid phase sintering at 1540°C for 2 h, which indicated that AM/MBAM ratios and TEMED didn't significantly change densification. Also, the apparent porosity (or open porosity) was less than 0.62 %, and water absorption was 0 % for all samples. There happened about a weight loss of 0.89 wt% after sintering, which was attributed to the volatilization of K_2O and Na_2O present in the initial powder. XRD analysis showed mullite phase together with minor amounts of rutile TiO_2 and corundum. Corundum was present in the as-received powder. TiO_2 did not completely dissolve

in the mullite matrix although its solubility limit was between 2 and 6 wt%. Therefore, unreacted TiO_2 was attributed to the possible agglomeration of nano TiO_2 particles during ball milling due to insufficient dispersant amount.

Backscattered SEM images revealed distinct microstructural characteristics irrespective of the AM/MBAM ratios and TEMED; anisotropically grown mullite grains, glassy phase located as islands between the grains, hexagonally-shaped grains, white-color grains, and sharp-cornered pores. Mullite had tendency to grow anisotropically by means of dissolution of smaller grains and precipitation on larger grains during liquid phase sintering. Glassy phase was already present in the initial powder, as determined in XRD. EDS analysis revealed that hexagonally-shaped grains were Al_2O_3, which was also present in the initial powder, and white-color grains were ZrO_2 and TiO_2. ZrO_2 was possibly contaminated during milling of powder with ZrO_2 balls, and TiO_2 was the unreacted rutile phase as evident in the XRD analysis. Sharp-cornered and faceted pores were a common characteristic of the systems experiencing random anisotropic grain growth.

AM/MBAM ratios and TEMED didn't significantly change the hardness of the samples and average values ranged from 1077 HV to 1089 HV. Similarly, average fracture toughness values ranged from 2.4 to 2.5 MPa. $\sqrt{m}$ for all samples. These results were very close to the reported mullite values in literature. SEM picture revealed both intergranular and intragranular fractures. Grain shape and its angle to propagating crack was found to be very critical to determine crack deflection and bridging mechanisms. For example, crack was successfully deflected when the elongated grains were either parallel or located at a deviation angle to the propagating crack. However, perpendicular elongated grains were ineffective in bridging/deflecting the advancing cracks. In contrast to the trends for the densification, hardness and fracture toughness results, TEMED significantly affected the flexural strength of the samples such that the averaged values ranged from 172 MPa to 182 MPa for the samples with TEMED and from 130 MPa to 210 MPa for the samples without TEMED. The curing time was much shorter by using TEMED, which allowed fast demolding and uniform drying from all surfaces, and yielded uniform and distortion-free samples. Therefore, very close flexural strength values

were measured. The reliability of the ceramics were determined by Weibull modulus using flexural strength of the samples with TEMED. The Weibull modulus was found to be a high value of 12.33, stating lower spreading of fracture strength and more reliable materials. The characteristic strength was 186 MPa below which no failure was expected. Young's modulus decreased from 185 MPa at 96.2 % relative density to 161 GPa at 91.4 % relative density due to the effect of porosity.

The thermal conductivity was calculated from the thermal diffusivity, specific heat and density measurements. It increased with temperature and varied between nearly 1.5 W/m.K at 50°C and 3.75 W/m.K at 550°C, which was opposite to the trend of the crystalline ceramics where scattering of phonons decreases the thermal conductivity with increasing temperature. This result was in fact expected because mullite used in this study contained 5-10 % glassy phase that embraced the crystalline grains and dominated the total conductivity. Thermal expansion coefficient was determined by a linear fit drawn to the relative expansion vs. temperature data between 30°C and 800°C, and the slope gave 5.26 ppm/°C for the CTE. The CTE of mullite was 5.3 ppm/°C between 25°C and 1000°C. Thermal shock effect on fracture toughness and crack propagation was investigated by indentation-quench method. A pre-crack was formed with a Vicker hardness indenter and then the samples were quenched into water from different temperatures. Critical temperature difference of quenching was reported from a temperature where a 10 % crack extension was observed, which corresponded to nearly 400°C. In addition, a thermal shock resistance parameter (e.g., R in °C) was calculated using mechanical and thermal results. The calculated R values for candidate ceramics of Al_2O_3, BN, Si_3N_4, and BeO were 80°C, 325°C, 321°C, and 71°C, respectively. The R value for the dense mullite in this study was 142.4°C, which was higher than Al_2O_3 and BeO. Although Si_3N_4 and BN had much higher R values, higher sintering temperatures under controlled atmosphere were required for Si_3N_4 and hot-pressing for BN. In addition, BeO is a toxic material.

The dielectric constant was found as nearly 7.5 up to 10 GHz, which was in between reported values of 6.5 and 8.1 up to 14 GHz. The loss tangent was 0.0031 at 5 MHz. Lower dielectric constant was desired for wide frequency band application in radomes. Also, signal transmission delay time of mullite was reported 17 % less than

that of Al_2O_3 due to its lower dielectric constant. The dielectric constant change per 100°C must be minimum and it was reported for Al_2O_3, pyroceram, mullite, BN, BeO as 1.20 %, 0.5%, 0.4 %, 0.6 %, and 1.5 %, respectively, which showed that mullite was among the lowest one.

In short, mullite is a suitable candidate ceramic for radome applications because it has a higher R value than Al_2O_3 and has advantages in terms of sintering in air as opposed to Si_3N_4 and BN ceramics. They have low and temperature-stable dielectric properties. They can also withstand quenching from nearly 400°C. A large block at a dimension of 240x250x35 mm^3 was also successfully casted by preparing a slurry of nearly 6 kg which contained TEMED with an AM/MBAM ratio of 12. The green samples were easily machined to desired shapes by using a standard lathe machine.

FUTURE STUDIES

- Detailed investigation of the microstructures by SEM and EDS
- Temperature dependence of mechanical, thermal and dielectric properties
- Porosity and composition dependence of thermal and mechanical properties
- Detailed investigation of glass transition temperature
- Fabrication of large radomes and their environmental tests for industrial applications

REFERENCES

[1] Guo, X., *"Gel casting of high strength ceramics"*, Diploma work in Master programme, Chalmers University of Technology. 2011.

[2] Koçlar, G. S., "*Gelcasting of alumina ceramics with gelatin and carrageenan gum and investigation of their mechanical properties* ", MS thesis, İzmir Institute of Technology, 2013.

[3] Li, Y. & Yang, C. & Zhao, H. & Qu, S. & Li, X. & Li, Y., " *New developments of Ti-based alloys for biomedical applications. Materials"*, Materials, *7*(3), 1709-1800, 2014

[4] Ahsan, H. *&* Ali, A. & Ali, R., *"Oxygen free radicals and systemic autoimmunity. Clinical & Experimental Immunology"*, *131*(3), 398-404. 2003.

[5] Jain,R.,"*Gel Electrophoresis"*. Retrieved July 10, 2018, from https://www.slideshare.net/RishabhJain413/lectut-btn202pptl13-gel-electrophoresis. April 28, 2017.

[6] Electrophoresis Acrylamide Polymerization- A practical approach. (n.d), Retrieved July10, 2018, from http://www.bio-rad.com/webroot/web/pdf/lsr/literature/Bulletin_1156.pdf

[7] Hong, Y. & Mao, Z. & Wang, H. & Gao, C.& Shen, J., "*Covalently crosslinked chitosan hydrogel formed at neutral pH and body temperature*", *Journal of Biomedical Materials Research Part A*, *79*(4), 913-922, 2006

[8] SDS-PAGE.(n.d).RetrievedJuly10,2018,from http://capricorn.bc.edu/wp/pathways/protein-expression/sds-page/

[9] Sun, S. & Cao, H. & Su, H. & Tan, T., *"Preparation and characterization of a novel injectable in situ cross-linked hydrogel",*Polymer bulletin , 62(5), 699-711, 2009

[10] Young, A. C. &Omatete, O. O. & Janney, M. A. & Menchhofer, P. A., *"Gelcasting of alumina"*, Journal of the American Ceramic Society, 74(3), 612-618, 1991.

[11] Altun , A. A., " *Development of Photocurable ceramics suspensions for lithiography- Based ceramic manufacturing",* diploma thesis, Universitat Wien, 2016.

[12] Tari, G., " Gel casting ceramics: A review", Am. Ceram. Soc. Bull, 82 (4) 43-46, 2003.

[13] Monash, P. & Pugazhenthi, G. & Saravanan, P.*,"Various fabrication methods of porous ceramic supports for membrane applications",* Reviews in Chemical Engineering, 29(5), 357-383, 2013.

[14] Hagedorn, Y. C.,"*Additive manufacturing of high performance oxide ceramics via selective laser melting"* , LehrstuhlfürLasertechnik, 2013.

[15] Janney, M. A & Nunn, S. D. & Claudia, A. W. &Ogbemi O. *O.* & *Randy, B. O.*& *Glen, H. K.* &*April D. M., "Gel casting",* THE HANDBOOK OF CERAMIC ENGINEERING, 1998.

[16] Drying and Binder removal. (n.d). Retrieved July 10, 2018, from http://old.vscht.cz/sil/keramika/Ceramic_Technology/SM-Lect-3-A.pdf

[17] Liu, P. F. & Li, Z. &Xiao, P. & Liu, Y. & Liu, Z. Y. & Luo, H.& Huang, Y. Q. "*Effect of the molecular weight and concentration of PEG solution on microstructure and mechanical properties of Si_3N_4 ceramics fabricated by gel-casting"*, Ceramics International, 44(8), 8800-8808, 2018.

[18] Janney, M. & Walls, C. A. & Kupp, D. M. & Kirby, K. W. *"Gelcasting SiAlON radomes*", American Ceramic Society Bulletin, 83(7), 9201-9206, 2004.

[19] Radome information. (n.d). Retrieved July 9, 2018. From https://www.globalspec.com/learnmore/electrical_electronic_components/enclosures/radomes.

[20] Corning museum of glass-finished nose cone for a standard missile. (n.d). Retrieved July 9, 2018, fromhttps://www.cmog.org/artwork/finished-nose-cone-standard-missile

[21] Khatavkar, N. & Balasubramanian, K.*,"Composite materials for supersonic aircraft radomes with ameliorated radio frequency transmission-a review"*, RSC Advances, 6(8), 6709-6718, 2016.

[22] Volakis, J. L., Chapter 53- radome, Burks, D. G.*, "Antenna engineering handbook"*. (53-1, 53-18), (4th. Ed.). New York: McGraw-Hill, 2007.

[23] Cary, R. H., "*Avionic radome materials"*, Royal Radar establishment Malvern, UNITED KINGDOM, 1974.

[24] Radio Frequency. (n.d). Retrieved July 8, 2018, from https://searchnetworking.techtarget.com/definition/radio-frequency .

[25] Lal, B. &Khosa, S. K. & Tickoo, R. & Bamzai, K. K. & Kotru, P. N. *"Dielectric characteristics of melt grown doped KMgF3 crystals"*, Materials chemistry and physics, 83(1), 158-168, 2004.

[26] Badr, A. M. & Elshaikh, H. A. & Ashraf, I. M. *"Impacts of temperature and frequency on the dielectric properties for insight into the nature of the charge transports in the Tl2S layered single crystals"*, Journal of Modern Physics, 2(01), 12, 2011.

[27] Barsoum, M., *"Fundamentals of Ceramics".* McGraw-Hill. Michigan

university, New York, 1997.

[28] Microwave and Radio Waves. (n.d). Retrieved July 15, 2018, from http://wifiinschools.org.uk/15.html

[29] Atyia, H. E., *"Deposition Temperature Effect on the Electric and Dielectric Properties of $InSbSe_3$ Thin Films*," Vacuum, Vol. 81, pp. 590-598, 2007.

[30] Kingery, W. D., *"Introduction to Ceramics,"*J. Electrochem. Soc., vol. 124, no. 3, p. 152C. 1977.

[31] Schneider, H. & Okada, K. & Pask, J. A., & Rahman, S. H., *"Mullite and mullite ceramics"*. New York: J. Wiley. 1994.

[32] What is insertion loss and how it specified?. (n.d). Retrieved July 8, 2018, from https://www.amphenolrf.com/faq/technical/what-is-insertion-loss-and-how-is-it-specified.html

[33] What is the relationship between frequency and wavelength?, (n.d), Retrieved:July8,2018,from http://hubblesite.org/reference_desk/faq/answer.php.id=72&cat=light [online].

[34] Sebastian, M. T. & Jantunen, H., *"Low loss dielectric materials for LTCC applications: a review,",* pp. 57–90, Int. Mater. Rev., vol. 53, no. 2, 2008.

[35] Imanaka, Y., *"Multilayered low temperature cofired ceramics (LTCC) technology"*. Springer Science & Business Media, 2005.

[36] Ruh, R. & Chizever, H. M. *"Permittivity and Permeability of Mullite- SiC- Whisker and Spinel- SiC- Whisker Composites"*, Journal of the American Ceramic Society, 81(4), 1069-1070, 1998.

[37] Zou, C. & Zhang, C. & Li, B. & Wang, S. & Cao, F. *"Microstructure and properties of porous silicon nitride ceramics prepared by gel-casting and gas pressure sintering"*, Materials & Design, 44, 114-118, 2013.

[38] Narayan, R. & Colombo, P., *"Advances in Bioceramics and Porous Ceramics IV"*, 6th. Ed. John wiley & Sons. 2013.

[39] Othman, M. B. H. & Ramli, M. R. & Tyng, L. Y. & Ahmad, Z., & Akil, H. M.*"Dielectric constant and refractive index of poly (siloxane–imide) block copolymer",* Materials & Design, 32(6), 3173-3182, 2011.

[40] HASSELMAN, D.P.H. & SINGH, J.P. , *"Role of mixed-mode crack propagation in thermally shocked brittle materials, Theoretical and Applied Fracture Mechanics 2"* ,59-65, 1984.

[41] W. D. Callister, "*Materials science and engineering: An introduction*".7th ed. USA: John Wiley & Sons. 2007.

[42] D. J. Green, "*An Introduction to the Mechanical Properties of Ceramics"*.1st ed. Cambridge: Cambridge University Press, 1998.

[43] Belghalem, H. & Hamidouche, M. & Gremillard, L. & Bonnefont, G. & Fantozzi, G.,*"Thermal shock resistance of two micro-structured alumina obtained by natural sintering and SPS"*, Ceramics International, 40(1), 619-627, 2014.

[44] Cold research and engineering laboratory report -Table 1: Dielectric constant of water. (n.d). Retrieved June 7, 2018, from http://coldregionsresearch.tpub.com/SR98_02/SR98_020009.htm.

[45] AZO Materials-Sintered Silicon nitride. (n.d). Retrieved July 5, 2018, from https://www.azom.com/article.aspx?ArticleID=260 .

[46] National center for Biotechnology information,Pub chemical compound database. (n.d). Retrieved June 15, 2018, from https://pubchem.ncbi.nlm.nih.gov/compound/beryllium_oxide#section=Top

[47] Pickens, E. B. & Trice, R. W., *"Pressureless sintering of silicon nitride/boron nitride laminate composites",* Journal of materials science, 40(8), 2101-2103, 2005.

[48] Aksay, I. A. & Dabbs, D. M. & Sarikaya, M. *"Mullite for structural, electronic, and optical applications"*, Journal of the American Ceramic Society", 74(10), 2343-2358, 1991.

[49] Duval, D. J., Risbud, S. H., & Shackelford, J. F.."*Mullite. In Ceramic and glass materials* ". (pp. 27-39). Boston: Springer, MA, 2008.

[50] Chapter2: Mullite-review (pp:36), (n.d). Retrived July 7, 2018, from http://shodhganga.inflibnet.ac.in/bitstream/10603/77324/9/09_chapter%202.pdf

[51] Alumina and Alumina refractories. (n.d). Retrieved May 12, 2018, fromhttp://ispatguru.com/alumina-and-alumina-refractories/

[52] Bhowmick, T. *"A study on the development of refractories for carbon black Reactor*", PhD thesis. (pp:4),Department of Ceramic Engineering National Institute of Technology, Rourkela. 2013

[53] Fischer, R. X., & Schneider, "*Crystal structure of Cr-mullite. American Mineralogist"*, 85(9), 1175-1179, 2000.

[54] Anggono, J. *"Mullite ceramics: its properties structure and synthesis"*, Jurnal Teknik Mesin, 7(1), 1-10, 2005.

[55] Chapter2: Mullite-review, (n.d). Retrived July 7, 2018, from http://shodhganga.inflibnet.ac.in/bitstream/10603/77324/9/09_chapter%202.pdf

[56] AZO materials- Mullite. (n.d.). Retrieved April 25, 2018, from https://www.azom.com/properties.aspx?ArticleID=925 .

[57] Memsnet- material: Mullite, bulk. (n.d). Retrieved April 5, 2018, from https://www.memsnet.org/material/mullite3al2o32sio2bulk/.

[58] Accuratus-mullite ceramic properties. (n.d). Retrieved July 5, 2018, from https://www.accuratus.com/mullite.html .

[59] Ferro Ceramic INC. -mullite properties. (n.d). Retrieved July 4, 2018, from http://www.ferroceramic.com/mullite_table.htm

[60] Schneider, H. & Schreuer, J. & Hildmann, B. *"Structure and properties of mullite—a review"*, Journal of the European Ceramic Society, 28(2), 329-344, 2008.

[61] Yu, J. & Wang, H., & Zhang, J. "*Neural network modeling and analysis of gel casting preparation of porous Si3N4 ceramics"*, Ceramics International, 35(7), 2943-2950, 2009.

[62] Yang, A. & Wang, C. A. & Guo, R. & Huang, Y. & Nan, C. W. *"Porous PZT ceramics with high hydrostatic figure of merit and low acoustic impedance by TBA- based gel- casting process"*, Journal of the American Ceramic Society, 93(5), 1427-1431, 2010.

[63] Tulliani, J. M. & Bartuli, C. & Bemporad, E. & Naglieri, V. & Sebastiani, M. *"Preparation and mechanical characterization of dense and porous zirconia produced by gel casting with gelatin as a gelling agent"*, Ceramics International, 35(6), 2481-2491, 2009.

[64] Liu, Y. F. & Liu, X. Q. & Wei, H., & Meng, G. Y. *"Porous mullite ceramics from national clay produced by gel casting",* Ceramics International", 27(1), 1-7, 2001.

[65] Xu, X. & Dong, X. & Guo, A. & Wang, M. & Sui, G. & Liu, J. *"Effect of binder types on the properties of the mullite fibrous ceramics prepared by TBA-based gel-casting method"*, Ceramics International, 43(1), 228-233, 2017.

[66] SYMULOX- Synthetic sintered mullite. (n.d). Retrieved July 4, 2018, from https://nabaltec.de/fileadmin/user_upload/03_produkte/03-5_synthetischer-mullit/nabaltec_tds_symulox-m72.pdf.

[67] Aeroxide, TiO_2 P25. (Jan, 2018). Retrieved July 5, 2018, from https://products-re.evonik.com/www2/uploads/productfinder/AEROXIDE-TiO2-P-25-EN.pdf .

[68] Evonik Industries- (AEROXİDE, AERODISP AND AEROPERL) Titanium dioxide as photocatalyst Technical information 1243. (n.d). Retrieved July 3, 2018, from http://www.aerosil.com/sites/lists/RE/DocumentsSI/TI-1243-Titanium-Dioxide-as-Photocatalyst-EN.pdf

[69] Standard Test Methods for Apparent Porosity, Water Absorption, Apparent Specific Gravity, and Bulk Density of Burned Refractory Brick and Shapes by Boiling Water. (n.d). Retrieved July 10, 2018 from https://edisciplinas.usp.br/pluginfile.php/4254532/mod_resource/content/0/Norma%20determina%C3%A7%C3%A3o%20densidade%20a%20verde.pdf

[70] Lawn, B. R. & Evans, A. G. & Marshall, D. B. *"Elastic/plastic indentation damage in ceramics: the median/radial crack system",* Journal of the American Ceramic Society, 63(9- 10), 574-581, 1980.

[71] Kübler, J. & Gauckler, L. J.,*" Mechanical Properties of Ceramics. Materials Science II-2010",* Ceramic Materials, 6(3), 1-21, 2010.

[72] "Thermal conductivity and Thermal Diffusivity". (n.d.). Retrieved July 10, 2018, from http://www.tainstruments.com/wp-content/uploads/BROCH-ThermalConductivityDiffusivity-2014-EN.pdf , 2014.

[73] The dielectric constant. (n.d.). Retrieved June 25, 2018, from http://physics.bu.edu/~duffy/semester2/c08_dielectric_constant.html .

[74] Andersson, T & *Rowcliffe, D. J.,"Indentation Thermal shock test for ceramics",*J. Am. Ceram. Soc., 79 [6] 1509-14, 1996.

[75] Cascales, A. & Tabares, N. & Bartolomé, J. F. & Cerpa, A. & Smirnov, A. & Moreno, R. & Nieto, M. I. *"Processing and mechanical properties of mullite and mullite–alumina composites reinforced with carbon nanofibers",* Journal of the European Ceramic Society, 35(13), 3613-3621, 2015.

[76] Skocaj, M. & Filipic, M. & Petkovic, J. & Novak, S., *"Titanium dioxide in our everyday life; is it safe?"* Radiology and oncology, 45(4), 227-247, 2011.

[77] Ren, L. & Luo, X. & Xia, Y. & Hu, Y. & Zhou, H. *"Fabrication of a high-performance film based borosilicate glass/Al2O3 ceramics for LTCC application",* Journal of the European Ceramic Society, 37(6), 2415-2421, 2017.

[78] Zeta potential an introduction in 30 minute, Technical note. (n.d). Retrieved July5,2018,fromhttp://www.materials-talks.com/wp content/uploads/2017/09/mrk654-1_an_introduction_to_zeta_potential_v3.pdf .

[79] Vanderbilt Minerals, LLC Darvan (dispersing agent)-Technical Data. (n.d). RetrievedMay25, 2018, fromhttps://www.vanderbiltminerals.com/assets/uploads/documents/technical/TDS_DARVAN_Dispersing_Agents_Web.pdf

[80] Burgos-Montes O. & Moreno, R. *"Colloidal behaviour of mullite powders produced by combustion synthesis",* Journal of the European Ceramic Society, 27(16), 4751-4757, 2007.

[81] Janney, M. A & Nunn, S. D. & Claudia, A. W. &Ogbemi O. *O.* & *Randy, B. O.*& *Glen, H. K.* &*April D. M., "Gel casting". (pp:5).* THE HANDBOOK OF CERAMIC ENGINEERING, 1998.

[82] Huang, Y. & Yang, J. "*Novel colloidal forming of ceramics*", Springer Science & Business Media, 2011.

[83] Mandal, S. & Sahu, M. K. & Patel, R. K. ,"*Adsorption studies of arsenic (III) removal from water by zirconium polyacrylamide hybrid material (ZrPACM-43)*", Water resources and industry, 4, 51-67, 2013.

[84] Gönenli, I. E. & Messing, G. L. *"Texturing of mullite by templated grain growth with aluminum borate whiskers"*, Journal of the European Ceramic Society, 21(14), 2495-2501, 2001.

[85] J. Matousek, "Chemistry of Evaporation from Silicate Melts," p. 10.

[86] Hong, S. H. & Lee, N. & Carim, A. H. & Messing, G. L. *"Interfacial precipitation in titania-doped diphasic mullite gels*", Journal of materials research, 13(4), 974-978, 1998.

[87] Baudin, C. & MOYA, J. S. *"Influence of titanium dioxide on the sintering and microstructural evolution of mullite",* Journal of the American Ceramic Society, 67(7), C-134, 1984.

[88] Duran, C. & Tür, Y. K. *"Phase formation and texture development in mullite/zirconia composites fabricated by templated grain growth"*, Journal of materials science, 41(11), 3303-3313, 2006.

[89] H. Schneider, in Ceramic Transactions, Vol. 6, "Mullite and Mullite Matrix Composites", S. Somiya (Ed.) & R. F. Davis (Ed.) & J. A. Pask (Ed.). (pp:135-158). Westerville,OH, : The American Ceramic Society. 1990.

[90] Galizia, P., Maizza, G.& Galassi, C., "*Heating rate dependence of anatase to rutile transformation"*, Process. Appl. Ceram, 10(4), 235-241, 2016.

[91] Huang, T. & Rahaman, M. N. & Mah, T. I. & Parthasarathay, T. A., *"Anisotropic grain growth and microstructural evolution of dense mullite above 1550 C"*,Journal of the American Ceramic Society, 83(1), 204-10., pp:204, 2000.

[92] Hong S. H. "Transformation kinetics, AGG, textured microstructures in diphasic mullite". PhD Thesis , Penn State university, 1997.

[93] Seabough, M. , PHD THESIS p 29, Penn state university, 1998.

[94] Hamidouche, M. & Bouaouadja, N. & Olagnon, C. & Fantozzi, G. *"Thermal shock behaviour of mullite ceramic",* Ceramics International, 29(6), 599-609, 2003.

[95] Paek, Y. K. & Suvaci, E. & Messing, G. L. *"Preparation and fracture behavior of alumina platelet reinforced alumina-monazite composites"*, Materials Transactions, 43(12), 3262-3265, 2002.

[96] Souza, R. C. & dos Santos, C. & Barboza, M. J. R. & de Araujo Bicalho, L. & Baptista, C. A. R. P. & Elias, C. N., *"Fatigue behavior of 3% Y2O3-doped ZrO2 ceramics"*, Journal of Materials Research and Technology, 3(1), 48-54, 2014.

[97] Fu, Y. &Tao, Z. & Hou, X. "*Weibull distribution of the fracture strength of 99% alumina ceramic reshaped by cold isostatic pressing"*, Ceramics International, 40(6), 7661-7667, 2014.

[98] Nielsen, L. F., *"Strength and stiffness of porous materials",* Journal of the American Ceramic Society, 73(9), 2684-2689, 1990.

[99] Anderman Industrial Ceramics Data sheet:mullite. (n.d). Retrieved July 4, 2018, from http://www.earthwaterfire.com/pdf_library/material_mullite.pdf .

[100] Callister ,W. D., "*Materials science and engineering: An introduction*".7th ed. (pp:666-667) USA: John Wiley & Sons. 2007.

[101] Poirier , D.R. &Geiger G.H., *"Transport Phenomena in Material Processing"* (pp:202), Switzerland: Springer International Publishers, The minerals, metals and materials society. 2016.

[102] Lide , D. R., "*CRC Handbook of Chemistry and Physics,"*eBook, p. 3485, 2003

[103] Schneider, H. & Eberhard, E. "*Thermal expansion of mullite",* Journal of the American Ceramic Society", 73(7), 2073-2076, 1990.

[104] Krohn, D.A. & Hasselman, D.P.H. , "*Effect of abrasion on strength and thermal stress resistance of a glass*". J. Amer. Ceram. Soc., 56(6) 337-38, 1973.

[105] D.P.H. Hasselman, "*Strength behavior of polycrystalline alumina subjected to thermal shock*", J. Amer. Ceram. Soc., 53 (9) 490-95, 1970.

[106] Hasselman, D. P. H. & Shaffer, P. T. B *"Factors Affecting Thermal Shock Resistance of Polyphase Ceramic Bodies,"* WRIGHT AIR DEVELOPMENT DIVISION TECHNICAL REPORT (WADD-TR-60-749), Part II, 1962, from http://www.dtic.mil/dtic/tr/fulltext/u2/a281579.pdf

[107] Cui, K. & Li, Y., *"Fabrication, mechanical properties and thermal shock resistance of laminated TiB2–based ceramic"*, Int. Journal of Refractory Metals and Hard Materials 54 148–153, 2016.

[108] Dursun G. M., *"Alumina/glass composites for low temperature co-fired ceramics (LTCC) and radome applications"*, MS thesis, Ankara Yıldırım Beyazıt University, 2018.

[109] Mullite. (n.d). Retrieved June 25, 2018, from https://www.azom.com/properties.aspx?ArticleID=925

CIRCULUM VITAE

PERSONAL INFORMATION

Name Surname : Nazım ECEBAŞ

Date of Birth : 23/10/1993

E-mail : nazimm.ecebas@gmail.com

EDUCATION

2016 -2018 **Ankara Yıldırım Beyazıt University**, Ankara, Turkey

M.Sc., Materials Engineering

Thesis: "Gel Casting Of Mullite For Radome Application"

2011-2016 **Ankara Yıldırım Beyazıt University**, Ankara, Turkey

B.Sc., Materials Engineering, June 2016

Graduation Project: "The production of $Pb(Mg_{1/3}Nb_{2/3})O_3$-$Pb(Yb_{1/2}Nb_{1/2})O_3$- $PbTiO_3$"

INTERNSHIPS

June–August 2015 **TÜBİTAK - Defense Industries Research and Development Institute**

June-July 2014 **TAI – Turkish Aerospace Industries, Inc.**

TOPICS OF INTEREST

- Ceramic materials
- Radome materials
- Tape casting, gel casting
- Dry pressing
- Mechanical, dielectric and thermal properties of ceramics